ABSTRACT

TUNING STRUCTURAL AND PHYSICAL PROPERTIES VIA A-SITE DOPING IN PEROVSKITE-TYPE TRANSITION METAL OXIDES

Hamoud H. Somaily, Ph.D.
Department of Physics
Northern Illinois University, 2018
Omar Chmaissem, Director

This thesis investigates the structure-property relationship of two important classes of transition metal oxides (the perovskite-type A-site substituted titanates $(Sr_{1-x-y}Ca_xNd_y)TiO_3$ and manganites $(Sr_{1-x}Ba_x)MnO_3$). A thorough evaluation is provided of their potential for prospective technological applications in heat recycling and information technology by examining the thermoelectric and multiferroic properties, respectively. In the titanate compounds, we doped on the *A*-site with small rare earth ions in order to generate mixed valent transition metals to increase band filling while the Ca doping maintained fixed levels of distortions. In the case of the manganites, *A*-site Sr ions were substituted with large Ba ions for the purpose of increasing the materials strain and to promote ferroelectricity.

Crystal structure was investigated using high-resolution neutron powder diffraction as a function of temperature and Nd/Ba doping. In the titanates, two series were synthesized and designed to have a nominally constant tolerance factor at room temperature. We determine the room temperature structures as tetragonal $I4/mcm$ and orthorhombic $Pbnm$ for the Sr-rich and Ca-rich series, respectively. Three low

temperature orthorhombic structures, *Pbnm*, *Ibmm* and *Pbcm* were also observed for the Sr-rich series; whereas, the symmetry of the Ca-rich series remained unchanged throughout the full measured temperature range.

Thermoelectricity in ternary $(Sr_{1-x-y}Ca_xNd_y)TiO_3$ perovskites was investigated. The double substitution at the *A*-site maintained a fixed crystal distortion while Nd^{3+} doping modified the electronic properties of the materials via increased band filling. Unique compositions of cations allowed for increased *A*-site atomic mass disorder and the lattice thermal conductivity was significantly suppressed to values as low as ~ 1.5 W/K.m in some samples, approaching amorphous Silicon limit. Charge doping via balanced formation of Ti^{3+} at the *B*-site has transformed materials into n-type semiconductors. I examined the range of applicability of various conduction models, viz., variable range hopping, semiconductor- type conductivity across band gap, and small polaron hopping for the best description of the temperature variation of measured resistivity. We succeeded in achieving a relatively high figure of merit ZT=0.07 at $\sim$ 400 K in the Sr-rich $Sr_{0.76}Ca_{0.16}Nd_{0.08}TiO_3$ composition which is comparable to that of the best n-type *TE* $SrTi_{0.80}Nb_{0.20}O_3$ oxide material reported to date. With an enhanced Seebeck coefficient at elevated temperatures and reduced thermal conductivity, we predict that $Sr_{0.76}Ca_{0.16}Nd_{0.08}TiO_3$ and similar compositions have the potential to become some of the best materials in their class of thermoelectric oxides.

We also report the structure-property phase diagram of unique single-ion type-1 multiferroic pseudocubic $Sr_{1-x}Ba_xMnO_3$ perovskites. Employing a specially designed multi-step reduction-oxidation synthesis technique, we have synthesized previously unknown $Sr_{1-x}Ba_xMnO_3$ compositions in their polycrystalline form with a significantly extended Ba solubility limit that is only rivaled by a very limited number of crystals and thin films grown under non-equilibrium conditions. Understanding the multiferroic interplay with structure in $Sr_{1-x}Ba_xMnO_3$ is of great importance as it opens the door wide to the development of newer materials from the parent (AA')(BB')O_3 sys-

tem with enhanced properties. To this end, using a combination of time-of-flight neutron and synchrotron x-ray scattering techniques, we determined the exact structures and quantified the Mn and oxygen polar distortions above and below the ferroelectric Curie temperature T_C and the Néel temperature T_N. In its ferroelectric state, the system crystalizes in the noncentrosymmetric tetragonal $P4mm$ space group which gives rise to a large electric dipole moment P_S, in the z-direction, of 18.4 and 29.5 $\mu C/cm^2$ for x = 0.43 and 0.45, respectively. The two independently driven ferroelectric and magnetic order parameters are single-handedly accommodated by the Mn sublattice leading to a novel strain-assisted multiferroic behavior in agreement with many theoretical predictions. Our neutron diffraction results demonstrate the large and tunable suppression of the ferroelectric order at the onset of AFM ordering and confirm the coexistence and strong coupling of the two ferroic orders below T_N. The refined magnetic moments confirm the strong covalent bonding between Mn and the oxygen anions which is necessary for stabilizing the ferroelectric phase.

NORTHERN ILLINOIS UNIVERSITY
DE KALB, ILLINOIS

MAY 2018

TUNING STRUCTURAL AND PHYSICAL PROPERTIES VIA A-SITE DOPING IN PEROVSKITE-TYPE TRANSITION METAL OXIDES

BY

HAMOUD H. SOMAILY

A DISSERTATION SUBMITTED TO THE GRADUATE SCHOOL
IN PARTIAL FULFILLMENT OF THE REQUIREMENTS
FOR THE DEGREE
DOCTOR OF PHILOSOPHY

DEPARTMENT OF PHYSICS

Dissertation Director:
Omar Chmaissem

ACKNOWLEDGEMENTS

I am tremendously grateful to my advisor, Professor. Omar Chmaissem for his helpful guidance throughout the long and arduous journey of graduate school. His rarely-rivaled experience in the field of crystallography and the use of neutron diffraction in materials science was my conduit towards exploring this fascinating world. I also would like to extend my thanks to Professor. Bogdan Dabrowski for his valuable help and insightful knowledge, and to Dr. Stanislaw Kolesnik for the fruitful discussions of various subjects of interest related to the project.

DEDICATION

To my family.

TABLE OF CONTENTS

LIST OF TABLES

Table Page

LIST OF FIGURES

Figure Page

Figure Page

Figure Page

CHAPTER 1

INTRODUCTION

1.1 Perovskites: A Special Class of Simple But Diverse Transition Metal Oxides

Transition-metal oxides are among the most studied materials that received, over the last few decades after discovery of colossal magnetoresistive and high-T superconductivity, constant attention devoted to the investigation of their structural and physical properties. Perovskite, named in honor of the Russian mineralogist L.A. Perovski, is the mineral $CaTiO_3$ [1] and the term has been conventionally in use since then to refer to a family of oxide materials that take the general chemical formula ABO_3 [2]. Beside the importance of these materials in understanding and developing the fundamental concepts of solid state physics, perovskites are proven structurally flexible with novel and diverse phenomena that can be tailored to specific application area in addition to their sheer abundance as for instance the case with $MgSiO_3$ compound which is one of the two main constituents of the earth's lower mantle [3, 4].

Perovskite ABO_3 structure can be visualized as an infinite 3D network of ReO_3 - like transition metal octahedra having an (A-site) center cavity which effectively couples with alkaline or rare earth elements as shown in Fig. 1.1(a). These BO_6 octahedra are linked in each crystallographic direction via a bridging anion (usu-

ally an oxygen) whose atomic orbital overlapping with the transition metal plays a central role in determining the electronic and magnetic properties of the material.

The simple perovskite structure can exist in many variants such as the double perovskite (compared side by side with ABO_3 in Fig.1.1) to minimize lattice energy when the difference in charge or size of ions is large [1]. The double perovskite (A_2BBO_6) is a clear demonstration of the structural flexibility of perovskites to tolerate the presence of substantial doping on multiple cationic sites [5] with B and B' representing two different transition metals (e.g. Ba_2MgWO_6) whose size difference does not admit mixing/disorder on a single lattice site.

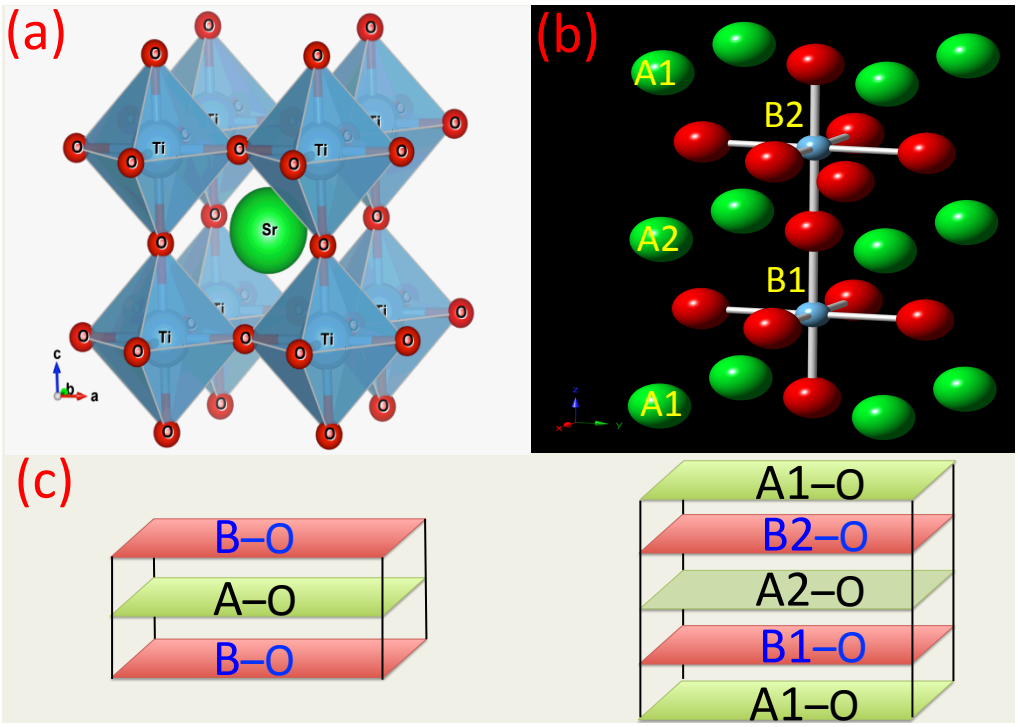

Figure 1.1: (a) The ideal (cubic) perovskite crystal structure of the archetypal $SrTiO_3$ (ABO_3) with B transition metal atoms centered at the corners of the unit cell forming a cubic close packed structure. (b) A complex variant of ABO_3 structure found in double perovskite materials compared side by side. (c) The unit cell is shown as infinite layers of ordered cation-anion sublattices along c axis in both structures.

The relation between Alkaline or rare earth doping and the physical properties is probably the most studied aspect of transition metal oxides with the perovskite structure. The layered materials have been considered for thermoelectric application due to the enhanced degeneracy of empty t_{2g} bands of the B ion and the large conductivity of e_g bands of the B' ion [6]. The alkaline earth doping of Ba or Sr stabilizes the tetragonal $I4/mmm$ phase and enhances superconductivity with high T_C in layered cuprate perovskites such as La_2CuO_4 [7]. In addition to that, Nd-doped titanate-based layered perovskites ($c/a \sim 6$) were developed which have large z-direction values of the spontaneous polarization P_S (100 $\mu C/cm^2$) for applications to nonvolatile ferroelectric random access memories [8]. These layered perovskites and other complex oxide superstructures such as the Ruddlesden-Popper (RP) perovskites ($A_{n+1}B_nO_{3n+1}$: n=1 for double layered perovskite) all lie outside the primary scope of this thesis and instead our main focus will be on the ABO_3 family whose simple crystal structure promises a much richer playground for investigating the structure-property relationship and provides more flexibility to optimize the physical properties.

The changes in the perovskite crystal structural often occur in response to changing ambient conditions such as temperature. Changing pressure also has similar effects on structure as decreasing temperature for displacive transitions [9]. Pressure has long been considered [10] an effective dual-role modulator of physical properties of perovskites. The delicate balance between long range attractive ionic interactions and short range on-site coulomb repulsion which stabilizes ferroelectricity in conventional materials is compromised with increasing pressure and T_C reduces but could as well be enhanced in some materials above a certain threshold hydrostatic pressure value [11]. Closely similar to the pressure effect is the strain engineering in multiferroic thin films. It has been reported that while epitaxial strain on the

multiferroic $BiFeO_3$ films has minimal effect on T_N, the FE Curie temperature T_C decreases dramatically in contrast with the behavior of typical ferroelectrics due to strong interplay of polar and non-polar oxygen tilting instabilities [12]. Large spin-lattice coupling via epitaxial-strain in $SrCoO_3$ for instance is capable of driving ferromagnetic-metallic to AFM-insulating ferroelectric transitions [13].

Atomic substitutions (sometimes referred to as chemical pressure) induce ionic size variance and lattice strains. A non-polar (antiferrodistortive) distortion is the most widely observed type of structural transition in cubic perovskites manifested by the cooperative tilting/rotation of the nearly rigid octahedra resulting from the displacements of oxygen atoms off their special positions while the transition metal remains in the center of the octahedra. This electrostatically driven oxygen displacement is a lattice response to changing the ionic sizes/temperature in order to maximize close packing of the structure as will be investigated in $Sr_{1-x-y}Ca_xNd_yTiO_3$ materials presented in chapter 4. Displacive phase transitions from ideal structure also correspond to changes in phonon modes of the Brillouin zone of the cubic phase [14].

Among the many forms of distortion from the ideal crystal structure is the B cation displacement off the center of the octahedra which is a ferrodistortive phenomenon that leads to misalignment of the center of mass of surrounding anions with the B cation and hence the development of ferroelectricity which we will encounter in $Sr_{1-x}Ba_xMnO_3$ materials in chapter 5. Displacive-type distortions are driven by lattice dynamical instabilities and often accompanied by the tendency of the frequency of a particular lattice vibrational mode (soft modes) toward zero at the phase transition boundary [15].

Distortions in perovskites need not be exclusively displacive in nature and may have an underlying electronic origin driven by the presence of strong electron-lattice

correlations in transition-metal oxides. For instance, the presence of 3d transition metal ion with electrons occupying the d orbitals according to Hund's rules could lead to cooperative the Jahn-Teller (J-T) effect. The strong electron-lattice coupling is manifested by significantly deformed octahedral bonds in same directions as electrons preferred orbital. This effect could also lead to orbital ordering [16] and lift the degeneracy of 3d orbitals as found for the intermediate spin state of $LaCoO_3$ perovskite [17]. It is not uncommon to observe more than one type of distortion present at the same time, for example the octahedral titling couples with the presence of an active J-T ion as found in the perovskite system $LaMnO_3$ [18]. Another example is the distortion in $PbZrO_3$ perovskite which is a consequence of polar instability emanating from Pb lone pairs that coexists with ZrO_6 octahedral rotations [19]. It has been recently shown [20] that two independent (non-polar) octahedral rotations in $Ca_3Mn_2O_7$ layered perovskite effectively break the spatial inversion symmetry and produce displacive ferroelectric order that couples to magnetic properties below T_N =115 K with first-principles calculated spontaneous polarization value of 5 $\mu C/cm^2$. Octahedral titling phase transitions in perovskites might show order-disorder characteristics as found in $SrSnO_3$ [21]. In addition, the nonstoichiometry-driven oxygen occupations of certain crystallographic sites can increase the degrees of structural complexity. This includes for instance reduced materials such as $SrMnO_x$ ($x < 2.7$) [22], ordered cobaltite superstructure $(Ln/La)BaCo_2O_{5+\delta}$ ($0 < \delta < 1$) [23] and $SrFeO_{2.875}$ [1].

The first step towards understanding and tuning of the extraordinary rich properties of perovskite materials is to apply a consistent and reliable tool for characterizing their crystal structures. Neutron diffraction is the primary experimental technique that is used throughout this thesis for that purpose whereas the non-polar distortions in $Sr_{1-x-y}Ca_xNd_yTiO_3$ perovskites is systematically described by

the Goldschmidt tolerance factor given as the ratio of distances between oxygen ions and cations as

$$t = \frac{(r_A + r_O)}{\sqrt{2}(r_B + r_O)} \tag{1.1}$$

Where r_A, r_B, and r_O are ionic radii of A, B and O ions, respectively, usually obtained from Shannon tables for different oxidation states and coordination environments [24]. A value of $t = 1$ corresponds to distortion-free materials but in rare cases such as in the paraelectric phase of cubic $BaTiO_3$, the nominal tolerance factor is greater than 1 (~ 1.07) due to the large ionic size of Ba^{2+} cation. The perovskite structure occurs usually within the range $0.75 \leq t \leq 1.00$ [23,25]. I should point out here that while structural changes that follow tolerance factor rules are ubiquitous in perovskites, there exist some peculiar anomalies that the t-factor can not predict as observed with the lattice parameters evolution in orthorhombic manganites for example [26].

While extremely useful, Shannon's tabulated values are x-ray averages based on the assumptions of complete ionic bonding and cannot always predict A-site ions as they often assume different values depending on the electronegativity of the B ions. Therefore, a more accurate calculation of t (we can refer to as the observed t factor) often requires using the actual measured bond lengths, A–O and B–O . Because of typically tiny displacements of the oxygen atoms, accurate measurements are only accessible via highly sensitive and non-destructive methods such as neutron diffraction. The NPD-measured bond lengths will allow me to calculate structural and physical parameters such as tolerance factor and spontaneous electric polarization for titanium and manganese based systems, respectively.

Nominal room temperature tolerance factor values for the full ternary $Sr_{1-x-y}Ca_xNd_yTiO_3$ system as shown in Fig. 1.2 are calculated using Eq. 1.2 which

is an extended expression based on Eq. 1.1 for complex compositions, along with the 10 samples which will be the subject of study in chapter 4 designed to have nearly the same t values and fixed distortion.

$$t = \frac{(1-x-y)\, r_A + x\, r_{A'} + y\, r_R + r_O}{\sqrt{2}[(1-y)\, r_B + y\, r_{B'} + r_O]} \tag{1.2}$$

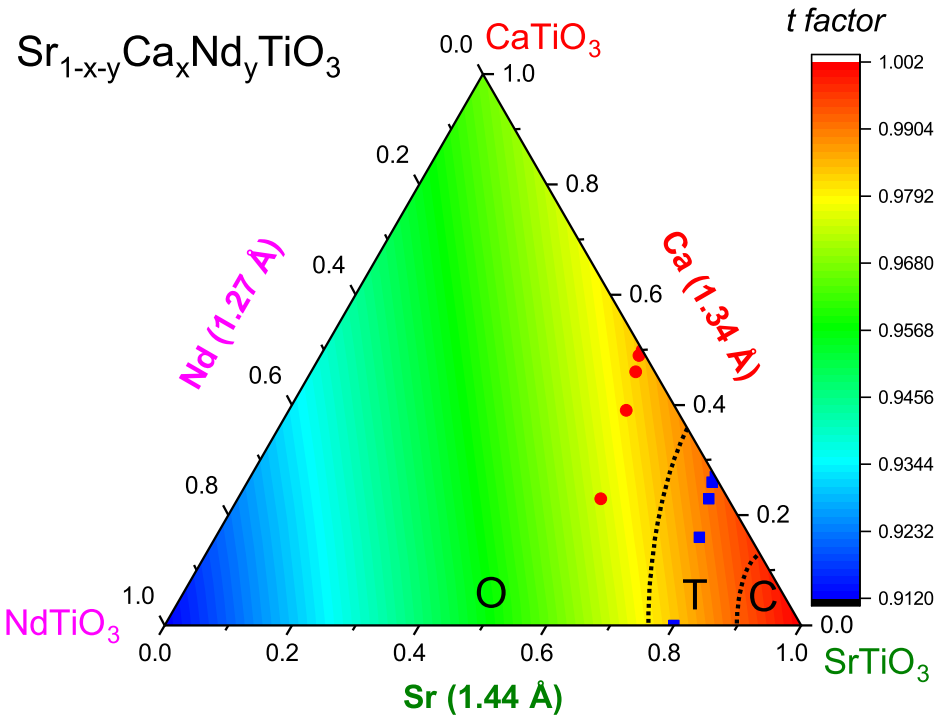

Figure 1.2: Isothermal t factor of ternary $Sr_{1-x-y}Ca_xNd_yTiO_3$ materials calculated at room temperature using Eq. 1.2 with the ionic radii from Shannon. Also shown is an overlay of the 10 samples that will be studied in chapter 4. Dashed curved boundary lines separate the three regions with different crustal structures (C = cubic, T = tetragonal, and O = orthorhombic).

While tolerance factor as shown in Fig.1.2 is a changing function of ionic radii, it also responds to temperature variations more progressively as found in the $CaTiO_3$ perovskite whose crystal structure is orthorhombic ($Pbnm$) at 300 K but transforms to the higher tetragonal symmetry ($I4/mcm$) at 1512 ± 13 K and then to the ideal

cubic ($Pm\bar{3}m$) at 1635 ± 2 K. Fig. 1.3 shows the tolerance factor as a function of temperature t(T) for $CaTiO_3$ using neutron powder diffraction results extracted from Ref. [27]. We expect similar effect of lowering temperature on the geometric tolerance factor of $Sr_{1-x-y}Ca_xNd_yTiO_3$ system.

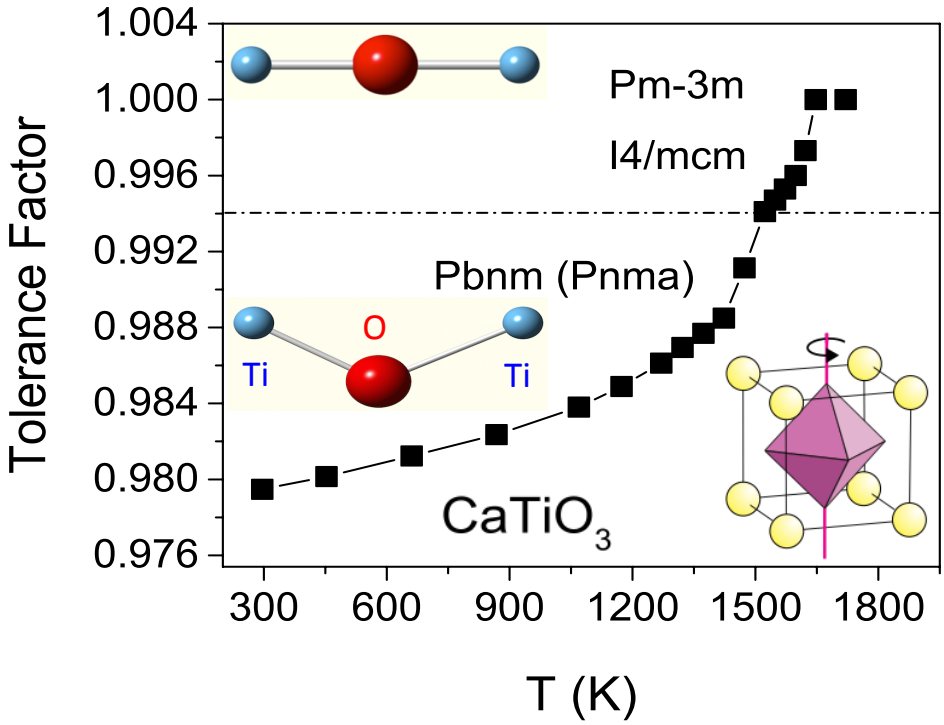

Figure 1.3: Tolerance factor as a function of temperature for $CaTiO_3$ shows its progressive increase (nearly perfect parabolic function of temperature). The transport properties which depend on the bandwidth or the Ti–O–Ti bond angle are expected to vary strongly with temperature as well. Observed transitions are due to tilting of nearly rigid linked octahedra about one of the unit cell three axes [1].

1.2 Electronic Properties of Perovskites

Good understanding of the electronic structure of transition metals in the octahedral complex is essential to describing the correlations between structural and

physical properties. In the BO_6 octahedra, the electrostatic potential (cubic crystal field) of oxygens stabilizes the splitting of the five initially-degenerate eigen-functions of the electron in 3d-orbitals of transition metal (e.g. Ti^{4+} or Mn^{4+}) into two distinct sets; the t_{2g} consisting of 3 degenerate (d_{xy}, d_{yz}, d_{xz}) orbitals and the higher energy e_g with 2 degenerate ($d_{x^2-y^2}$, d_{z^2}) orbitals.

The occupation of these subsets is dependent upon the electronic configuration of the cations. In the case of Ti^{4+} or Mn^{4+}, the e_g orbitals extending towards the oxygen ions are empty and thus all materials studied here are considered immune to Jahn-Teller distortions as opposed to the lower oxidation counterparts Mn^{3+} in its high-spin configuration where the lattice is strongly coupled with the electronic occupation of e_g orbitals and lead to elongation/compression of the bonds as shown in Fig. 1.4 [28]. The degeneracy of the lower t_{2g} subset can also be lifted and orbital ordering is established as found in $LaTiO_3$ based on the deviation of the semiconducting resistivity data from both the thermal activation and variable range hopping models [29]. Although the large electronegativity difference between cations and oxygen atoms in most perovskites indicates that the bonding is largely ionic, the diverse properties of these materials are attributed to the strong polarizable transition metal – oxygen bond with an appreciable covalent character.

A considerable degree of orbital overlapping is desirable for enhancing the material's properties such as electrical conductivity and for stabilizing ionic displacements as discussed in chapter 5 for multiferroic perovskites. According to band theory [31] (augmented plane wave band calculations [32]), A-site core electronic states are of little interest and the hybridization or π interaction mixes the t_{2g} orbitals of the transition-metal ion with the p orbitals of the oxygen such that the lowest conduction band determined principally by the (pd) interaction are made up of the transition metal d states which are separated from the filled oxygen p states in the

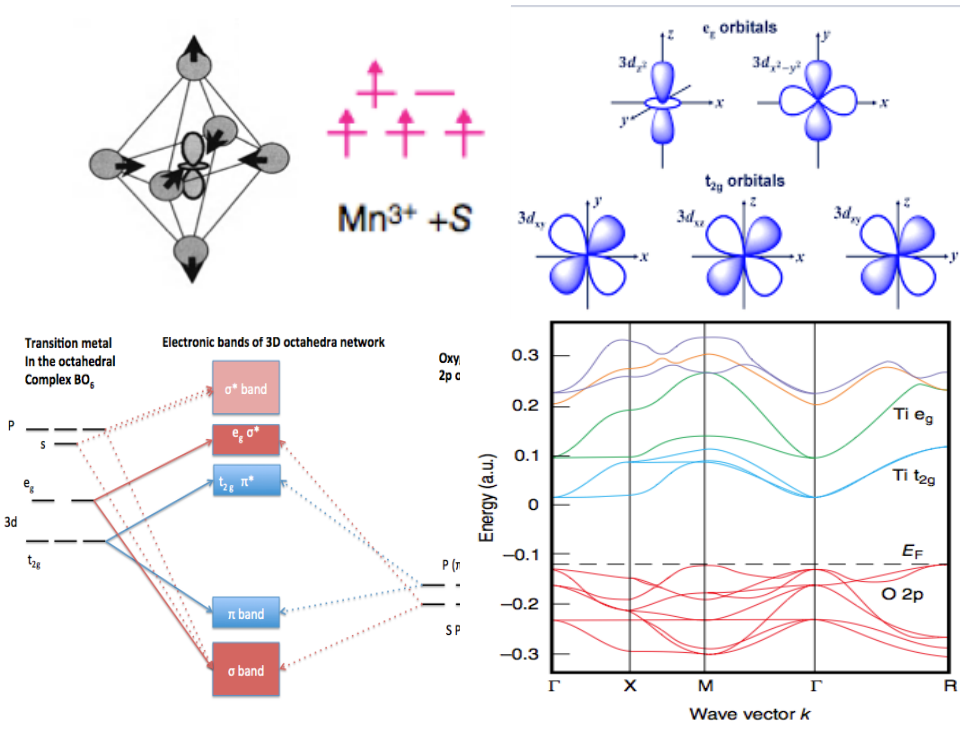

Figure 1.4: Top: Manganese Mn atom in its active (high-spin Mn^{3+}) J-T form which deforms the octahedra [25]. Mn^{4+} atoms in $Sr_{1-x}Ba_xMnO_3$ materials in chapter 5 are of the non-active J-T type. Bottom: Band structure of cubic $SrTiO_3$ showing energies relative to the Fermi level and a wide-gap band insulating characteristics [1, 30].

valence band by a wide energy gap (E_g) typically of the order of $1 - 4$ eV [2], see Fig. 1.4. Most perovskite oxides with d orbital electrons are Mott insulators with an energy gap that can be modulated by changing the B–O distance and B–O–B angle as demonstrated recently in Ba-doped cubic $SrMnO_3$ in which theoretical studies have shown that the energy gap between t_{2g} and e_g bands decreases with increased volume and ferroelectricity (FE) can be stabilized [33].

$SrTiO_3$ is a key ABO_3 perovskite material that is classified as a wide gap perfect insulator ~ 3.1 eV [1, 2]. Its transport properties can be drastically modified when electrons are added to the lattice. The one-electron t_{2g} bandwidth (W) created

in Rare-earth doped $Sr_{1-x-y}Ca_xNd_yTiO_3$ system (the oxidation state of Ti^{4+} t^0e^0 is altered with Nd doping to Ti^{3+} t^1e^0) is governed by the degree of interactions (overlap) between 3d -2p orbitals which in turn is extremely sensitive to perovskite distortions. We expect the Nd doping (band filling) at the A-site to have similar effect to that found in the semiconductor La^{3+}-doped $SrTiO_3$ [34,35]. One-electron bandwidth can instead be controlled by the magnitude of $< Ti–O–Ti >$ angle without changing the electronic density as found in $Ca_{1-x}Sr_xVO_3$ system where $3d^1$ t_{2g} band width should have similar characteristics to that of $Sr_{1-x-y}Ca_xNd_yTiO_3$ materials [36]. In manganites with the general formula $R_{1-x}A_xMnO_3$ (R=trivalent, A = divalent cations), the increase of the one-electron e_g bandwidth via doping with large Sr for Ca in the charge ordered $La_{0.5}Ca_{0.5}MnO_3$ perovskites is shown to control the magnetic transitions and T_C increases with the Sr content monotonically consistent with the enhancement in the double-exchange ferromagnetic interaction [37]. Alternatively, the oxidation state of the Ti metal can equally be changed via *B*-site substitutions with pentavalent cations such as Nb^{5+} [38] while oxygen-deficient $SrTiO_{3-\delta}$ materials transform into an n-type semiconductor [2,39] and even exhibits low-T superconductivity [40,41].

A-site or *B*-site vacancies due to the charge compensation process in La-doped ferroelectric $PbTiO_3$ perovskite can result in a giant dielectric constant characteristic of relaxor ferroelectric material in the case of B-site defects [42]. Intrinsic point defects is present in a material when the entropy gain from disorder is more favorable and surpasses the enthalpy increase as encapsulated in the Gibbs free energy of the system [43]. Because of its dependence on temperature, oxygen non-stoichiometry (vacancy/excess) which can be created during synthesis in a reducing/oxidizing environment is a common form of defects in perovskite-type oxides and could heavily impact and alter their thermoelectric and transport properties [44] since vacancies

act as electron donors in the conduction band and also create in-gap deep localized states [45]. For instance resistivity data of the oxygen deficient $SrTiO_{3-\delta}$ indicates a semiconductor-type behavior with enhanced conductivity as vacancies presence increases as shown in Fig. 1.5 [39]. The conduction is believed to occur by electron transfer or hopping from one ion to another via the bridging oxygen ion. Conduction in La-doped $CaMnO_3$ perovskites (x = 0 is an AFM insulator [46]) which is typical of nonmetallic materials above T $\sim$ 150 K is explained based on the thermal activation of charge carriers from impurity states associated with La dopants [47].

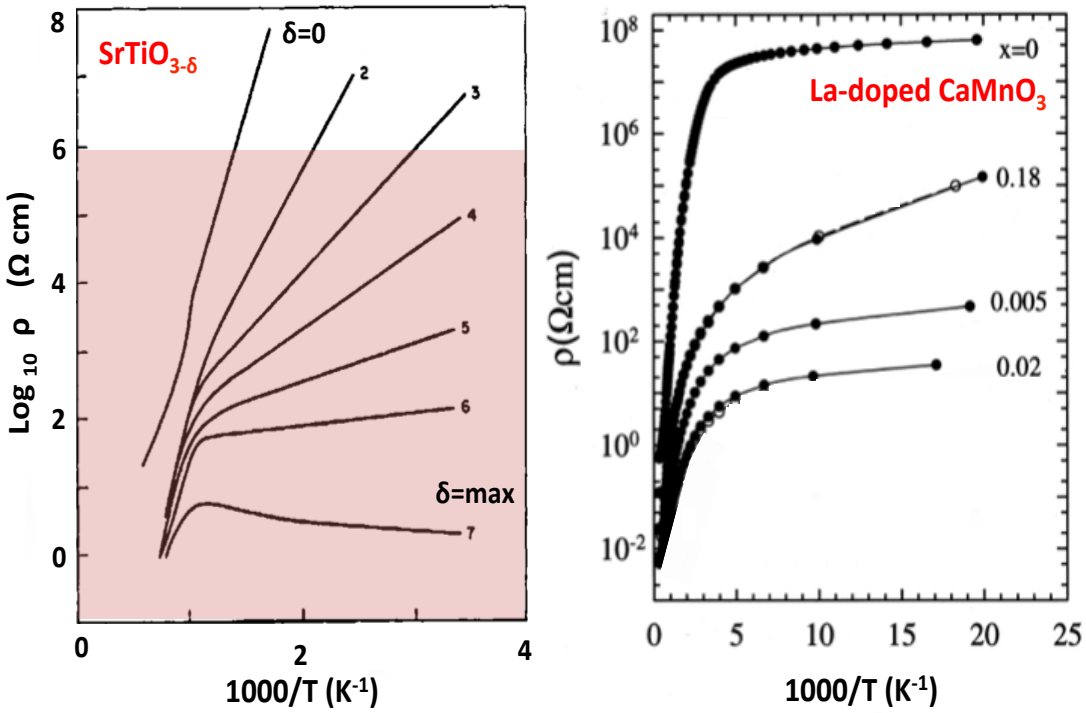

Figure 1.5: Similar effect of vacancy and electron doping on perovskite electronic properties. Left Panel: Log of resistivity vs. reciprocal temperature of oxygen deficient $SrTiO_{3-\delta}$ materials where resistivity is reduced from stoichiometric material producing semiconducting properties [39]. Right Panel: Semiconducting behavior due to thermal activation of impurity in La-doped $CaMnO_3$ manganite perovskites.

It has been shown that the presence of oxygen excess or vacancies can be easily accommodated in specific crystal structures such as found in rare earth manganites $RMnO_{3-d}$ [48]. In $Sr_{1-x-y}Ca_xNd_yTiO_3$ materials of chapter 4, the oxidation states of the *A*-site cations are varied but nonetheless we will neutralize the complicating effect of vacancies by maintaining stoichiometric materials for the purpose of drawing clear correlations between physical and structural properties where any amount of vacancies only adds to the complexity of the analysis. Therefore, what might give rise to the semiconducting behavior is instead the formation of Ti^{3+} ions via Nd doping similar to the second example shown in Fig. 1.5.

The presence of mixed valence transition metal oxides affects the properties to a various degree. The initially antiferromagnetic $LaMnO_3$ (Mn^{3+}: e_g^1) Mott insulator (large on-site Coulomb U= 8-10 eV [46]) becomes metallic ferromagnetic by the double exchange of the e_g electron hopping between Mn^{4+} and Mn^{3+} sites when doped with 20 % Alkaline earth elements such as Sr (Mn^{4+}: empty e_g^0 states) [49, 50], whereas the opposite insulator-metal transition is observed in $Pr_{0.5}Sr_{0.5}MnO_3$ at 140 K [51].

Conductivity behavior of titanate perovskites can be complicated by the interaction of charge carriers with the lattice. Evidence for formation and conduction of polarons due to strong electron-lattice interactions has been accumulating for $ATiO_3$ (A=Sr or Ba). In n-type $SrTiO_3$, the weak electron-lattice correlations allowed for delocalized (large) polarons conduction and consequently the material shows metallic behavior [52]. On the other hand, a 2 % increase in lattice parameters for A=Ba has enhanced the electrical resistivity of n-type B-site Nb^{5+}-doped $BaTi_{1-x}Nb_xO_3$ ceramics (wide gap insulators for x=0) and exhibits a semiconducting behavior for $0 < x < 0.20$ in which the conduction is explained by the non-adiabatic thermally

activated hopping of strongly localized (small) polarons on the isolated Ti^{3+} sites [53].

1.3 Structure-property Relationship in Perovskites

The first attempt to optimize the physical property via the study of crystal structure in perovskites was carried out on the first functional perovskite discovered, namely dielectric/ferroelectric $BaTiO_3$ which lead to the identification of many structural phases in this material [1]. The rise of dielectric constant to maximum value occurs at the ferroelectric transition temperature in $BaTiO_3$ [54].

Electron-electron correlations are to a large extent responsible for the complex relationship between the electronic and structural properties. These interactions include Hubbard Coulomb interaction of electrons on the same site and orbital with opposite spins (U $\sim$ 6–8 eV in typical perovskites), Hund's coupling (J$\sim$ 1 eV) which favors spin alignment of electrons in different orbitals on the same ion, ferromagnetic-favoring direct exchange interaction between electrons at different sites. Another type of interaction is Zener double exchange where Hund's coupling facilitates the motion of electrons (metallic state) in ferromagnetic ordered mixed valent materials. However, many of the transition metal oxides such as $CaMnO_3$ are antiferromagnetic (Mott) insulators due to combined effects of large U and the superexchange interactions mediated by oxygen ions as shown in Fig. 1.6 [25]; a situation we will encounter in chapter 5.

Size and/or thermal effects imposed on perovskites can be accommodated through different degrees of bonds expansion/compression, bond angles buckling/straightening, and octahedra rotation/tilting while the material is trying to sustain a specific crys-

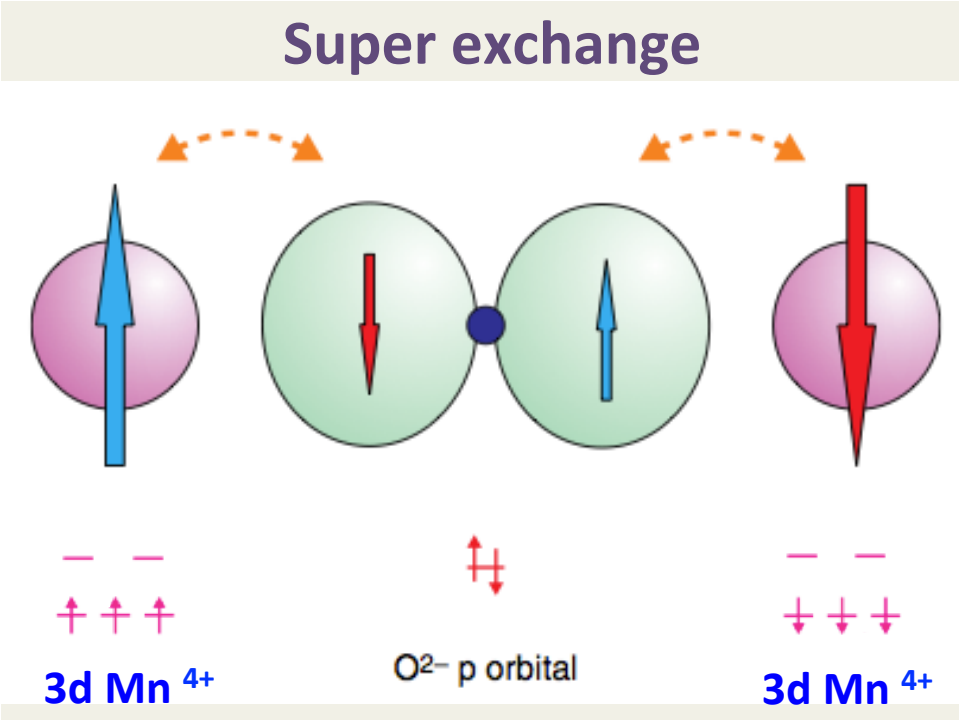

Figure 1.6: Schematic diagram of a 180° superexchange interaction between two paramagnetic Mn^{4+} cations via n oxygen ion. The interaction out come is predicted by the Goodenough–Kanamori–Anderson (GKA) rules and its strength which affects T_N is dependent on the degree of overlap between Mn^{4+} and O^{2-} ions (figure adapted from Ref. [1]).

tal symmetry. However, in most cases, local instabilities become large and a first or second order phase transition is observed. These structure transformations have important ramifications as they are intimately linked with changes in measured properties whether electrical, magnetic, mechanical, etc. Breaking the symmetry associated with different order parameters such as the spatial inversion symmetry, time reversal, and gauge symmetry in perovskites leads to the emergence of the phenomena of ferroelectricity, magnetic ordering and superconductivity, respectively [55].

Over many decades of research, it has been found that transition metal oxides span a wide range of properties including ferroelectricity [8], superconductivity [56,57] (ranging from T=0.7 K for reduced $SrTiO_{3-\delta}$ to well above 100 K in cuprates such as $TICa_2Ba_2Cu_3O_{10}$ [25]), colossal magnetoresistance [58], multiferroicity [59–61], spin-glass behavior [62], metal-insulator transition due to either strong correlation effects [63–67] or Anderson type localization [68] and much more with the crystal structure changing at the onset of the appearance, suppression, and enhancement of the majority of these properties.

I present in the next few paragraphs selected outstanding examples to showcase how *A*-site doping changes important structural characteristics and exhibit large coupling with the physical properties of perovskites.

In doped rare-earth manganite ($La_{1-x}A_xMnO_3$, A= Sr, Ca), it was suggested that in addition to the double-exchange mechanism one should also consider the influence of octahedral deformation to fully understand the measured resistivity data of its colossal magnetoresistance properties [69]. Systematic variations in the tolerance factor and one-electron bandwidth by doping induced critical changes of few order of magnitude in the resistivity in these colossal magnetoresistance perovskites [70].

Octahedral rotation at fixed band filling can change the electric properties drastically as in the Ca-doped $SrCrO_3$ ($3d^2$) compound where the doping with Ca ions causes the effective metallic (itinerant electrons) bandwidth W to become dramatically narrower and eventually the electrons becomes highly localized in $CaCr^{4+}O_3$ despite having the same levels of band filling as in its $SrCr^{4+}O_3$ counterpart [71].

The magnitude of tetragonal distortion c/a in $La_{1-x}Sr_xMnO_3$ dictates the type of magnetic ground state with magnetic ordering following the sequence; ferromagnetic, C-type, A-type, and finally the most conventional G-type AFM as a function of increased c/a ratio [72]. On the other hand, it has been shown that the ferro-

magnetic transition (Curie temperature) in Alkaline earth-doped $A\mathrm{RuO}_3$ ruthenates increases as a function of the average bond length and reaches a maximum value corresponding to a tolerance factor $t \sim 1$ [73].

The structural-property correlations are extensively studied in this thesis where I will discuss for example the correlation between antiferromagnetism ($\mathrm{T_N}$) and structural parameters (variance and bond angles) in the manganite systems as well as the tolerance factor effects on the thermoelectric properties in titanates.

CHAPTER 2

APPLICATIONS OF PEROVSKITE OXIDES

2.1 Thermoelectricity in Oxide Materials

Large amounts of today's energy ($\sim$ 66%) released from factories, plants and automobile are discharged into the environment as waste heat [74]. With limited natural resources and a fast-paced growth in consumer's consumption of energy, efficient and affordable sources of clean energy are in great demand. While revolutionary renewable sources such as solar, wind, and biofuels are still limited in use or in development stage to replace traditional energy sources worldwide, waste heat recovery is far more realistic and easy to implement and incorporate into current devices and means of transportation. Among the promising techniques to retrieve thermal energy is the thermoelectric process which involves using solid state units (no moving parts or greenhouse gas emissions). Search for good thermoelectric materials has witnessed a great surge in activities in recent years as shown in Fig. 2.1. Thermoelectric devices (generators) are now implemented in small-scale applications as temperature sensors and in space missions and satellites to generate electric power and can be useful for solar power utilization as well [75].

Thermoelectricity or the Seebeck effect, which refers to the mechanism by which a material is capable of converting heat gradient into voltage or electrical potential, has been known for almost two centuries dating back to the year 1821 when scientist Thomas J. Seebeck found that a nearby compass needle could be deflected by hold-

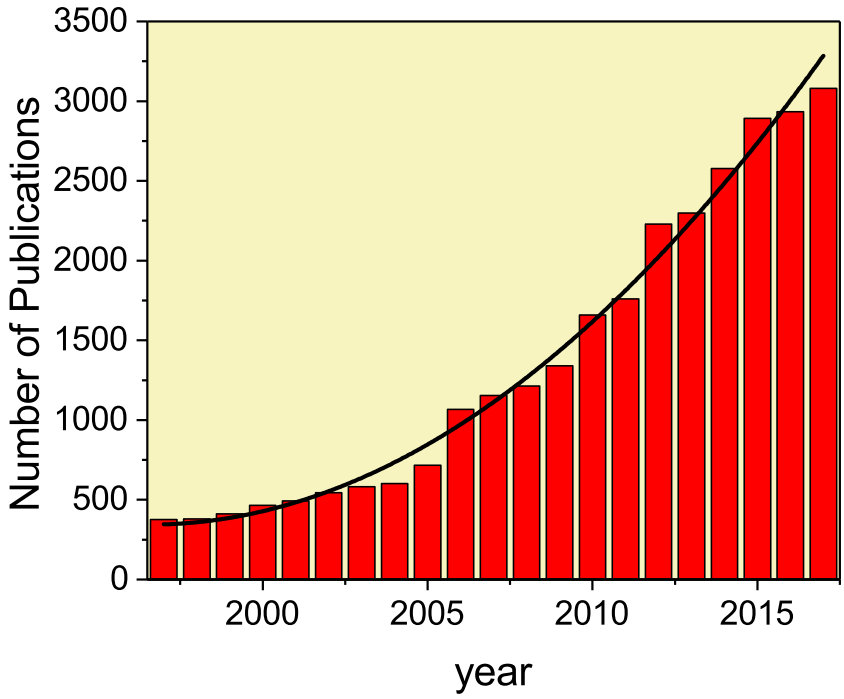

Figure 2.1: Exponential increase in the scientific community's interest in thermoelectricity and its applications measured by the number of publications per year for the last twenty years (1997–2017). Data obtained from the "web of science" database using the search topic "thermoelectric".

ing a metallic thermocouple's junctions at different temperatures which produced an electric current [76]. Fig. 2.2 shows an original diagram drawing of Seebeck's thermoelectric circuit in a book titled in German "Magnetische polarisation der metalle und erze durch temperatur-differenz" which translates into " Magnetic polarization in metals and ores due to temperature difference" [77, 78].

Microscopically, the thermoelectric (TE) effect is ascribed to the diffusion of heat carrying electrons under a temperature gradient ΔT that results in a potential difference $\Delta V = S\ \Delta T$ [80]. The constant of proportionality is known as the material's thermopower S or the Seebeck coefficient. Typical materials have a Seebeck coefficient on the order of a few microvolts/K whereas a potentially good

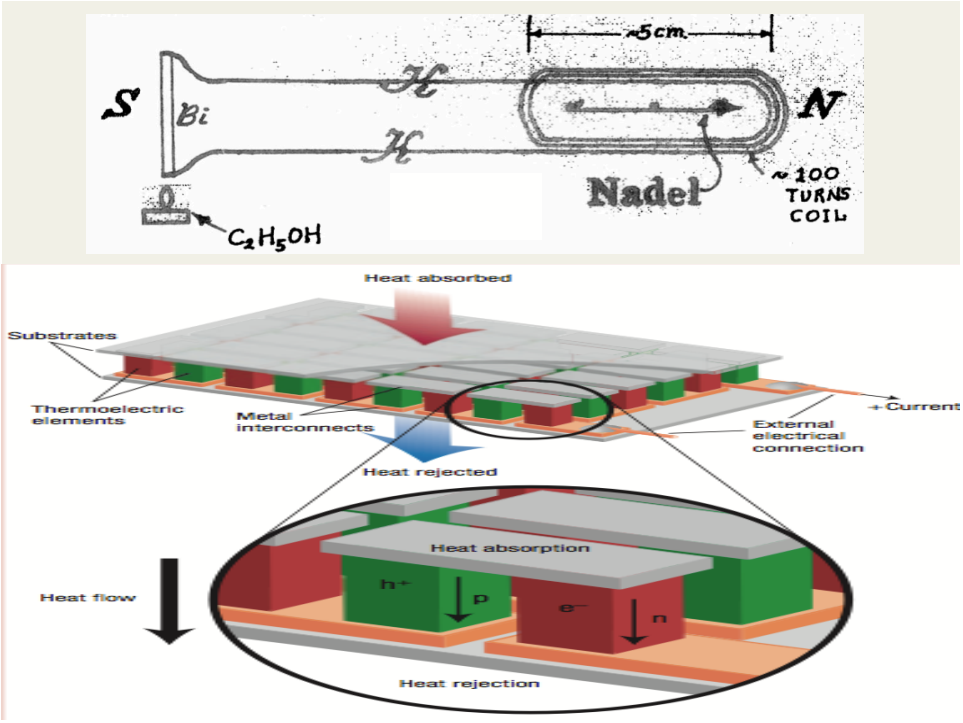

Figure 2.2: Top: Schematic diagram of TE process (Seebeck effect) from his original publication showing temperature gradient across two dissimilar metallic junctions (Bismuth and Copper) deflecting a compass needle. Bottom: A typical thermoelectric power generating device comprised of n- and p-type modules connected electrically in series and thermally in parallel (from Ref. [79]) using the same operational basis as that in the original Seebeck experiment.

thermoelectric material is capable of producing hundreds of microvolts per Kelvin [80, 81].

Instead of taking on the impractical task of applying a large temperature gradient ΔT across a material, researchers in the field have realized early on that successfully developed materials with large thermopower values would allow any small increase in temperature to be adequate enough to produce considerable potential difference. Most of the early studies concentrated on metals and alloys which have small thermopower (≤ 10 μV/K) and it was not until the beginning of last century when Altenkirch showed a systematic way of searching for good *TE* with a unified

criterion [82]. The basic requirement in principle for any good TE material is to have low thermal conductivity (preventing the state of thermal equilibrium), high electric conductivity (equivalently high mobility) and a large Seebeck coefficient to maintain high potential difference across the material.

A universally agreed upon gauge of the efficiency of a thermoelectric device in given by Abram Ioffe's dimensionless figure of merit $ZT = S^2\sigma(\kappa_e + \kappa_L)^{-1}T$ [83,84] which is a function of several transport coefficients. S, σ, and κ represent the Seebeck coefficient, electrical and thermal (electronic and lattice contributions) conductivities, respectively, with ZT values equal to or greater than 1 being highly desirable for efficient energy conversion with no theoretical limitations on its maximum value. However, the road to increasing ZT does not always run smooth as these thermoelectric parameters are strongly coupled with each other and are sensitive to the materials' lattice and electronic properties. The figure of merit ZT is part of the heat-electricity conversion efficiency η of a thermoelectric power generator [85,86] given as

$$\eta = \left(\frac{\Delta T}{T_2}\right) \frac{(1+ZT)^{1/2} - 1}{(1+ZT)^{1/2} + \frac{T_1}{T_2}} \tag{2.1}$$

Where the first term is the conventional Carnot efficiency ($\Delta T = T_2 - T_1,\ T_2 > T_1$).

The ultimate sought-after goal in the search for good thermoelectric material is to achieve Slack's "phonon-glass electron-crystal PGEC" state [87] in which thermal conductivity approaches that of an amorphous material while its electrical conductivity and mobility are characteristic of a perfect single crystal. The direct correlation between reducing thermal conductivity and increased average atomic weight was established by Ioffe around 1950 in isostructural semiconductors [82] as

shown in Fig. 2.3 and compared to the recent advancement in reducing the lattice thermal conductivity κ_L in skutterudite family which represents a good example of materials in which Slack's PGEC concept is practically realized. It is worth mentioning at this point that we succeeded in reducing κ_L of some of the materials studied in chapter 4 below the limit achieved by filled skutterudites in the inset of Fig. 2.3.

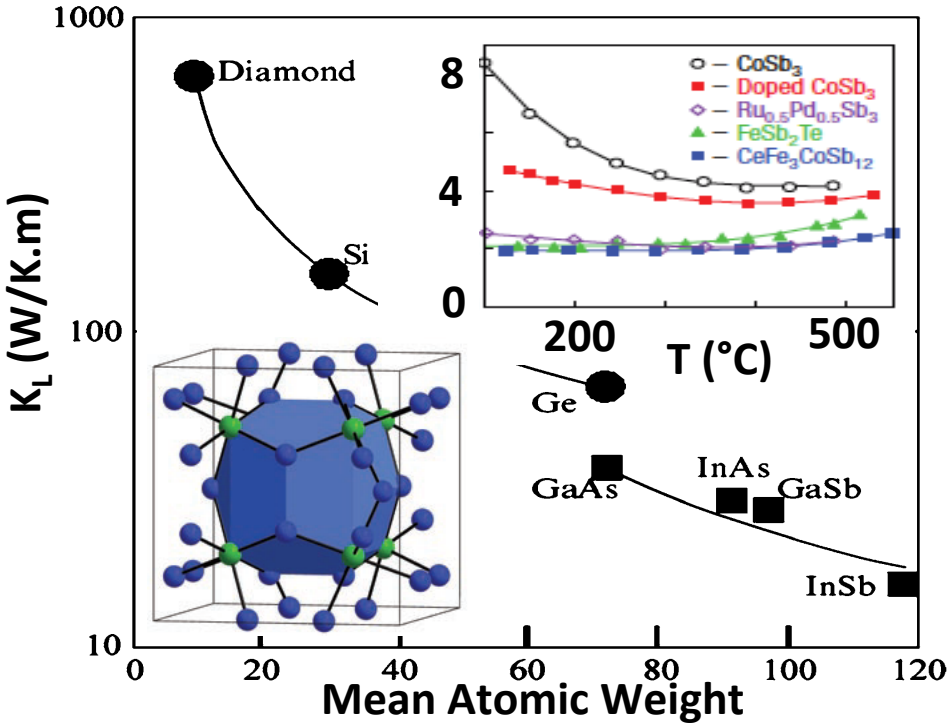

Figure 2.3: First established correlation between lattice thermal conductivity and mean atomic weight for isostructural materials as studied by Ioffe [82]. Inset shows the cubic structure of skutterudite $CoSb_3$ ($Im\bar{3}$) (Sb is blue, and Co is green color) with large voids created by tilting octahedra that can be filled with weakly-bonded small size heavy rare-earths to reduce κ_L by its strong thermal displacement (rattling) modes (insets from ref. [79]).

The first two TE parameters in the ZT expression trend inversely due to their strong and opposite dependence on the charge carrier density n [76, 88]; thus making the optimization of ZT inherently difficult. They together define a useful TE

quantity known as the power factor $PF = S^2\sigma$ [76]. I will provide throughout the remaining of this chapter a few examples of TE materials with large PF values yet with poor thermoelectric properties because the third term in Ioffe's ZT expression, namely the thermal conductivity, is large.

Implementation of the exact and standard theory of the thermopower given by Kubo formalism is not particularly useful for strongly correlated condensed matter systems where Mott showed that S is a function of density of states at the Fermi level [82]. Heikes formula of the thermopower, originally developed to describe S behavior in narrow band semiconductors [89], provides a good approximation to Kubo formalism where effect of correlations is reduced to the change in the entropy of the system. This theory describes the physical origin of Seebeck coefficient [90] for oxides based on the concept that S is related to the temperature gradient ΔT through the thermodynamical entropy s as:

$$S = \frac{q^2 R}{t} - \frac{T\partial s}{\partial T}\Delta T \tag{2.2}$$

In narrow band semiconductors as well as in the strongly correlated transition metal oxides, the thermoelectric properties are described based on a Hubbard model where the Hamiltonian of the system is a result of the competition between transfer integral of charge carriers between neighboring sites and the on-site Coulomb interactions. In the high temperature limit ($t << k_B T << U$) and initially ignoring the spin and orbital degeneracies, statistical mechanics treatment (site degeneracy (g) of N spineless fermions) gives the Seebeck coefficient as [91]

$$S_{(T\to\infty)} = -\frac{K_B}{e}\left(\frac{\partial ln g}{\partial N}\right) \tag{2.3}$$

Using Stirling's approximation, we arrive at the well-known Heikes formula with S rewritten as a function of the ratio of charge carriers to the transition metal sites

$$S_{(T\to\infty)} = -\frac{K_B}{e}\left(ln\frac{1-n}{n}\right) \tag{2.4}$$

Since the entropy is related to the degeneracy of electronic states, Eq. 2.4 predicts a further enhancement in the thermopower S if the d band of the transition metal perovskites is degenerate. Koshibae et al [90] applied Heikes general formula to specific strongly correlated material (cobaltite oxide) and found that the thermopower S would reach an optimal and temperature independent value that is determined exclusively by the site degeneracy as well as the orbital and spin degeneracy of electrons in mixed Co^{3+}/Co^{4+} sites.

Applying the same analysis to $Sr_{1\text{-}x\text{-}y}Ca_xNd_yTiO_3$ materials studied in chapter 4. the degeneracy is given as

$$g = g_3^{N_3} g_4^{N-N_3} \frac{N!}{[N_3!(N-N_3)!]} \tag{2.5}$$

Where N is the total number of available transition metal sites in the system (1 site per unit cell) and N_3 is the number of particles (electrons) which gives

$$S_{(T\to\infty)} = -\frac{K_B}{e}\left(ln\frac{1-y}{y} + ln\frac{g_3}{g_4}\right) \tag{2.6}$$

The variables y ($= N/N_3$), g_3 and g_4 in Eq. 2.6 correspond to Nd content (y), degeneracy of 3d electrons in the mixed valence state of Ti^{3+} and Ti^{4+}, respectively for this system which can be rewritten explicitly as $Sr_{1\text{-}x\text{-}y}Ca_xNd_yTi^{4+}{}_{1\text{-}y}Ti^{3+}{}_yO_3$ with ($lng_3/g_4 = ln2 + ln3$) representing the spin and orbital degrees of freedom of the ground state of t_{2g} 1-electron in 3d orbitals as shown in Fig 2.4.

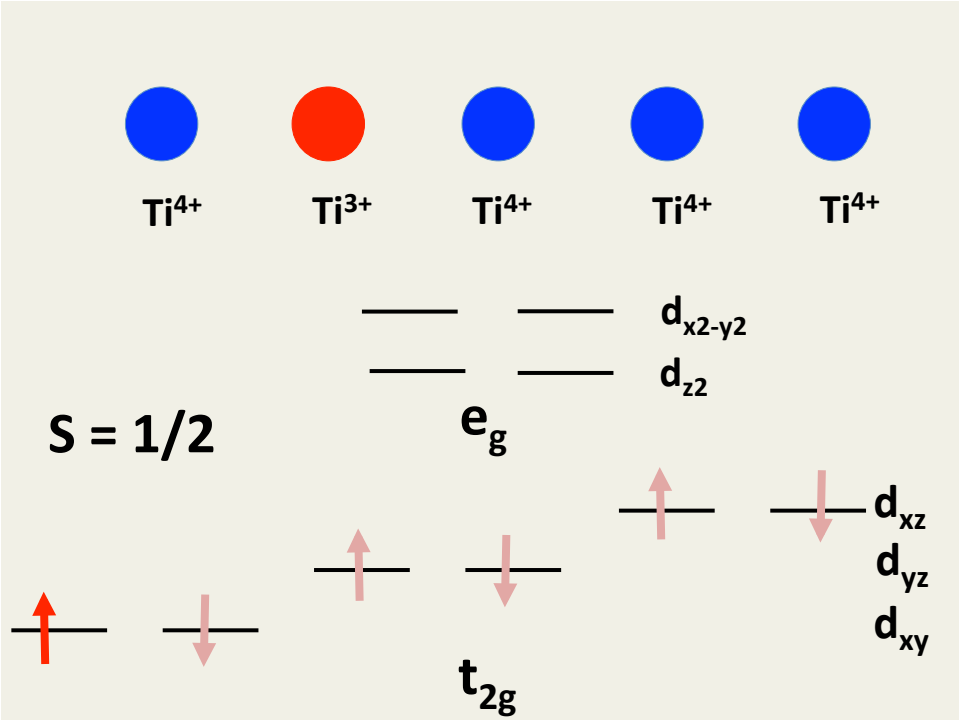

Figure 2.4: Different possible states of site/orbital degeneracy of electrons in the mixed valence $Ti^{3+}(Ti^{4+})$ of $Sr_{1-x-y}Ca_xNd_yTiO_3$ corresponds to the amount of Nd present in the system where each Ti^{3+} ion generates a charge carrier in the 3d band that has 6 total spin and orbital degrees of freedom.

Thermal conductivity, κ (in units of W/m.K) is the third TE parameter which appears in the partial differential equation of heat diffusion in solids and is defined as the rate at which heat is transferred through a surface area A of a material in the presence of a spatial temperature gradient as given by the formula:

$$\frac{dQ}{dt} = -\kappa A \frac{dT}{dX} \tag{2.7}$$

In metals and degenerate semiconductors, electrical and thermal conductivities are intrinsically linked with direct proportionality $\kappa/\sigma = LT$ as expressed by the Wiedemann-Franz law [76]. To develop a good sense of the role that thermal conductivity plays in the effectiveness of TE material, lets examine the hypothetical

situation in which a metal has small lattice thermal conductivity. Then, the figure of merit ZT becomes only function of the thermopower ($ZT = S^2/L$) and an S value $\sim$ 270 μV/K would easily raise ZT to $\sim$ 3 [82]. Because of their high electrical conductivity, metals also conduct heat very efficiently and this is the reason behind their poor TE performance compared to semiconductors as shown in Fig. 2.5 which presents a qualitative analysis of the TE characteristics of different materials classified based on their charge concentration. The remarkable influence of the electronic structure (carrier concentration) on ZT values is evident from this figure. Large S values are found in low charge concentration semiconductors or insulators while large electrical conductivity demands large carrier concentration. Thus, we can see that the values that maximize PF correspond to carrier concentration range n $\sim 10^{18}$–10^{20} cm^{-3} typically found in extrinsically doped semiconductors.

Typical TE parameters values are compared in Table 2.1 for different classes of materials and for a representative sample from chapter 4 which shows that the best compromise is achieved in the semiconducting regime where ZT often reaches maximum values that could exceed ZT= 1.5 as found recently in SnSe single crystals (ZT = 2.6 at 900 K) [92] and $Bi_{0.5}Sb_{1.5}Te_3$ with ZT that peaks to 1.9 at 320 K [93].

All of the ZT components except lattice thermal conductivity are reliant on the electronic band structure of the materials. As shown in Fig.2.5, the electronic contribution κ_e to the total thermal conductivity is small in oxides (around $\sim$ 15% or less [97]). In materials with strongly correlated electrons ($U >> W$) like the titanate perovskites, transport properties are governed by the hopping amplitude and greatly dependent on the electronic wavefunction overlapping between Ti–O orbitals. High mobility ($\sigma = \mu ne$) is essential for achieving good TE results. Oxides in general have long been considered poor thermoelectrics because of the low carrier

Table 2.1: Comparison of TE properties of different classes of solids and their corresponding power factor and ZT values including a representative sample from materials studied in chapter 4.

Material	S (μV/K)	σ (Ω^{-1}cm^{-1})	PF ((mW/ m-K^2))	κ (W/K.m)	Z (K^{-1})	ZT (T=300 K)
Typical Insulators [94]	~ 1000	$\sim 10^{-12}$	-	$\approx \kappa_L$	5×10^{-17}	very small
Typical Semiconductors [94, 96]	~ 200	$\sim 10^3 (10^{-4} - 10^3$	~ 4	$\approx \kappa_L$	2×10^{-3}	~ 0.6
Typical Metals [94]	~ 5	$\sim 10^6$	~ 2.5	$\approx \kappa_e$	3×10^{-6}	9×10^{-4}
$Sr_{0.76}Ca_{0.16}Nd_{0.08}TiO_3$ (chapter 4)	133	10^2	~ 0.18	3.5	-	0.07
Heavily Nd-doped $SrTiO_3$ [34]	100	10^4	3×10^{-3}	12	-	-
$Ca_3Co_4O_9$ [97]	120	300	1	~ 3	-	0.08
$SrTi_{0.8}Nb_{0.2}O_3$ (T=1000K) [38, 97]	200	450 (thin film , RT [98])	1.3	3.5	-	0.35
$NaCo_2O_4$ [81] (Single crystal)	100	5×10^3	5	1.5	1	-
Bi_2Te_3 [86, 99]	$220 - 225$	1000	4	1.5	-	1
$SrTiO_3$ single crystal [34] (Single crystal)	390	10	-	12	-	0.005

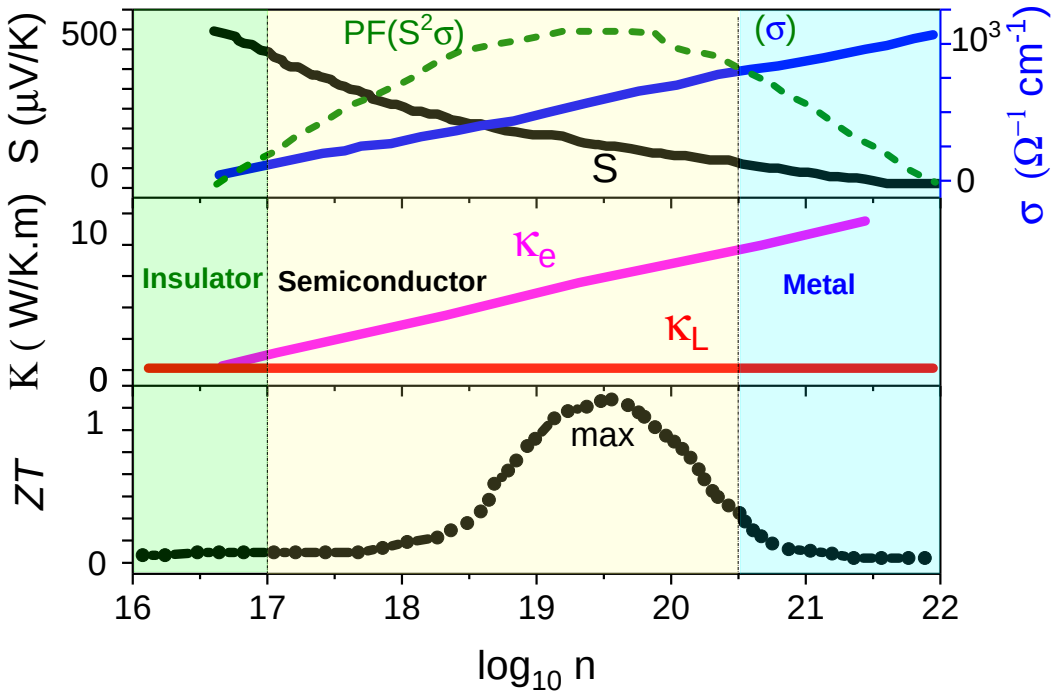

Figure 2.5: "Qualitative" picture of the complex intricacy between different TE parameters in solids as classified according to their carrier concentrations where ZT peaks at carrier concentration of $\sim 10^{19}$–10^{21} cm^{-3}. In chapter 4, we will transform the dielectric (insulating) $SrTiO_3$ oxide into an n-type semiconductor by Nd doping and hence the materials will acquire enhanced semiconducting thermoelectric properties. (Fig. adapted from Refs. [79, 82, 94, 95]).

mobility and strong electrons localization. The effect of low mobility on reducing ZT is evident as will be examined in chapter 4 where the small polarons formed in heavily doped samples (Nd=20%) of $Sr_{1-x-y}Ca_xNd_yTiO_3$ materials are characterized by low μ and hence their ZT values are considerably smaller compared to lightly doped samples.

With the basic theory of thermoelectricity outlined above, we will now examine the current status of the field in terms of best potential thermoelectric materials. Thermoelectric materials provide one key avenue for tackling the multifaceted and long-standing global challenge of meeting the increasing demand for alternative en-

ergy. Advancements in the field of thermoelectricity have accumulated rapidly and the search for good thermoelectric materials has progressed from the early use of simple metals by Seebeck to the development of nanostructured and quantum dot materials [100, 101]. Many semiconducting alloys such as Sb_2Te_3, SnTe, $Si_{1-x}Ge_x$ and Bi_2Te_3 (present day conventional thermoelectrics) had received an early stage recognition and were examined and classified as good thermoelectric materials by Haken around 1910 [102] and even promoted as alternatives to traditional power generating resources around 1950 [103].

Despite being good *TE* materials around room temperature with high mobility μ, semiconducting alloys [76,80] are examples of conventional thermoelectric materials that become unstable at higher temperatures [80]. The operational temperature range of *TE* semiconductors is severely limited by a reduced thermal stability of their structure which leads to deteriorating figure of merit values with temperature as depicted in Fig. 2.6 for common n-type and p-type *TE* semiconductors [79].

Another example of the many limitations that might stand as a barrier against their wide-use implementation is the economical inefficiency. Additionally, with the increasing environmental awareness in recent years, some semiconductors are hazardous and cannot be widely implemented for wide-range industrial and commercial use. As scientists have come to realize these unfortunate limitations, the gear soon shifted towards exploring transition-metal oxides as potential alternatives [39, 80, 83] thanks to their relatively low cost production and oxygen-reinforced stability at high temperatures. Built-in oxygen in these materials maximizes their potential for capturing and recycling wasted heat from automobile exhausts and industrial plants, i.e. for mid-to-high temperature applications [83]. As I mentioned above, possessing a high power factor $PF(= S^2\sigma)$ does not typically classify a material as good *TE* candidate unless it simultaneously exhibits a substantial

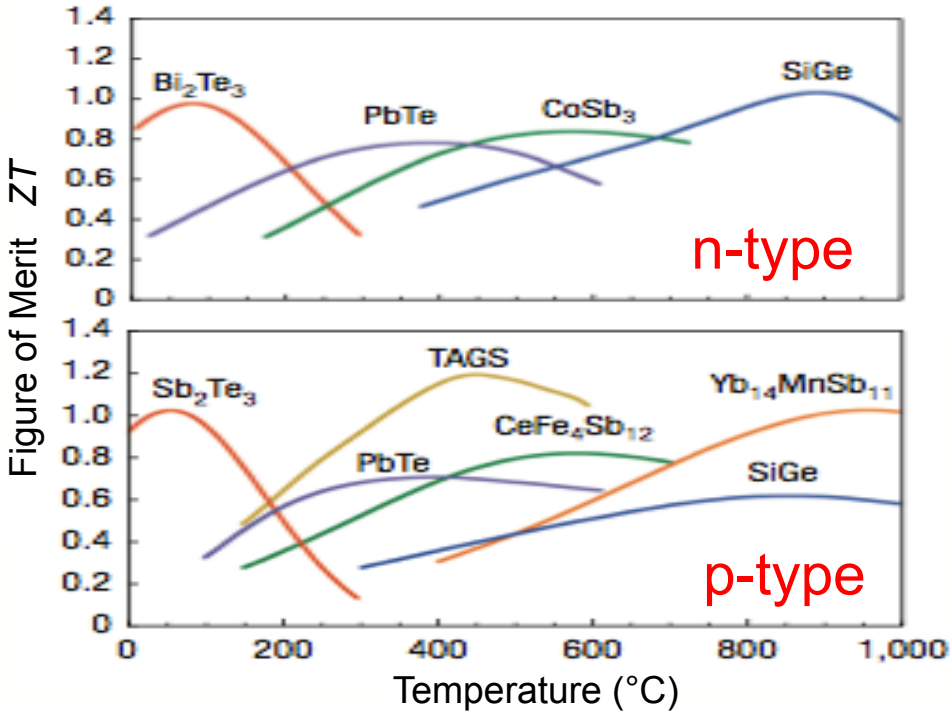

Figure 2.6: ZT vs. T curves for some conventional n-type and p-type semiconducting materials [79] where significant deterioration occurs at medium to high temperature regions limiting their capability of recycling waste heat. TAGS refer to alloys of Te-Ag-Ge-Sb.

reduction in its thermal conductivity. Recent discoveries of oxides with PF values that surpass TE semiconductors have sparked interest into optimizing their thermal conductivity to achieve the highest possible ZT which is quite challenging because of intrinsically high lattice thermal conductivity due to the presence of light oxygen anions in oxides.

A standard thermoelectric module comprises a pair of p-type and n-type elements as shown in Fig.2.2. Among the studied bulk oxides, p-type cobalt-based materials stand out as highly promising TE candidates. Examples of layered cobaltites exhibiting large ZT values that approach unity include $NaCo_2O_4$ single crystals

($ZT \sim 1$ at 800 K, and PF larger than that of Bi_2Te_3) [76, 81, 104] and $Ca_3Co_4O_9$ ($ZT \sim 0.30 - 0.40$ at 1000 K) [97, 104].

On the other hand, in the area of developing n-type perovskite oxides such as $ATiO_3$ and $AMnO_3$ the progress has been much slower with most materials displaying modest ZT values. The $CaMnO_3$ compound upon A-site (B-site) doping with Pr (W) has a maximum ZT of only about 0.01 at 300 K (0.16 at 873 K) [105, 106] while the multiple site doping composition $Ca_{0.9}Y_{0.1}Mn_{1-x}Fe_xO_3$ gives $ZT \sim 0.02$ at 400 K for x = 0.05 [107].

$SrTiO_3$-based materials are currently at the forefront of exploration for good n-type *TE* oxides due to encouraging *TE* capabilities which far exceed that of their manganite-based counterparts owing to the large Seebeck coefficient (large carrier effective mass m* which is typically in the range of 6 to 10 m_o [97, 108]). The highest ZT value reported [38] is for 20% B-site Nb-doped $SrTiO_3$ ($ZT \sim 0.37$ at 1000 K, PF = 1.3 mW/mK^2) thanks to its low thermal conductivity whereas *TE* performance of A-site La-doped $SrTiO_3$ is severely limited [34] due to high phonon conduction despite a PF value that is comparable to that of Bi_2Te_3 [81]. Seebeck coefficient enhanced when band degeneracy that increases the density of states (DOS) is present around Fermi level [30]. Improved *TE* properties by modifying the shape of DOS in reduced dimensionality is realized for strongly correlated oxides in the $SrTiO_3$ superstructure with confined electron gas which was found to enhance the thermopower S to $\sim 850\,\mu V/K$ at room temperature [109].

Both the electrical conductivity σ and the Seebeck coefficient S of $SrTiO_3$-materials depend on the electronic doping level n (band filling) [67]. An equally important factor for determining transport and thermoelectric properties of the materials is the strength of the interactions between neighboring Ti atoms mediated by oxygen. These B–O–B interactions, which can be strong enough to change the

electronic state from localized to itinerant in some materials [35], are measured by the bandwidth W and hence they are sensitive to the degree of $< Ti\text{-}O\text{-}Ti >$ bond angle distortions. Additionally, significant variations in the [Ti-O] bond length could play an important role in influencing the *TE* or MIT properties [110].

The enhanced effective mass (and hence S) [38] in electron-doped $SrTiO_3$ is the result of orbital degeneracy or equivalently the entropy per carrier. La-doped $Sr_{1-x}La_xTiO_3$ [34] material exhibits a PF nearly three times larger (3.6 mW/mK^2); a value comparable to that of Bi_2Te_3 (4 mW/mK^2) [81]. In these materials, the La content was kept to a minimum (x = 0.1) just enough to enhance the n-type band filling while preserving the cubic symmetry necessary for optimal orbital degeneracy. The interesting *TE* capabilities displayed by these materials are mainly attributed to the orbital degeneracy of the Ti 3d orbitals (triply degenerate t_{2g} comprising the conduction band) [34]. These results demonstrate the importance of optimizing the orbital degeneracy by keeping the octahedral distortions small (large t factor and larger $< Ti–O–Ti >$ bond angles). Indeed, further splitting of the t_{2g} orbitals (lifting the degeneracy) into a doubly-degenerate e_g and a singly-degenerate lower orbital was found to lead to deterioration of the effective mass values and S in layered $Ca_3Co_4O_9$ perovskites [104], and in Nb-doped $SrO(SrTiO_3)n$ (n = 1, 2) materials [111]. Such undesirable distortion-induced effects on the effective mass were reversed in rare earth (RE)-doped samples by the gradual increase of the bond angle with increasing temperature leading to the successful restoration of the triply degenerate Ti 3d t_{2g} orbitals [111]. In some cases, however, breaking the orbital degeneracy by octahedral distortion as in $LaCoO_3$ helps stabilize the low spin configurations of Co^{3+} and Co^{4+} and leads to large thermopower properties [90, 112]. Structural distortion of MnO_6 in Sr-doped $LaMnO_3$ was found to lift the double degeneracy of the upper e_g band and S changes its sign from negative to positive accordingly

[113]. In the chapter 4 of this thesis, thermoelectric properties and figure of merit of the titanate system ($Sr_{1-x-y}Ca_xNd_yTiO_3$) will be examined thoroughly.

2.2 Multiferroicity in Oxide Materials

The unification of all physical phenomena into a single discipline or the theory of everything has always been the ultimate goal of physics which was realized in part for electricity and magnetism by the brilliant work of Maxwell. Experimentally, material's degrees of freedom (spin, charge and lattice) are often tangled exhibiting strong correlations as observed for example in the emerging field of spintronics which demonstrated the possibility of practical control of the coupling between electric current (charge carrying unpolarized spins) and the magnetically ordered materials it passes through.

We will find the investigated materials in chapter 5 ($Sr_{1-x}Ba_xMnO_3$, Mn^{4+}: $[Ar]4s^03d^3$) structurally described as ferroelectrics with magnetic ordering below $\sim$ 200K and hence these manganites are characterized as multiferroics. Multiferroics [114] in which two or more order parameters must coexist [115–118](see Fig. 2.7 [119]) are of great fundamental and technological interest because of their potential for impactful applications with a promise to revolutionize a wide range of consumer electronics in addition to space and defense industries. For instance, it has been demonstrated recently that magnetic skyrmions can be created in multiferroic materials for information storage and transfer [120]. A strong coupling between the ferroic order parameters is highly desired for successful device applications.

Although single-ferroic electronic or magnetic materials are relatively abundant; the combination of both orders in one perovskite material is relatively scarce and

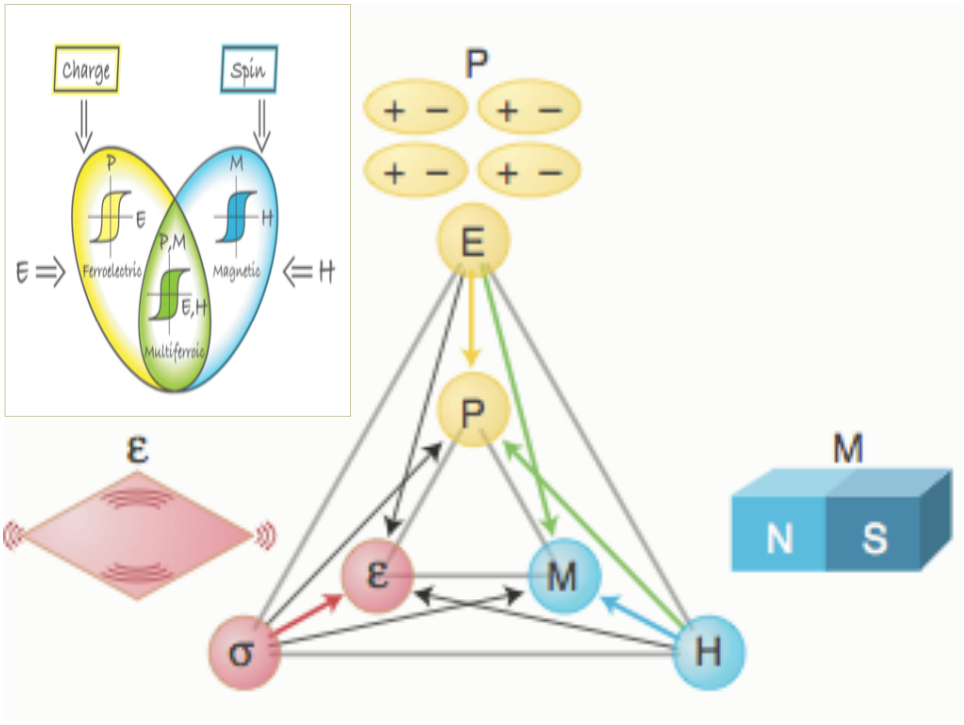

Figure 2.7: The interplay between different degrees of freedom ([119]) and the coexistence of two or more order parameters classifies the material as multiferroic.

the two orders have long been assumed to be mutually incompatible [116]. From crystallographic perspective, the reason for rare multiferroicity can be understood partially by noting that the majority of ferromagnetic point groups are centrosymmetric and spontaneous polarization is forbidden by symmetry rules [114]. As is the case for most strongly correlated materials where properties explained on the basis of Hubbard model, the correlation that exists between the apparent necessity for empty d orbitals and polar instabilities is a result of competition between kinetic energy-lowering overlap of B ions with oxygens and the increased on-site Coulomb interactions and hence ferroelectricity is often suppressed in transition metal ions with active d orbital electrons [118,121]. For example, it has been theoretically calculated that possible shifts of Mn^{4+} ($3d^3$) off octahedral center in $CaMnO_3$ leads to

significant increase in the ground state energy of the system ($\sim$ 160 meV/f.u.) [122] and thus the centrosymmetric non-polar Pbnm structure is more stable. From all these results, it is evident that stabilizing ferroelectricity requires a second stimulus which turns out to be the lattice strains. Thus, this energy barrier can be overcome and transition metals with d orbital electrons can turn into ferroelectrically active ions when materials are subjected to large lattice strains and relaxation of bonds via ions displacement becomes more favorable.

Of particular interest to this thesis is the relatively recent discovery of multiferroic properties in several oxide materials including $BiMnO_3$ [123], $Sr_{1-x}Ba_xMnO_3$ (SBMO) [124,125] and $BiFeO_3$ [117] in addition to a handful of other related rare-earth manganites [115, 126, 127]. While the sole microscopic source of magnetic ordering in these materials is the exchange interaction between localized magnetic moments, the ferroelectric distortion is driven by a number of distinctly different mechanisms. These include dangling bonds due to A-site lone pairs as in $BiMnO_3$ [123] and $BiFeO_3$ [117], charge ordering in $La_{0.5}Ca_{0.5}MnO_3$ [128,129], orbital ordering in $SrCrO_3$ [130] induced ferroelectric (FE) polarization by inversion symmetry-breaking helicoidal magnetic ordering as in the orthorhombic manganite $TbMnO_3$ [127, 131, 132] or Y-O mediated dipoles as in the hexagonal manganite $YMnO_3$ (combination of polyhedra buckling and displacement of Y ion) [133], all of which are in clear contrast with the origin of ferroelectricity in the prototypal FE $BaTiO_3$ which arises from the combination of empty $3d^0$-shells [134, 135] and large strains that force the off-centering displacements of the Ti^{4+} ions.

Ferroelectricity breaks the centrosymmetric crystal and a polar transition is accompanied by a loss of symmetry element as found for example in the recently discovered metallic $LiOsO_3$ perovskite oxide where the ferroelectric phase is characterized by a structural transition from centrosymmetric $R\bar{3}c$ to non-centrosymmetric

R3c [136,137]. Ferroelectricity enhancement in materials has evolved from the early attempts to realize multiferroicity by synthesizing mixed perovskites where two different ions occupy the B-site to independently give rise to magnetism and ferroelectricity [138] to a room-temperature ferroelectric polarization $\sim 130\ \mu C/cm^2$ from the recently reported tetragonal-like $BiFeO_3$ thin film where the enhancement of P_S has been attributed to a combination of a large strain-induced Fe-ion displacement and the Bi 6s lone pair electrons [139].

$BaTiO_3$ (Ba ionic radius $r_{Ba}^{XII} = 1.61$ Å) is one of the most widely used ferroelectric materials since its first laboratory preparation eight decades ago [1], see Table 2.2 for FE properties of few selected materials including a representative sample from chapter 5. On the other hand, the small A-site cationic sizes in $SrTiO_3$ (r_{Sr}^{XII} = 1.44 Å) and $CaTiO_3$ (r_{Ca}^{XII} = 1.34 Å) perovskites suppress the ferrodistortive mode despite sharing an identical TiO_2 sublattice with $BaTiO_3$. This emphasizes the significant role of steric effects (ionic size differences) in stabilizing FE disorder in perovskite oxides.

Multiferroics in general are classified into two broad categories depending on the origin of their multiferroic behavior. In type-II materials, magnetically induced polar distortion is a direct result of the complex spin arrangements of the crystal. To this category belong the perovskite manganites (large but light rare earth atoms) such as $TbMnO_3$ [127,131,132]. The sinusoidal spin density wave transforms into helicoidal arrangement under the strong influence of symmetry breaking exchange interaction between neighboring spins known as Dzyaloshinskii-Moriya interactions (DMI) that induces polar distortion [140,141]. Accordingly, the coupling between ferroic order parameters in type-II materials is expected to be large making this class of multiferroics superior to type-I counterparts in device applications. Large magnetoelectric effects desirable for effective electric field control of the magneti-

zation [142] has indeed been confirmed in orthorhombic $TbMnO_3$ crystals form the sudden suppression of the c-axis spontaneous polarization when applying magnetic field along the same direction [115, 126]. In type-I materials, ferroelectricity originate from various mechanisms as we mentioned above that are fundamentally independent of the influence of the present magnetic ordering. To this class belong hexagonal manganites $RMnO_3$ (R is a heavy and small size rare earth atom or Y).

The $Sr_{1-x}Ba_xMnO_3$ system was chosen here for examination of its multiferroic properties in particular because of its uniqueness as it combines the best of both worlds. It is type-I multiferroic and yet the two independent sources of FE and magnetism originate on the same MnO_2 sublattice promising a strong coupling between the ferroic order parameters.

Table 2.2: Ferroelectric properties of few materials including a representative sample from chapter 5 for comparison. The influence of doping on Curie temperature is clear and T_C is lowered by doping Zr for Ti for example while it increases by replacing Ba with Pb ions.

Material	T_C (K)	P_S Spontaneous polarization ($\mu C/cm^2$))	Ref.
Rochelle Salt (first FE)	296	0.25–1	[34]
$Pb(Zr_xTi_{1-x})O_3$ (PZT)	620	82	[143]
$BaTiO_3$ single crystal	394	26	[134]
$BaTiO_3$ strained thin film	-	50–70	[144]
$PbTiO_3$	766	50–80	[43, 134]
$KNbO_3$	691	30	[43]
$Ba_{0.6}Pb_{0.4}TiO_3$	573	-	[43]
$Ba_{0.6}Sr_{0.4}TiO_3$	0 (non polar)	0	[43]
$Sr_{0.55}Ba_{0.45}MnO_3$	362	29.5	Chapter 5

From Table 2.2, we see that $PbTiO_3$ has T_C that is nearly twice the 400 K of $BaTiO_3$, thus by doping the latter with lead in $Ba_{1-x}Pb_xTiO_3$ an increase in T_C was

made possible to $\sim$ 573 K [43]. The exceptionally large T_C in $PbTiO_3$ is due to large strains and the covalent character of Pb–O bonding which stabilizes the *FE* distortion to such a high temperature [134]. The *FE* properties of thin films are enhanced and $T_C \sim 300$ K in epitaxially strained $SrTiO_3$ for example [145].

CHAPTER 3

EXPERIMENTAL DETAILS

The polycrystalline samples of $Sr_{1-x-y}Ca_xNd_yTiO_3$ titanate materials studied in next chapter were successfully synthesized using conventional solid-state synthesis techniques. A total of ten samples were prepared forming two distinct series of the perovskite titanates $ATiO_3$ ($A = Sr_{1-x-y}Ca_xNd_y$), with the compositions in each series designed to exhibit a nominally constant magnitude of the tolerance factor. The first series is Sr-rich with Sr contents ranging between 73 and 80% while the second series is Ca-rich (Sr-poor) with Sr concentrations reduced to 50 – 57%. Both the series have the same Nd substitution levels (i.e., charge doping or band filling) of 0, 1, 3, 8 and 20 %.

Synthesis involved mixing proper amounts of highly pure (∼99.99% pure) powders $SrCO_3$, $CaCO_3$, Nd_2O_3, and TiO_2. Oxygen off stoichiometry in oxides considerably influences their transport and thermoelectric properties [146–148]. To ensure oxygen-stoichiometric materials, after calcinated compacted powder are pressed into disk-like pellets applying hydraulic pressure, the Nd-free samples were sintered in air at temperatures up to 1450 – 1480°C while Nd-containing samples (Nd_2O_3 is hygroscopic) were synthesized in a slightly reducing atmosphere 1– 5 % H_2/Ar at temperatures up to 1480°C.

On the other hand, pseudocubic $Sr_{1-x}Ba_xMnO_3$ manganite perovskites are metastable phases that can only form under stringent synthesis conditions [149]. For this work, high quality polycrystalline $Sr_{1-x}Ba_xMnO_3$ (with x = 0.43, 0.44, and 0.45) materials were prepared from stoichiometric mixtures of $SrCO_3$, $BaCO_3$,

and MnO_2. In chapter 5, I report in detail the results of the x = 0.43 sample at which ferroelectricity first appears, and the x = 0.45 sample which is the highest Ba concentration achieved in samples with better than 99% purity. In addition, synchrotron x-ray measurements performed on the x = 0.44 sample show that it exhibits properties similar to what would be expected for intermediate compositions between the x = 0.43 and 0.45 samples.

In contrast to $Sr_{1-x-y}Ca_xNd_yTiO_3$ titanates, the perovskite structure of $Sr_{1-x}Ba_xMnO_3$ manganites was stabilized in a two-step process to avoid its more energetically favorable hexagonal counterpart, see Fig 3.1. In a first step, single-phase oxygen deficient $Sr_{1-x}Ba_xMnO_{3-d}$ perovskite samples were obtained using standard solid-state ceramic fabrication methods with successive grinding and firing at temperatures above 1573 K. In the second step, the oxygen deficient samples are slowly annealed at lower temperatures in a Cahn TG171 thermogravimetric analysis (TGA) furnace in a pure oxygen gas flowing continuously at 100 sccm with heating/cooling rates of 1 K/min until all the oxygen vacancies are completely filled. In order to ensure equilibrium, the samples were soaked at 673 K for four hours. Compacted samples with masses between one and three grams were broken into smaller pieces to help improve the oxygen diffusion during oxygenation. Figure 3.2 shows the annealing cycle of the reduced $Sr_{0.55}Ba_{0.45}MnO_{3-d}$ sample as a function of temperature normalized to the final sample mass. The oxygen uptake occurs in a single-step starting at 450 K. The inset of the figure shows similar curves for other $Sr_{1-x}Ba_xMnO_{3-d}$ compositions treated under similar conditions. The oxygenation temperature at which oxygen vacancies are completely filled and the material becoming fully stoichiometric drops from ∼460 K for x = 0 to ∼420 K upon increasing the Ba content. Such clear correlation between the average ionic size of the A-site cations and the temperatures at which final oxygen content of the material

is stabilized has been repeatedly confirmed in other manganite systems [48]. It is also worth noting that the oxygenation process concludes much faster with larger concentrations of Barium.

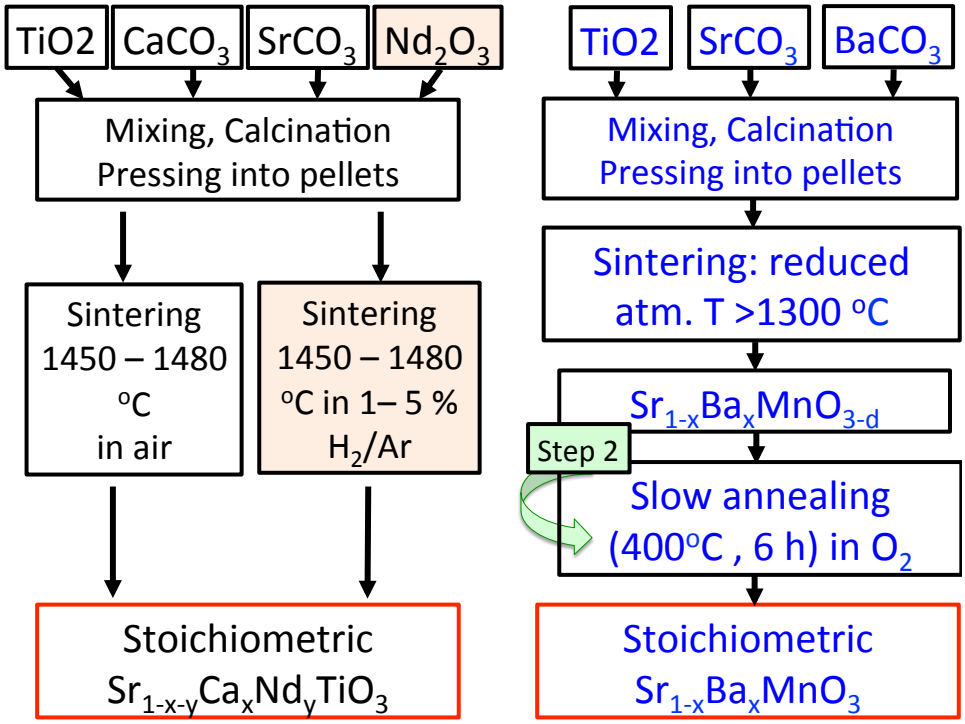

Figure 3.1: Conventional solid state reaction technique on the left for the synthesis of titanates vs. employing a two-step reduction-oxidation synthesis technique on the right in the case of manganites.

Additional high oxygen pressure annealing of a few hundred bars followed by very slow cooling to room temperature at a rate of 0.1 K/min were performed to ensure the full oxygen stoichiometry to within 0.01 oxygen atom/formula and that no additional oxygen can be incorporated. At a pressure of 225 bar and a temperature of 773 K for example, the careful weighing of the samples before and after annealing did not result in any discernable mass variation thus indicating no change in the oxygen content.

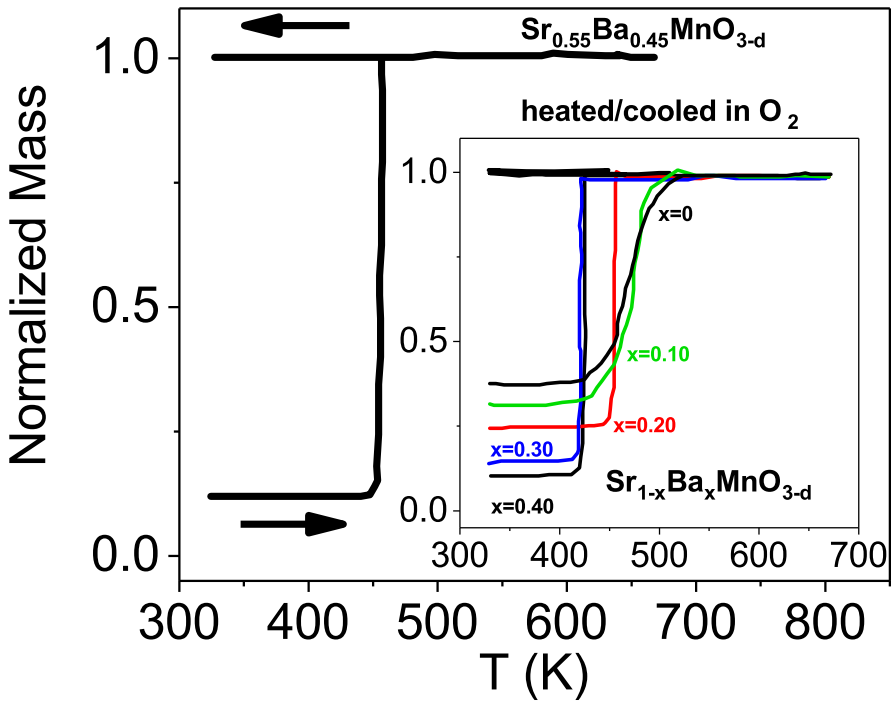

Figure 3.2: Thermogravimetric analysis (TGA) measurements for the as-synthesized $Sr_{0.55}Ba_{0.45}MnO_{3-d}$ sample on heating and cooling (indicated by arrows) in pure oxygen at 1 K/min and held at 670 K for four hours. Inset: Oxygen nonstoichiometry during heating the perovskite phases $Sr_{1-x}Ba_xMnO_{3-d}$ (x = 0.0, 0.1, 0.2, 0.3, 0.4) heated and cooled in pure flowing oxygen under similar conditions. The arrows indicate the direction of the temperature sweep.

Preliminary analysis of sample purity and phase formation was performed using in-house x-ray diffraction data collected at room temperature on a Rigaku D/MAX Diffractometer with CuKα radiation in the 2θ = 20 - 70° range. It is important to remember that oxygen non-stoichiometry in very common in complex oxides during synthesis imposes serious challenges for any attempt to structurally characterize the materials or to explore the complex structure-property correlations. The oxygen stoichiometry is determined for $Sr_{1-x-y}Ca_xNd_yTiO_3$ materials via a direct measurement of the oxygen content by oxidization at temperatures up to 1250°C which indicated from measuring the weight difference before and after air annealing that the initial

oxygen content was $\sim$ 3.00 oxygen atom per formulae unit with an uncertainty of no more than $\pm$0.01. On the other hand, refining the oxygen site occupancies in $Sr_{1-x-y}Ca_xNd_yTiO_3$ system using neutron powder diffraction data demonstrates that the oxygen content is fully stoichiometric for all the samples; see Table 4.4 presented in chapter 4 for the refined values. Additionally, monitoring the measured Seebeck coefficient of our samples (which is directly related to the carrier concentration and is exclusively dependent on the Ti^{3+} content), reveals nearly identical Seebeck coefficient values for each pair of same Nd content samples from the two Ca-rich and Sr-rich series (i.e. similar carrier concentrations) and provides evidence for our success to maintain a well-controlled oxygen stoichiometry through consistent synthesis procedures.

Transport and thermoelectric properties for $Sr_{1-x-y}Ca_xNd_yTiO_3$ materials were measured in the temperature range 10 – 400 K using a Quantum Design Physical Property Measurement System (PPMS) equipped with a Thermal Transport Option while DC magnetic measurements were performed for $Sr_{1-x}Ba_xMnO_3$ using a Quantum Design SQUID in external magnetic fields up to 70 kOe.

The common methodology in condensed matter physics for characterization of crystal structures and detection of any phase transitions a material might undergo microscopically is by the observation of the effect such transitions might produce on measured neutron or X-ray diffraction data through the concept of symmetry. Neutron powder diffraction (NPD), which is the primary investigative tool here that allows us to probe the various aspects of the materials structural properties, was performed for all the materials on the high-resolution time-of-flight third generation POWGEN diffractometer at the Spallation Neutron Source of Oak Ridge National Laboratory [150]. Neutron data were collected at temperatures 13 – 300 K for $Sr_{1-x-y}Ca_xNd_yTiO_3$ materials in the time-of-flight range of 10 - 80 millisecond which

corresponds to a d-spacing frame of 0.5 – 3.6 Å characterized by a wavelength centered at 1.333 Å (bank 3). For the multiferroic $Sr_{1-x}Ba_xMnO_3$ materials, data were measured for four-gram samples of $Sr_{0.57}Ba_{0.43}MnO_3$ and $Sr_{0.55}Ba_{0.45}MnO_3$ between 10 and 450 K with the diffraction patterns collected on heating with temperature increments of 20 K over two different d-spacing frames with central wavelength of $\lambda = 1.066$ and 2.665 Å in order to capture the possible diffraction peaks at low Q (high d values) that could arise due to magnetic ordering of the Mn sublattice.

Data was also collected on the high resolution synchrotron powder diffraction beamline 11-BM-B at the Advanced Photon Source of Argonne National Laboratory for some $Sr_{1-x-y}Ca_xNd_yTiO_3$ materials and for $Sr_{1-x}Ba_xMnO_3$ with x=0.43 - 0.45 compositions at temperatures between 140 and 440 K with increments of 5 K.

Data analysis of both titanate and manganite materials was performed using the Rietveld technique of full-matrix-least-squares as implemented in the GSAS/EXPGUI software suite [151,152]. Background, peak-profile and other general variables were refined simultaneously with the lattice parameters, atomic positions, magnetic moment and isotropic thermal factors. The background was modeled using shifted Chebyschev polynomials (type 1). The effect of the instrument and sample microstructure on the diffraction peaks is taken into account by modeling the peak shape with a pseudo-voigt function (identical to function type 3 in GSAS).

Figure 3.3 shows schematically a top view of the design of time of flight (TOF) POWGEN diffractometer instrument [150]. In this time of flight set up, neutrons which are quantum mechanical wave particles are produced at the core of the apparatus as a result of collisions between highly accelerated protons (hydrogen ions) and the nuclei of heavy metals such as Ta or U. This type of neutron-producing nuclear reaction known as spallation results in the emission of high-energy (hot) neutrons. Particularly useful to the study of crystal structures are neutrons with

wavelengths comparable to atomic sizes, i.e. the thermal neutrons which have wavelength ranging between 1–2 Å. For that purpose, the velocity of neutrons is tuned such that λ is of the order of the separation between atoms in the crystal structure and fast neutrons are slowed down by H_2 moderators and neutrons emerging with a spectrum of wavelengths ranging from hot (high frequency) having $\lambda \sim 0.3$ Å while wavelength of cold ones (small frequency or low speed $mv^2/2 = k_B T$) $\lambda \sim 2.4$ Å. .

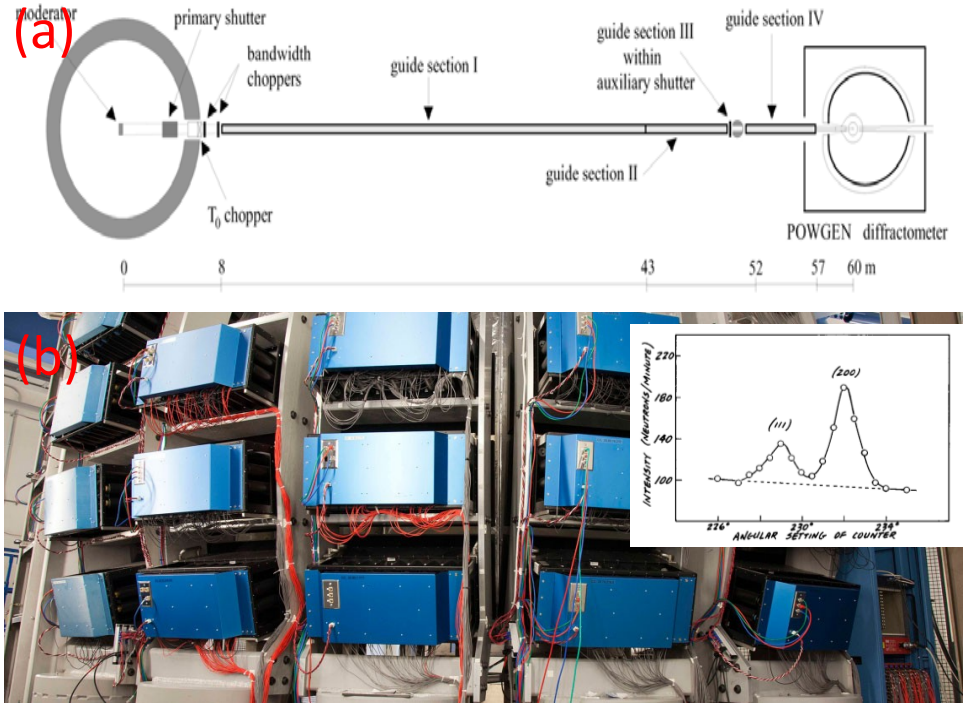

Figure 3.3: Top: A schematic drawing of the time-of-flight POWGEN diffractometer showing the total path from source to the sample [150]. Bottom: A photograph of the instrument shows the arrays of detectors that cover a wide solid angle with 2θ range of 20 – 150°. Inset shows portion of one of first neutron diffraction pattern recorded on double-axis neutron spectrometer where background is comparable to the peak intensiites [153].

The overall resolution of the diffractometer is defined by the change in spacing separating inter-planes ($\Delta d/d$), which determines plane reflections distinguishability (d spacing uncertainty). The factors that determine the resolution of the diffrac-

tometer are the scattering angle, total path, and time of flight according to the following expression for the TOF instrument arrangement [154].

$$\frac{\Delta d}{d} = \left(\Delta\theta^2 \cot^2\theta + \frac{\Delta t^2}{t^2} + \frac{\Delta L^2}{L^2} \right)^{1/2} \tag{3.1}$$

Therefore best resolution is always obtained with backscattering detector banks ($2\theta > 90°$). The peak resolution of Powgen instrument is $\Delta d/d = 0.0015$ at a d = 1 Å [150]. POWGEN is considered a high-resolution instrument due to its large total path (60 meters excluding sample to detector distance) which also increases time of flight of neutrons. We are analyzing in this study the data collected on high scattering angle detectors which will allow us to distinguish different structural distortions and/or phase transitions. Peak broadening is not only a function of the instrument factors but also depend on sample size and strains and the neutron path from sample to final destination (detector) is fixed at ~ 2 meters to reduce the finite size effect while maintaining large solid angle of scattering beam that reaches the detector.

The multiple detectors (contains high pressurized 3He gas that interacts with the neutrons to emit detectable rays) are fixed at specific angles (a combination of low angles, a 90°, and back scattering) that collect the scattered neutrons which arrive at the counter at different times that depend on their wavelengths (or speed v) governed according to de Broglie's dual wave-particle equation, $\lambda = h/mv$ (where h is Planck's constant and m is the mass of the neutron) from which the time of flight t is given as $t = mL\lambda/h$, L is the total flight path of neutrons from the pulse neutron source to the detector is 63.18 m for POWGEN.

To investigate magnetic peaks for the multiferroic samples ($Sr_{1-x}Ba_xMnO_3$) in chapter 5, measurements in the high d-spacing range in needed. For that purpose,

neutrons from a second frame of the POWGEN diffractometer corresponding to a range of incident wavelengths 2.2 – 15.2 Å are chosen in order to record the peaks for d spacing range up to $\sim$ 6.2 Å in a single measurement without sacrificing the high resolution of the peaks.

The neutrons beam is time sliced by two rotating choppers one of which is located near neutron source and one at the diffractometer end in order to prevent frame overlapping and to allow for large variations in the incident neutrons wavelengths (bandwidth) or velocities as the intense neutron pulse enters the neutron guides at pulse repetition rate (typical value is 60 HZ).

Neutron diffraction of any material is governed by Bragg law $\lambda = 2d \sin\theta$ for which the variables in the case of time-of-flight neutron diffraction are the neutron wavelength and d spacing. While electrons are primarily used to examine surface structures of materials, x-ray and neutron diffraction probe the bulk of materials. X-ray scatters effectively by the electronic cloud due to its electric field while neutral neutrons are capable of penetrating the electrostatic cloud to interact directly with the core nuclei (incident neutron-nucleus spin-spin interaction) and scatter coherently.

Neutrons are neutral and have magnetic moment (spin- fermions) and thus they are used to study the crystallographic structure as well as the magnetic properties of materials via neutron-unpaired electron spin-spin interaction. Attention to Neutron diffraction was first drawn around 1936 with a series of experiments that confirmed the diffraction of neutrons by crystalline materials. The first neutron diffractometer was built at Argonne National Laboratory in 1945 but was shut down in recent years. It took considerable time for the development of nuclear reactors to be mature enough for the useful application of the neutrons for research which explains the few operating facilities worldwide.

X-ray and neutrons both have comparable wavelengths but they differ in the scattering process. The difference is also intrinsically related to their physical nature since X-rays are electromagnetic waves while neutrons are neutral non-ionizing matter waves. The scattering amplitude of x-ray depends on the scattering angle [155]. Time of flight neutrons, on the other hand, scatter isotropically with minimum dependence on the angle of scattering and diffraction peaks maintain their intensity at high scattering angle (strong reflections at both long and short d-spacing range) while intensity of x-ray diffraction decays as the scattering angle increases due to the effect from the scattering factor f.

It is well known from the diffraction theory that the intensity of a peak with Miller indices (h, k, l) is directly proportional to the square of the structure factor or form factor which is a function of atomic positions (x,y,z) and scattering factor (strength) of individual atoms making up the unit cell. In the case of neutron diffraction, the equivalent parameter to x-ray scatting factor is scattering length b (in 10^{-15} m) which is an intrinsic property of the nucleus and hence is different for the isotopes of an atom and could even be negative as shown for Ti and Mn in Fig. 3.4 where arrows indicate values for some atoms comprising the materials studied in this thesis [155]. Assuming no energy transfer between neutrons and atoms (elastic scattering), the scattered flux intensity is given as the square of the scattering length b. The scattering amplitudes (scattering factor) of x-ray as shown in Table 3.1 depend heavily on the atomic number Z of elements making the detection and determination of atomic positions of light elements such as oxygen very limited. While the scattering length b of neutrons is atom-dependent and a function of its Z value, it however shows far less variations and the heavy atoms scattering power is reasonably comparable to the lighter ones. Only a handful of

atoms have weak interaction with neutron among which is the vanadium which is behind its exclusive use as sample holder material in diffraction experiments.

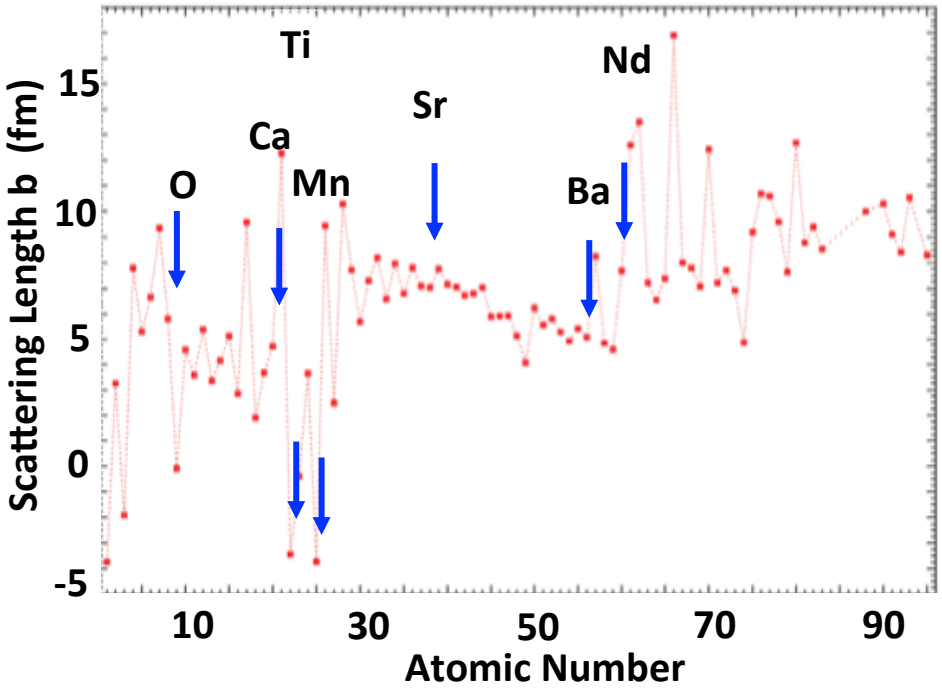

Figure 3.4: Neutron scattering length for the elements comprising materials studied in this thesis (value are in table 3.1 and compared to scattering factor from x-ray) indicated by arrows where both light and heavy weight atoms have comparable scattering power with variation is minimum [156].

The absorption of x-ray beam is a common property of all nuclei and it increases with increasing atomic number Z. While most neutrons are diffracted when interacting with atoms, neutrons can also be absorbed by the nucleus of an atom. Fortunately, absorption coefficients of most materials for neutrons are low. Almost all the individual atoms of materials investigated here have practically vanishingly small absorption cross-section. Diffraction experiments with few heavy rare-earth elements such as Gd and Eu are complicated because of their large absorption cross section. As shown in Table 3.2, Nd atom which is the only rare earth elements we

Table 3.1: Scattering factor dependence on atomic number in x-ray vs. angle-independent scattering length in the case of neutrons

Element	scattering length b Neutron ($\times 10^{-15}$ m)	scattering factor X-ray ($\times 10^{-12}(\sin\theta/\lambda)$
O 8	5.8	0.62
Ca 20	4.7	2.4
Ti 22	-3.4	2.7
Sr 38	6.9	5.2
Nd 60	7.5	9.0

incorporated in our materials has an absorption cross section of about 20 barn and also has a large incoherent (background) absorption cross section.

Table 3.2: Summary of the cross-section absorption $\sigma(\times 10^{-24} cm^2)$ by x-ray (1.54Å) and neutron diffraction (1.08Å) of the elements that make up the perovskite system $Sr_{1-x-y}Ca_xNd_yTiO_3$.

Element	Neutron absorption ($\times 10^{-24}$ cm^2)	X-ray absorption ($\times 10^{-24}$cm^2)
O 8	0.0001	305
Ca 20	0.25	10800
Ti 22	3.5	16500
Sr 38	0.70	18200
Nd 60	26	89700

CHAPTER 4

STRUCTURAL AND THERMOELECTRIC CORRELATIONS IN TERNARY $SR_{1-X-Y}CA_XND_YTIO_3$ TITANATES

4.1 Introduction

I present in this chapter the detailed measurements and analysis of thermoelectric properties of an elaborate $SrTiO_3$-based ternary system ($Sr_{1-x-y}Ca_xNd_yTiO_3$) with strong emphasis on the effects of electronic structure modification and the reduction of phonon conduction. Optimizing *TE* properties of a material for commercial use is widely regarded as a twofold challenge; one which is concerned with creating materials with low thermal conductivity κ and a large Seebeck coefficient S, and another which deals with understanding and exploiting the complex interactions between the material's structural and physical properties which largely influence its thermoelectric behavior. The importance of the work presented here stems from what I hope to be a successful disentanglement of the structural and thermoelectric properties in n-type $SrTiO_3$-based perovskite materials to whom our *A*-site substituted $(Sr_{1-x-y}Ca_xNd_y)TiO_3$ system belongs.

Substituted strontium titanates have demonstrated a strong potential for *TE* applications owing to high effective mass and large Seebeck coefficients. Apart from silicon, $SrTiO_3$ is one of the most common substrates in the thin film industry while its ferroelectric $BaTiO_3$ and $Ba_{1-x}Sr_xTiO_3$ counterparts have been used to

fine tune dielectric properties and improve their suitability for advanced spintronic applications. Additionally, a variety of isovalent and multivalent substitutions at either the Sr^{2+} or the $3d^0$ Ti^4 sites have been successfully accomplished leading to drastic structural modifications mediated by TiO_6 octahedral twists and tilts that give rise to luminescence [157], ferrorelectricity (FE), antiferroelectricity (AFE) [134,158,159], metal-insulating transitions (MIT) [35,160], and thermoelectric (TE) properties [38]. Ferroelectricity was successfully induced in $SrTiO_3$ by replacing O^{16} by the heavier O^{18} oxygen isotope [161]. By altering the oxidation state of Ti^{4+}, the transport properties of A-site (or B-site) chemically substituted $SrTiO_3$ can be drastically manipulated via injecting electrons into the conduction band of the otherwise empty $3d^0$ Ti^{4+} orbitals [34, 38]. Doped and reduced $SrTiO_3$ were reported to exhibit superconducting properties at low temperatures [162–164]. All of these results clearly demonstrate the strong potential of substituted strontium titanates which will be the subject of study in this chapter.

While intensive investigations have been carried out on A-site binary solid solutions like $Sr_{1-x}Ca_xTiO_3$ (SCT) or $Ba_{1-x}Sr_xTiO_3$ (BST), studies of ternary systems such as $Sr_{1-x-y}Ca_xNd_yTiO_3$ are relatively scarce. Perhaps this limitation is due in part to the compounded complexity of the diverse structural distortions that have so far been identified for intermediate SCT compositions [148, 165–176]. However, such an extensive range of possible distortion induced symmetries and properties make our goal to synthesize and investigate Nd^{3+}-substituted $Sr_{1-x-y}Ca_xNd_yTiO_3$ materials even more attractive and compelling.

Examined here at great length is how the double substitution of small ions like Ca^{2+} and Nd^{3+} at the Sr^{2+} site is used to tune the A-site ionic size and achieve specific constant or variable charge concentrations. The ionic size variance has served two primary purposes; while the smaller ionic sizes of Ca/Na maintain a fixed struc-

tural distortion as we increase Sr content in each series, electronic properties were systematically varied by Nd doping which generates extra electron by balanced formation of Ti^{3+} ions giving rise to B-site multi-valency (Ti^{4+}, Ti^{3+}) at the transition metal sublattice and promote a semiconductor-like temperature dependence of the conductivity. Two distinct $Sr_{1-x-y}Ca_xNd_yTiO_3$ series were designed and fabricated having nearly constant room temperature tolerance factor, t (nominal values of 0.997 and 0.993). This seemingly tiny difference in the tolerance factor has tremendous effects on the materials structure and final symmetry as will be demonstrated in the subsequent sections.

Varying the temperature at a fixed doping level leads to significant changes in the tolerance factor and hence to possible phase transitions [177]. In our materials, we expect the tolerance factor to increase progressively with temperature, as found in the related orthorhombic $CaTiO_3$ perovskite [27] for example (see section 1.1 of chapter 1), leading to structures with higher symmetries similar to those identified as tetragonal $I4/mcm$ and cubic $Pm\bar{3}m$ (when $t = 1$). It is clear that the strong dependence of the t factor on temperature leads to significant variations in the structural parameters (i.e. bond angles <Ti–O–Ti>and bond lengths) which in turn, at fixed band filling, cause a significant change of the electronic bandwidth $W(\sim \cos[(180° - < Ti\text{–}O\text{–}Ti >)/2])$ [178]. Using reliable structural information obtained by high-resolution neutron powder diffraction (NPD), this study is designed to pave the way for a solid understanding of the correlations between the structural ([A–O], [Ti–O], <Ti–O–Ti>, and t-factor), transport ($\sigma, n, m*, \mu$, and thermal conductivity κ), and thermoelectric ($S, PF, and\, ZT$) properties in this class of promising perovskite titanates. Additionally, this work will thoroughly address currently disputed structures and shed light on the aspects of phase transformations in perovskites that may occur as substituted trivalent atoms change the oxidation

state of the B-site transition metal. In addition to the analysis of the influence of small vs. large band filling on the electrical conductivity, I will investigate the effectiveness of Nd^{3+} doping (point defects) on reducing lattice thermal conductivity. Reproducing experimental data using well-established models allows us to uniquely identify different contributing sources of phonon scattering and thus opens a clear path towards optimizing TE properties of n-type oxide materials.

4.2 Structural Symmetries and Modeling

While the crystal structure of the end members of the binary solid solution $Sr_{1-x}Ca_xTiO_3$ is known to transform from cubic $Pm\bar{3}m$ to the tetragonal $I4/mcm$ symmetry [179] with an additional low temperature orthorhombic phase transition for $CaTiO_3$ (x=1) [27, 179], intermediate compositions have been intensively investigated in the past decade but remain controversial. While several groups [65, 168, 169, 171, 176] report an orthorhombic $Pbnm$ ($Pnma$) symmetry for only the $0.60 < x \leq 1.00$ Ca-rich members, others [169, 174, 176, 180] extend this orthorhombic distortion range to also include the $0.40 \leq x \leq 0.60$ members of the series. With even lower Ca concentrations, reports in the literature [165,168,180,181] suggest the structure of the $0.06 \leq x < 0.40$ compositions to have become tetragonal $I4/mcm$; however, other studies propose the orthorhombic $Ibmm$ symmetry for the compositional range $0.10 \leq x < 0.35$ [170, 173, 174, 176] and the formation of a superstructure with the $Pbcm$ symmetry [169,170,172,173,176] for $0.30 \leq x < 0.40$. For compositions with $x \leq 0.06$, most papers confirm the structure of these slightly doped materials as cubic [165, 169]. Furthermore, several other crystal structures have also been suggested from electron diffraction studies. For example, Woodward

and co-workers [171] have reported the existence of room temperature monoclinic distortions in the specific composition range $x > 0.2$ and $x < 0.6$ while Anwar and Lalla [148, 167] argued that the structure is rather orthorhombic $P2_12_12$ in the range $0.20 \leq x < 0.35$. This quick and nonexhaustive survey of the various reported space group symmetries gives a good sense of the simmering dispute within the research community over the correct crystal structure of this class of Alkaline earth titanates. In the following sections, I will examine the nature of these conflicting claims and determine which crystal structures are valid and which should be justifiably dismissed.

4.2.1 Monoclinic space group $P2_1/m$

The structural analyses on neutron direction patterns of perovskite materials are often performed by applying the principle concept that the rise of superlattice reflections is the manifestation of antiferrodistortive distortions which maintain the rigidity of the connected octahedra. Characteristic peaks of the high symmetry ideal (cubic) perovskite with space group $Pm\bar{3}m$ (No. 221) are singlets but at phase transition boundary, corresponding to a specific substitutional levels and/or temperature value, some of these peaks will split due to lifting of directional cubic symmetry of the unit cell. These reflections with Miller indices (hkl) being odd (O) or even (E) type with respect to parent cell uniquely associated with specific space groups classified by Glazer [182, 183] based on the magnitude and character [in phase (+) /out of phase (-)] of rotations about the three cubic axes.

The monoclinic $P2_1/m$ phase is found in perovskites such as $KMnF_3$ at low temperatures [184]. Being classified as a mixed Glazer tilt system ($a^-b^+c^-$) [171],

this phase assignment to our Sr-rich samples with only OOO-type reflections present seems rather unlikely. In addition, the fact that the main cubic reflections of the (h00) type such as {400} and {200} were found to split into doublet whereas the (hhh)-type peaks (for example {222} reflection at ~ 1.125 Å) remain single is further evidence that the distortion present in our materials cannot be monoclinic. Rietveld refinements were conducted using $P2_1/m$ from which significantly large agreement factors were obtained for all the samples. For example, for $Sr_{0.73}Ca_{0.27}TiO_3$ (SCT27) agreement factors $\chi^2 = 13.01$, $R_{wp} = 6\%$ and $R_I = 19\%$ were obtained compared with the much better $\chi^2 = 4.30$, $R_{wp} = 3\%$ and $R_I = 5\%$ values obtained using the $I4/mcm$ model. This failure to properly fit the data also extends to the low-T regime for all the studied samples. As for the Ca-rich series where the more plausible Pbnm symmetry shares similar tilt characteristics with $P2_1/m$, we also found that the residual agreement factors in $P2_1/m$ pale in comparison with the superior fit corresponding to Pbnm (SCT50 for example: $\chi^2 = 14.02$, $R_{wp} = 6\%$, $R_I = 15\%$ using $P2_1/m$ compared to $\chi^2 = 4.9$, $R_{wp} = 3.5\%$ and $R_I = 6\%$ with $Pbnm$). Moreover, the low symmetry monoclinic distortion is expected to produce many more diffraction peaks that we did not observe.

4.2.2 Orthorhombic space group $P2_12_12$

Significantly worse agreement factors were obtained using the proposed $P2_12_12$ symmetry [148, 167] for the Ca-rich samples. In SCT50 for example,$P2_12_12$ yields $\chi^2 = 23.4$, $R_{wp} = 8\%$ compared with $\chi^2 = 4.90$, $R_{wp} = 4\%$ using $Pbnm$. Additionally, unrealistically large thermal factors were obtained for the oxygen atoms using

$P2_12_12$. For example: O_2 (U_{11}= 0.262(3) Å^2) and O_1 (U_{33}= 0.331(3) Å^2) in $P2_12_12$ compared with 0.0076(2) Å^2 and 0.0030(2) Å^2 in $Pbnm$, respectively.

As for the Sr-rich series, it is interesting to note that the orthorhombic $P2_12_12$ did indeed result in a goodness of fit similar to what we achieved with I4/mcm model. For example, for SCT27 we obtain $\chi^2_{I4/mcm} \approx \chi^2_{P2_12_12} \sim 4.3$ both with $R_{wp} \sim 3\%$. However, in such cases where similar agreements are obtained, it is a universally accepted practice to resort to several tests that can help establishing the correct model. First, $P2_12_12$ is a low noncentrosymmetric space group (No.18) as opposed to a much higher centrosymmetric $I4/mcm$ (No. 140). Accordingly, atoms split in $P2_12_12$ to occupy more independent sites resulting in the number of atomic variables to nearly double compared with $I4/mcm$. Secondly, $P2_12_12$ produces many symmetry-allowed peaks ($\sim$ 1800 reflections) in the d-spacing range of our data resulting in most of the extra reflections having no observed intensities while $I4/mcm$ only produces 296 reflections, see Fig. 4.1 for example. Consequently, a Hamilton ratio test based on these observations clearly confirms that $I4/mcm$ is the correct model when compared with $P2_12_12$.

4.2.3 Orthorhombic space group $Ibmm$

Refinements of the Sr-rich series with the orthorhombic $Ibmm$ [170,173,174,176] resulted in poor peak fitting with large statistical agreement factors. Despite the successful indexing of all the observed reflections due to the similarity in Glazer tilt system (out-of-phase) characterizing the two models [$I4/mcm$ ($a^0a^0c^-$) and $Ibmm$ ($a^-a^-c^0$)], a close inspection of the quality of fit in the inset of Fig. 4.2 reveals unambiguously large differences between the two models. The fitting under-performance

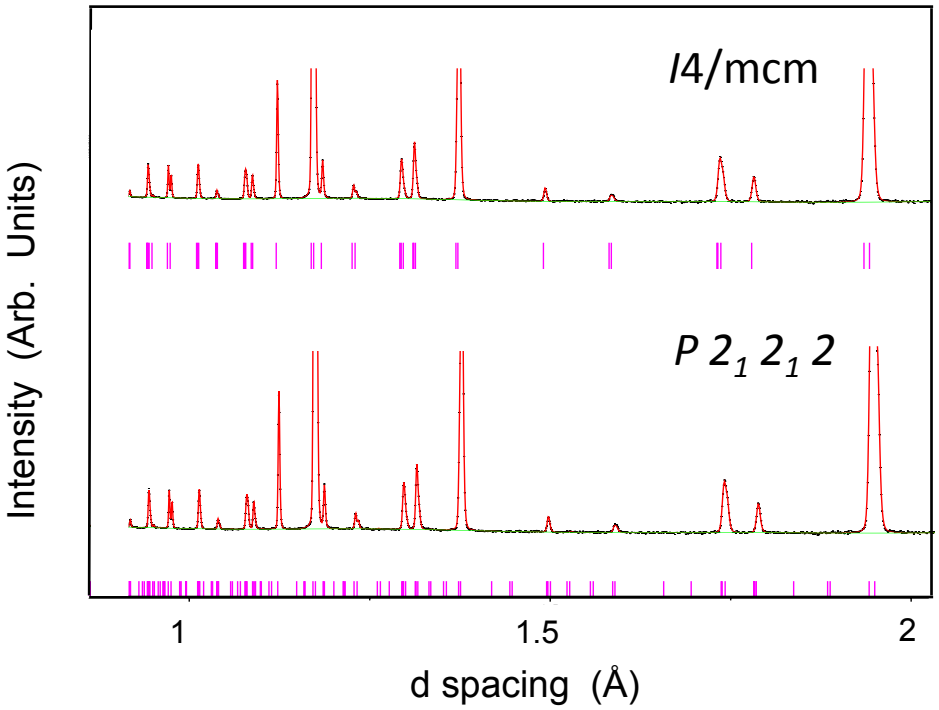

Figure 4.1: Top panel shows diffraction pattern for SCT27 indexed using the $I4/mcm$ space group symmetry. Bottom panel represents indexing the same pattern using the lower symmetry space group $P2_12_12$. The $I4/mcm$ space group indexes nothing other than the observed peaks while $P2_12_12$ results in a large number of unnecessary reflections without any corresponding measured intensities.

using $Ibmm$ is marked by an average value of 5.00% for R_{wp} and a goodness of fit χ^2 value that was found to double for all the samples as shown in Table 4.1. This conclusion holds true for low-T refinements as well where we found that $Ibmm$ was either resulting in large R-factors or unable to index the extra superlattice reflections characterizing the low temperature phase transitions. As we will see below, the Ibmm structural model was found to be suitable only as a mixed phase coexisting with $I4/mcm$ at low temperature in Sr-rich sample with Nd content of 20% where superlattice reflections were absent.

Table 4.1: Room temperature results for the Sr-rich series comparing the statistical agreement factors of $Ibmm$ and $I4/mcm$. Best model that fits our neutron data is $I4/mcm$ structure.

Composition	$I4/mcm$, χ^2 (R_{wp}%)	$Ibmm$, χ^2 (R_{wp}%)
$Sr_{0.73}Ca_{0.27}TiO_3$	4.30 (3.29)	9.77 (5.00)
$Sr_{0.73}Ca_{0.26}Nd_{0.01}TiO_3$	5.15 (4.00)	7.00 (5.00)
$Sr_{0.74}Ca_{0.23}Nd_{0.03}TiO_3$	2.98 (3.00)	6.51 (5.30)
$Sr_{0.76}Ca_{0.16}Nd_{0.08}TiO_3$	2.40 (3.00)	5.11 (5.40)
$Sr_{0.80}Nd_{0.20}TiO_3$	3.60 (3.80)	6.44 (5.20)

As for the Ca-rich series, the characteristics of the tilt type in $Ibmm$ ($a^-a^-c^0$) severely limits its ability to index superlattice peaks that result from a different tilt system (+ in-phase) as shown in Fig. 4.2. This conclusion also extends to the low T regime in all the Ca-rich samples which have shown reflections of the type OOE accounted for by only adopting a mixed-tilt phase such as the $Pbnm$ ($a^-a^-c^+$).

4.2.4 Orthorhombic space group $Bmmb$

The mixed tilt orthorhombic system $Bmmb$ (another setting of $Cmcm$: $a^0b^+c^-$) was also examined. In this model, the unit cell volume ($2a_p$, $2b_p$, $2c_p$) is twice that for $Pbnm$ or $I4/mcm$ ($\sqrt{2}a_p, \sqrt{2}b_p, 2c_p$) and eight times the cubic cell resulting in doubling the number of A-site atoms and a significantly large number of refined parameters. Refinements with this model found to yield large residual agreement factors. For instance, $\chi^2 = 8.10, R_{wp} = 5\%$ using $Bmmb$ for Nd-free Ca-rich sample as opposed to the low values ($\chi^2 = 4.95, R_{wp} = 4\%$) obtained when considering Pbnm instead.

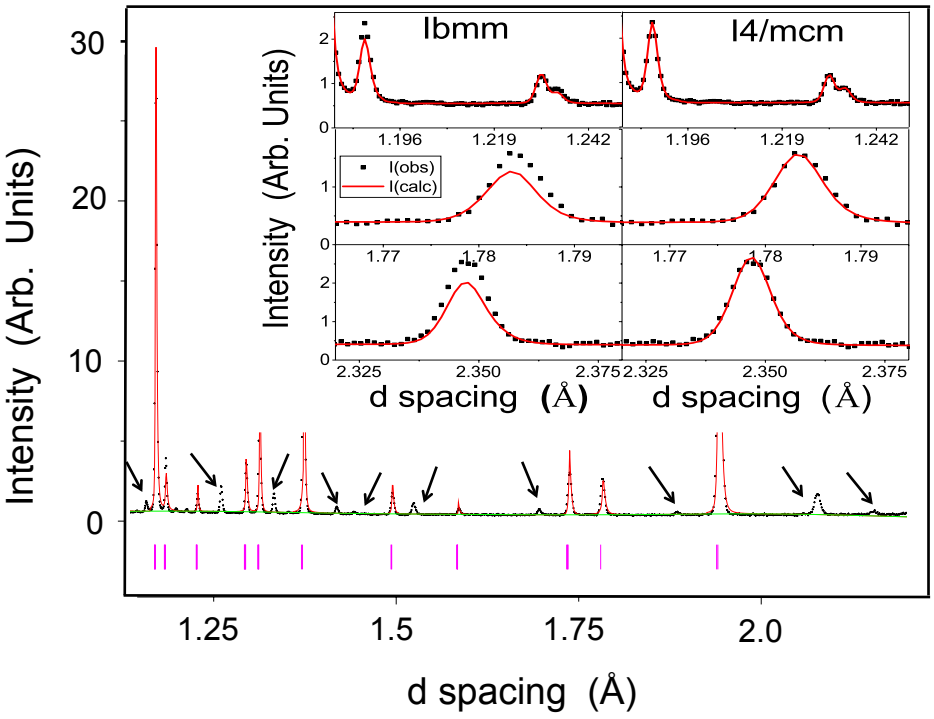

Figure 4.2: Portions of room temperature diffraction data for Ca-rich SCT50 material showing that the high symmetry *Ibmm* space group cannot index all the observed intensities. Inset corresponds to the observed, calculated intensities (solid red line) at 300K for the Sr-rich SCT27 material using $I4/mcm$ and *Ibmm* models.

4.2.5 Structural Analysis of Ca-rich Materials

Rietveld analyses performed on all the members of the Ca rich series show the common orthorhombic *Pbnm* structure (3-tilt system $a^-a^-c^+$ using Glazer notations [182, 183]) at all temperatures between 15 and 300 K and for all the Nd contents y = 0, 0.01, 0.03, 0.08, 0.20. No evidence for any phase transition was detected. As expected for a mixed tilt system, three distinct sets of superlattice reflections relative to the parent cubic structure were observed in the neutron diffraction data. Figure 4.3 shows portions of the patterns at room temperature for SCT50 while the refined structural parameters are listed in Table 4.2.The [612 162] reflections of the

(odd odd even) OOE type (labeling of reflections is with respect to the parent cubic subcell) are due to in-phase tilting, whereas the [533 353 515 155] index set as EEO are due to A-cation displacements in both the x and y directions. Marked peaks have no corresponding reflections in the $I4/mcm$ tilt system. Strong peaks of the EEE type correspond to the elementary unit cell while Peaks of the OOO type are associated with anti-phase tilting. Satisfactory fitting results were achieved when the refinement was carried out using the space group $Pbnm$.

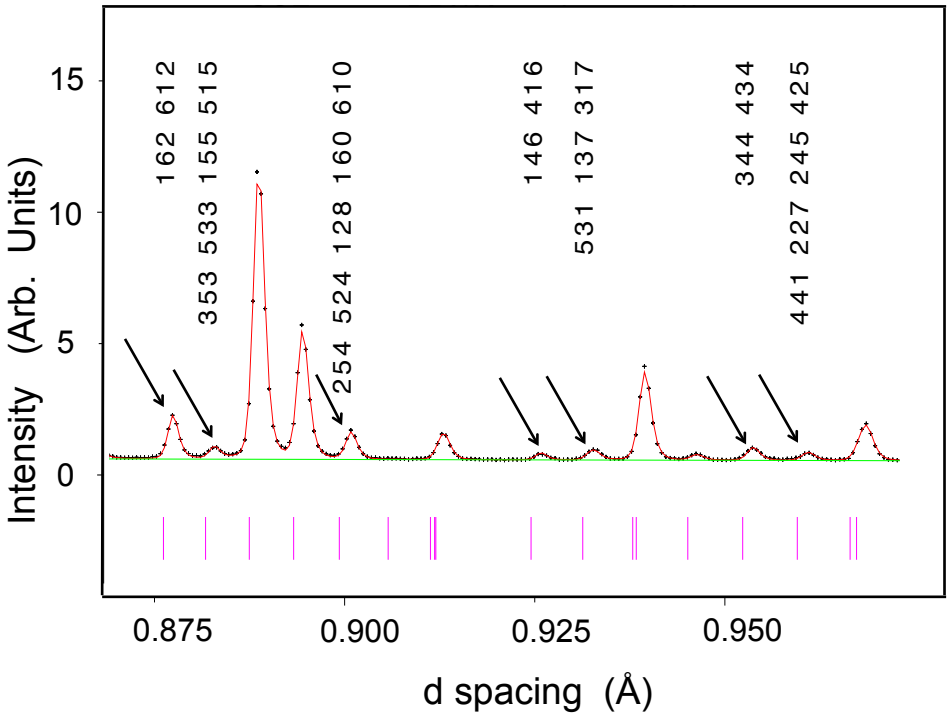

Figure 4.3: Room temperature diffraction data for SCT50 in a narrow d spacing range. Superlattice reflections marked by arrows indicate the orthorhombic $Pbnm$ ($a^-a^-c^+$) symmetry. Tick marks represent symmetry allowed reflections.

Table 4.2: Room temperature structural parameters for orthorhombic $Sr_{0.50}Ca_{0.50}TiO_3$ (SCT50) ($Pbnm$) obtained from neutron diffraction. Lattice parameters a = 5.47640(3) Å, b = 5.47642(3) Å and c = 7.73860(4) Å. Residual agreement factors: $\chi^2 = 4.95$ and $R_{wp} = 3.51\%$.

Atoms	x (Å)	y (Å)	z (Å)
Sr/Ca	0.9982(5)	0.0107(1)	0.25
Ti	0.5	0	0
O(1) Apical	0.0480(1)	0.4949(2)	0.25
O(2) Equatorial	0.7284(1)	0.2729(1)	0.02560(6)

4.2.6 Structural Analysis of Sr-rich Materials

The structural properties of the Sr rich materials are more eventful. Room temperature modeling for the Nd-free $Sr_{0.73}Ca_{0.27}TiO_3$ (SCT27) and $Sr_{0.73}Ca_{0.26}Nd_{0.01}TiO_3$ (Nd01) compositions was successfully performed using a previously proposed tetragonal structure with the $I4/mcm$ space group symmetry [185]. Excellent fits between the observed and calculated intensities were obtained. Table 4.3 lists the refined room temperature structural parameters for SCT27.

Table 4.3: Room temperature structural parameters for tetragonal $Sr_{0.73}Ca_{0.27}TiO_3$ (SCT27) ($I4/mcm$) obtained by Rietveld refinement. Lattice parameters a= 5.4922(1) (Å), c= 7.7981(1) (Å). Residual agreement factors: $\chi^2 = 4.30$ and $R_{wp} = 3.29\%$.

Atoms	x (Å)	y (Å)	z (Å)
Sr/Ca	0	0.5	0.25
Ti	0	0	0
O(1) Apical	0	0	0.25
O(2) Equatorial	0.77390(5)	0.27390(5)	0

Among other space group symmetries that were examined, the proposed orthorhombic *Pbnm* space group was ruled out because it could not produce all the observed reflections. Out-of-phase double tilt orthorhombic *Ibmm* ($a^-a^-c^0$) [166,169,170,176] and rhombohedral ($a^-a^-a^-$) were also tested and rejected. The first gave a relatively large goodness of fit χ^2 value and it could not produce the expected tilts about the *c*-axis. The latter was unable to index many of the observed peaks, especially the main strong reflection at 2.25 Å. Additionally, the initially-singlet peaks of the $(h00)_p$ type associated with the cubic phase should remain unchanged when the transition to the rhombohedral phase takes place whereas peaks of the type $(hhh)_p$ should split, Fig. 4.4 demonstrates a completely different behavior. Using similar arguments as shown earlier, $P2_12_12$ and $P2_1/m$ were ruled out as shown above. Thus, our results confirm that $I4/mcm$ is the appropriate symmetry for our Sr-rich compositions at room temperature.

The $I4/mcm$ phase remains stable as a function of decreasing temperature until a new set of weak superlattice reflections appear below 200 K that cannot be accounted for based on Glazer's 23 tilt systems, see Fig. 4.5 for example. Considering other possible sublattices led to the doubling of the unit cell along the *c*-axis $[001]_p$ direction with the symmetry lowered to orthorhombic *Pbcm* [169, 172].

In the Pbcm space group, the positive Ti ions move off-center in their original octahedral sites to result in displacive distortions thus making this phase ferroelectric. On the verge of the $I4/mcm \rightarrow Pbcm$ phase transition at $\sim$ 200 K, mixed-phase Rietveld refinements for $Sr_{0.73}Ca_{0.27}TiO_3$ successfully converged with phase weight fractions of 60% and 40%, respectively. Evidence for this mixed phase region is displayed in Fig. 4.6 showing the temperature evolution of the tetragonal reflection set $[440/008]_{I4/mcm}$ which is related to the singlet $[400]_{Pm\bar{3}m}$ cubic peak and is often

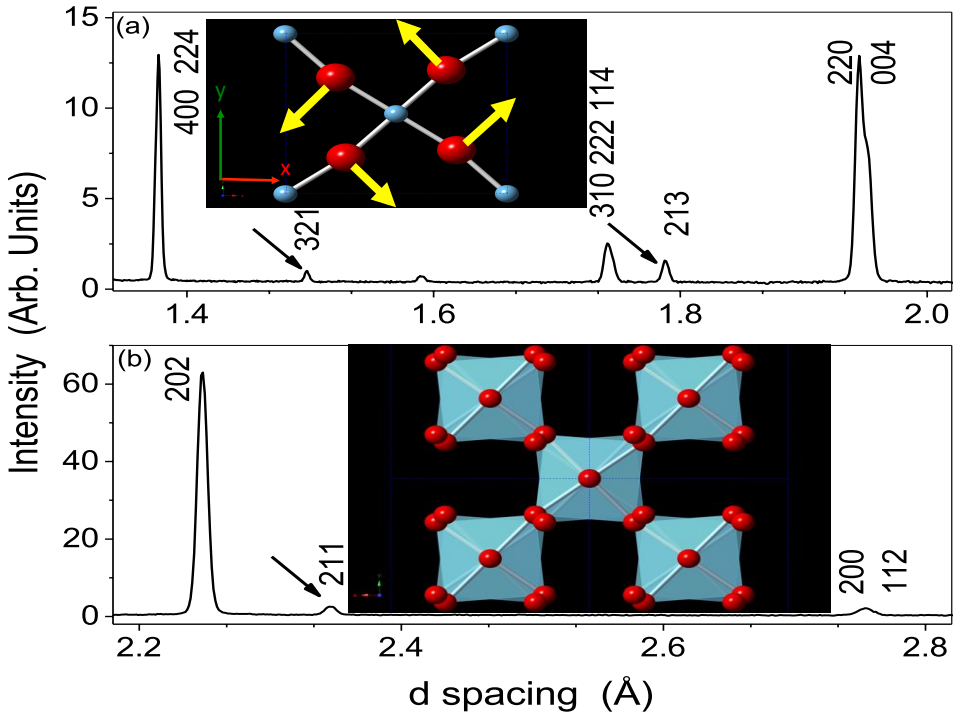

Figure 4.4: Extracts from room temperature neutron diffraction patterns for $Sr_{0.73}Ca_{0.27}TiO_3$. Superlattice reflections of the OOO type with respect to the parent cubic subcell are indicated by arrows in (a) and (b). The tetragonal structure is demonstrated by the splitting of the primitive cubic $(200)_p$ peak into a [220/004] doublet ($I4/mcm$ symmetry). The antiferrodistortive AFD (non polar) mode and directions of oxygen displacements (thick yellow arrows in the inset) within the Ti–O sublattice are shown which reduces the cubic symmetry to tetragonal.

examined to identify similar phase transitions. Between 150 and 200 K, the 440 and 008 peaks greatly overlap as the structure becomes orthorhombic.

The tetragonal $I4/mcm$ stability range for $Sr_{0.74}Ca_{0.23}Nd_{0.03}TiO_3$ is wider (300 – 150 K) in comparison with the two previous Nd-free and Nd 1% samples. A structural transition is also seen in a narrow temperature range close to $\sim$ 125 K but to the common orthorhombic space group $Pbnm$. Unlike the larger orthorhombic $Pbcm$ superstructure, the Ti cations in the $Pbnm$ space-group symmetry remain at the center of the severely distorted oxygen octahedra. As the Nd substitution

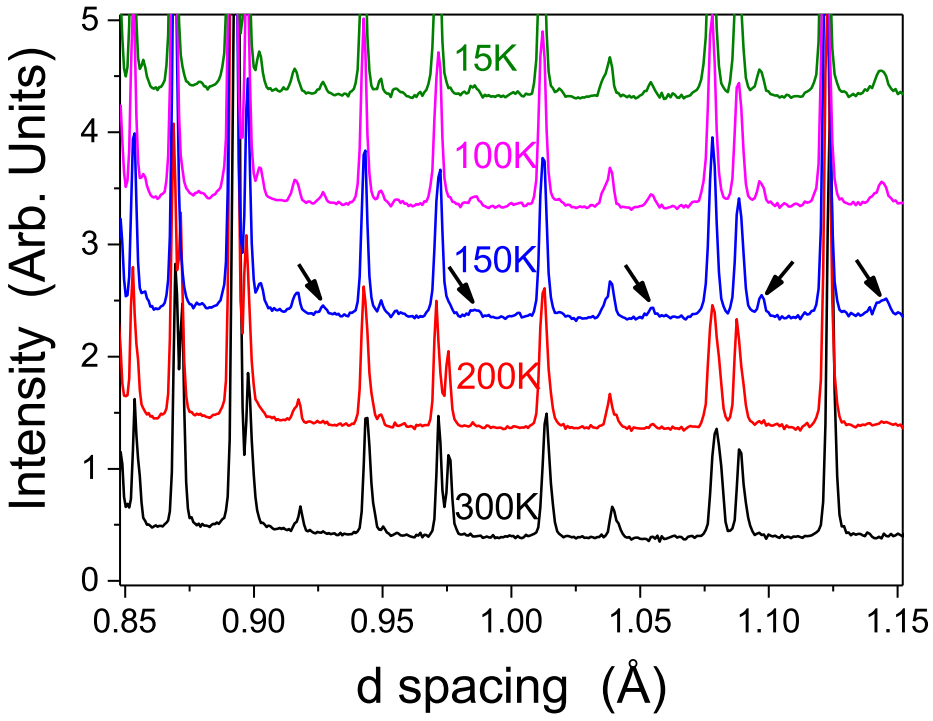

Figure 4.5: Neutron diffraction patterns showing superlattice reflections for $Sr_{0.73}Ca_{0.26}Nd_{0.01}TiO_3$ at select temperatures. Weak peaks arise due to distortions from the 300 K tetragonal structures. Strong peaks appear truncated in the figure to emphasize the weak reflections.

increases to 8% ($Sr_{0.76}Ca_{0.16}Nd_{0.08}TiO_3$), an enhanced stability of the $I4/mcm$ phase is achieved down to the lowest measured temperature of 13 K.

The last sample in the Sr-rich series is the Ca-free heavily doped $Sr_{0.80}Nd_{0.20}TiO_3$ material (Nd 20%). The structure is single phase tetragonal $I4/mcm$ only in a narrow temperature range close to room temperature (300 – 275 K). However, broader peak profiles observed below 275 K are indicative of extra anti-phase tilts about the a or b axes in addition to the existing rotation about the c-axis. The only candidate that satisfies this change is the orthorhombic $Ibmm$ ($a^- a^- c^0$) according to Glazer's tilt models.

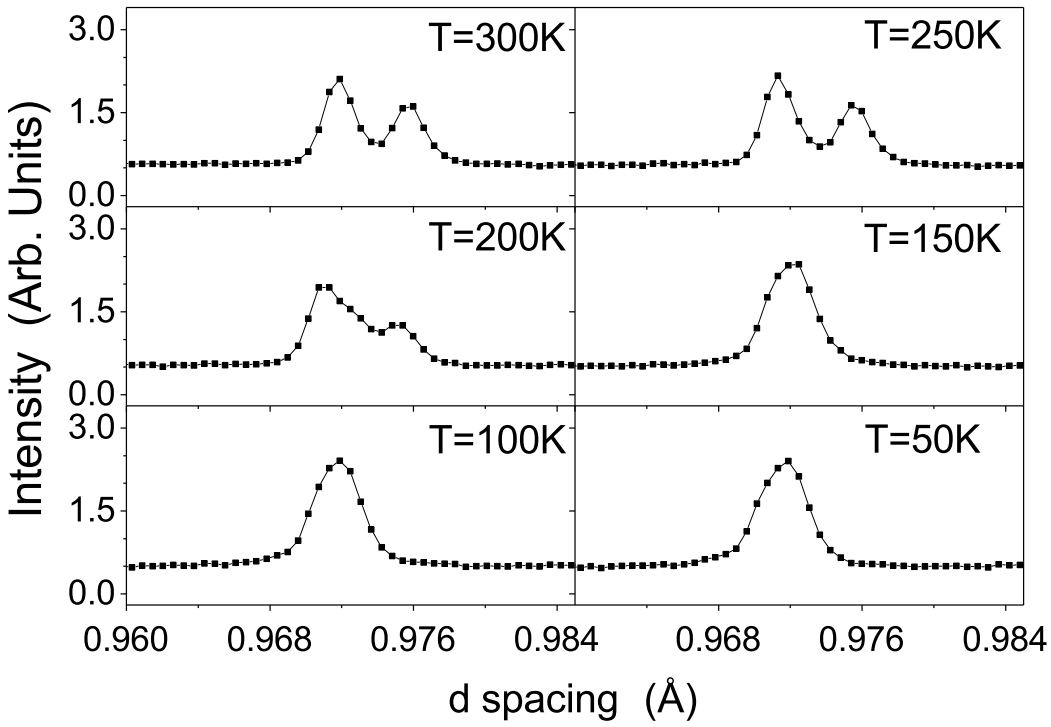

Figure 4.6: Temperature evolution of the tetragonal reflections $(440/008)_{I4/mcm}$ in SCT27 showing evidence of a mixed phase region between 150 and 200K.

Imposing only a single phase symmetry in the $I4/mcm$ or $Ibmm$ space groups in our refinements leads to significant mismatch between the observed and calculated profiles with a deteriorating goodness of fit $\chi^2 = 12.77$ and 11.35, respectively. Therefore, the structure was refined successfully on the basis of a two-phase mixture of $I4/mcm$ and $Ibmm$ which resulted in an excellent fit to the data and drastically lowered χ^2 to 4.35. Both phases coexist in the temperature range 275 – 15 K with $Ibmm$ rapidly becoming the majority phase.

Two of the materials studied here have been intensively investigated in the literature, namely $Sr_{0.73}Ca_{0.27}TiO_3$ and $Sr_{0.50}Ca_{0.50}TiO_3$ for which our structural transitions sequence are in agreement [27,160,168,169]. On the other hand, claims [160]

of a room temperature cubic structure for $Sr_{0.80}Nd_{0.20}TiO_3$ are not sustained in this study.

4.3 Compositional (y)/Thermal Effects on the Lattice Parameters of $Sr_{(1-x-y)}Ca_{(x)}Nd_{(y)}TiO_3$

The lattice constants of our samples expand with increasing Nd^{3+} doping levels mainly due to the increased ionic ratio of Ti^{3+}/Ti^{4+}. The c-parameter of the $I4/mcm$ phase appears to be expanding linearly in the measured temperature range. The $I4/mcm \rightarrow Pbnm$ and $I4/mcm \rightarrow Pbcm$ first-order structural transitions in some of our Sr-rich materials is manifest by the abrupt jumps in the c- (downwards) and b- lattice parameters (upwards) shown in Fig. 4.7(a,c).

The comparable average [Ti–O] bond length in the lightly doped samples (Nd: 0–8 %) in both series as seen in Fig. 4.7(g and h) is markedly smaller than the values in the heavily doped counterparts (Nd: 20%). This difference in bond length between the two groups has a profound impact on the transport properties and results in two distinct conduction mechanisms of the charge carriers, as we will see later in this chapter.

In an earlier work, Ubic [186] proposed an empirical formula $a_{calc} = 0.06741 + 0.49052\ (r_A + r_O) + 1.29212\ (r_B + r_O)$ as a function of Shannon's tabulated ionic radii [24] for the prediction of pseudocubic lattice constants of the diverse known perovskites ($a_p \approx b_p \approx c_p$). When compared with the lattice parameters measured for a large number of perovskite materials, the results of this formula were found to yield highly reliable values with an average relative error of no more than 0.60%. For our samples, we find that the best fit between the calculated (applying Ubic's

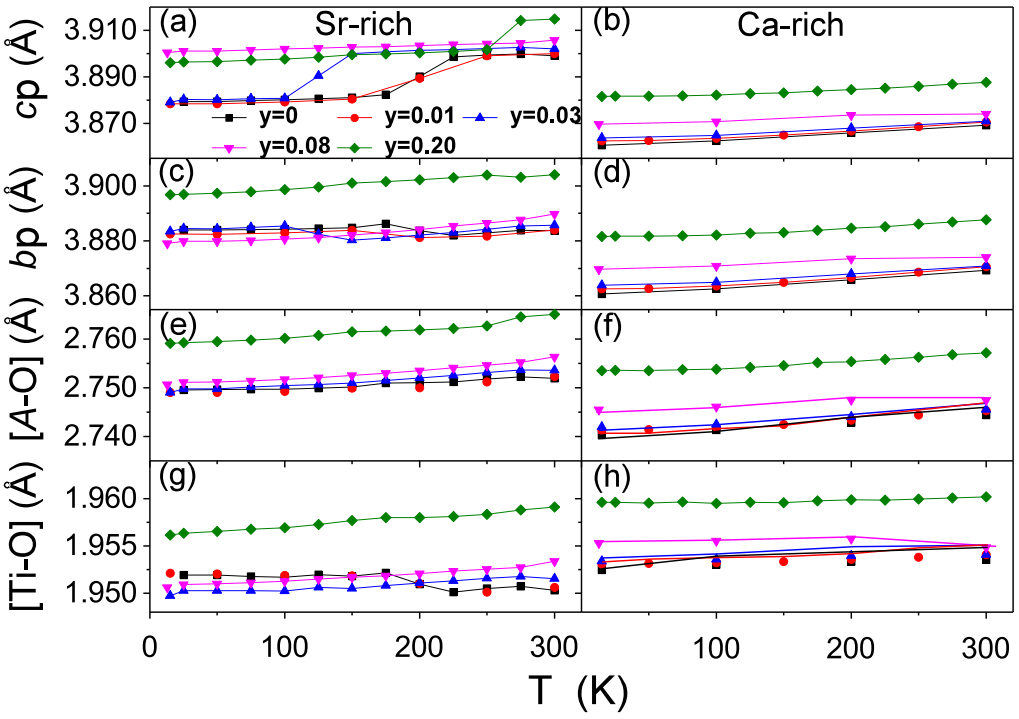

Figure 4.7: Plots of reduced c_p (= c/2) and b_p (= $b/\sqrt{2}$) lattice constants and the bond lengths [A–O] and [Ti–O] as a function of temperature. Curiously, the opposite behaviors of these parameters perfectly compensate to produce a continuous expansion of the unit cell volume upon increasing the temperature, see Fig 4.8.

formula) and measured room temperature lattice parameters is achieved when considering 8-fold coordinated A-cations in both the Sr- and Ca-rich series with relative errors of 0.84% and 0.80%, respectively (assuming 12-fold coordination would raise the error to 1.5% or more).

The apparent inadequacy of Shannon's ionic radii to help predicting the pseudocubic lattice constants using 12-fold coordinated A-site ionic sizes may be due to a host of different reasons including insufficient accuracy or simply to the fact that four of the twelve ligands in the distorted structures are usually long enough that they do not effectively contribute to ionic bonding. This is a well-known problem that has been repeatedly observed and invoked when explaining for example the

magnetic properties of the colossal magnetoresistive perovskite manganites in terms of their internal structural parameters [177].

The effects of both the Nd content and temperature on the unit cell volume for all the investigated materials are depicted in Fig. 4.8. The unit cell volume of the parent $SrTiO_3$ [168, 187–189] and $CaTiO_3$ [27, 179, 190] materials are shown for comparison.

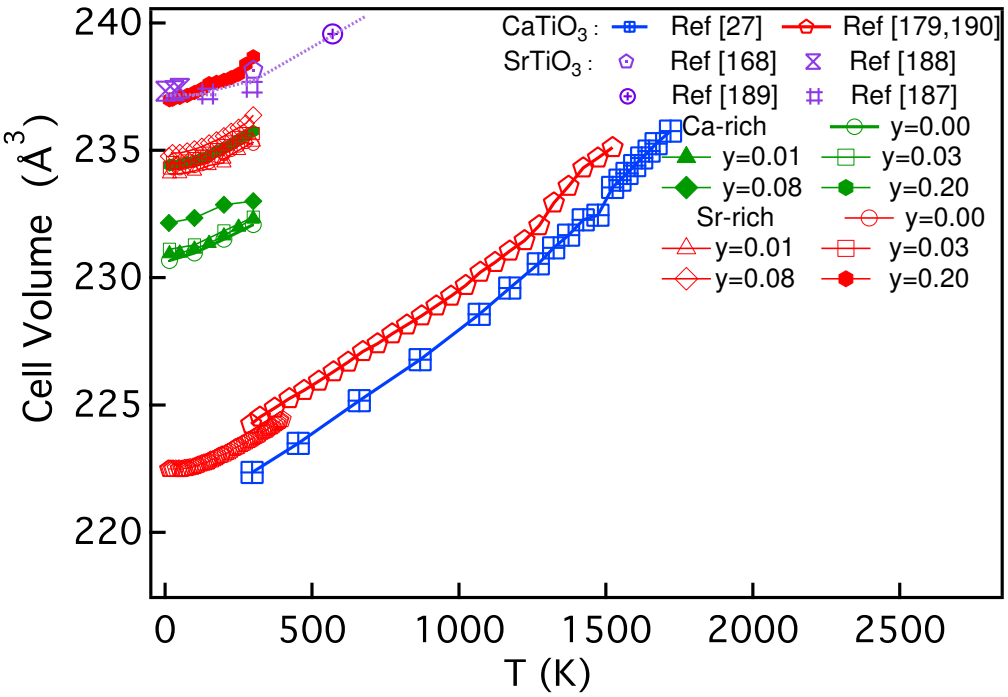

Figure 4.8: Unit cell volume behavior as a function of temperature for all of our Sr-rich and Ca-rich samples together with those of the parent $CaTiO_3$ and $SrTiO_3$ materials as extracted from multiple literature references. The inset shows the zoomed in data for both series.

4.4 Bond Lengths and Angles

In this section, we will examine the octahedral tilts and bond-length trends with doping and thermal variations. Adjusting to the structural deformation in the form of A-O and B-O bond length mismatch ($t < 1$), the TiO_6 octahedra rotate cooperatively ($Pbnm$ and $I4/mcm$ structure) [35] about the c-axis to distort the equatorial Ti–O2–Ti bond angle from its ideal value of 180° in the cubic symmetry, and tilt relative to the (001) plane making the apical Ti–O1–Ti bond-angle less than 180° ($Pbnm$) [191]. Therefore, the average distortion of the <Ti–O–Ti> bond angle provides a direct measure of the overall structural deformation through its proportionality to the tolerance factor, $t \sim \cos^2(< Ti\text{-}O\text{-}Ti >)$ [177]. The octahedral tilt angle has been clearly identified as the order parameter for non-polar phase transitions in perovskites [192, 193].

The magnitude of the tolerance factor t, which acts as the driving mechanism for the octahedral tilts, is kept nearly the same as that of the Nd-free sample of each series. Therefore, the <Ti–O–Ti> bond-angle is expected to reflect this doping-independency. Indeed, insignificant differences were observed between the Nd-free $Sr_{0.73}Ca_{0.27}TiO_3$ (174.54°) and the heavily doped $Sr_{0.80}Nd_{0.20}TiO_3$ (174.83°) samples of the Sr-rich series. Likewise, in the Ca-rich series the <Ti–O–Ti> bond angle ranges between 164.49° for Nd-free SCT50 and 165.96° for $Sr_{0.57}Ca_{0.23}Nd_{0.20}TiO_3$, see inset of top panel in Fig. 4.9.

The effects of temperature on the <Ti–O–Ti> bond angle are more significant with first order phase transitions observed in the Sr-rich series. For example, a 5-6° change is determined for the y = 0, 1, and 3 % samples between 300 and 15 K while the single-phase Nd 8% sample has its <Ti–O–Ti> bond angle contracting by

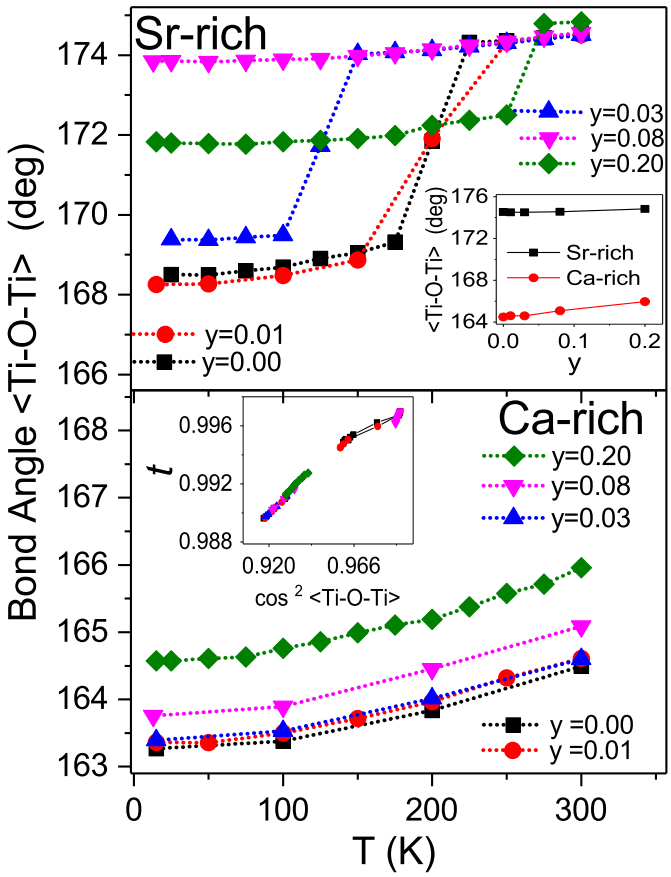

Figure 4.9: T-variations of the average <Ti–O–Ti> bond angle for Sr-rich materials. The abrupt drops correlate with first-order phase transitions to lower symmetries. The inset shows the linear relationship between tolerance factor (t) and the squared cosine of the bond angle.

only $\sim 0.7^{\circ}$ over a similar temperature range. On the other hand, the temperature-dependence of the <Ti–O–Ti> bond angle is weaker and more uniform in the Ca-rich series in which phase transitions are absent with changes of only $\sim 1.3^{\circ}$ observed for all the members of this series as displayed in the bottom panel of Fig. 4.9. Based on these results, we conclude that larger effects of the bond angle should be expected on the physical properties of the Sr-rich compounds in agreement with their thermoelectric properties presented later.

Correct understanding of the correlation between structural and physical properties requires defining the NPD-measured bond length <A–O> as the geometrical average of all 12 individual distances A–O. Twelve A–O bond lengths of the A-site polyhedron exhibit a room temperature length distribution ranging from 2.62389(4) to 2.89176(2) Å and from 2.4862(32) to 3.0346(22) Å for the tetragonal Sr-rich and the more distorted orthorhombic Ca-rich series, respectively. Geometric averaging of the bonds reveals that the A–O bond-length average expands slightly as a function of increased Nd content (Table 4.4) or temperature [Fig. 4.7(e) and (f)] with nearly identical thermal expansion rates of 0.49% or 0.52% for the Sr-rich and Ca-rich series, respectively.

On the other hand, the geometrically averaged <Ti–O> bond lengths also elongate in both series upon increased substitution of the trivalent Nd^{3+} ions at the bivalent Sr^{2+}/Ca^{2+} sites. The lengthening of the bonds can be easily explained by the expected partial conversion, via Nd doping, of some Ti^{4+} ions into Ti^{3+} and the consequent formation of larger [Ti^{3+}– O] bonds. The <Ti–O> bond length in the $I4/mcm$ Sr-rich samples increases by 0.45% from 1.95028(9) Å (for Nd-free sample) while the $Pbnm$ members of the Ca-rich series exhibit a somewhat weaker response with the <Ti–O> bond length increasing by only 0.33% from its initial value of 1.9535(39) Å in the Nd-free $Sr_{0.50}Ca_{0.50}TiO_3$. It is worth noting that the structural sensitivity of the TiO_6 octahedra, quantified by the percent change in [Ti–O] bond length upon doping, appears to depend on the initial degree of structural distortions of the Nd-free parent compound. This observation should be taken into consideration when designing newer materials with specific desired tolerance factors.

Thanks to the unique choice of our carefully selected A-site cationic compositions, similar room temperature expansion rates are obtained as a function of Nd doping for the averaged <A–O> and $\sqrt{2}$<Ti–O> bonds and hence the tolerance

Table 4.4: Room temperature bond lengths and oxygen site occupancies of $Sr_{1-x-y}Ca_xNd_yTiO_3$ obtained from NPD refinement results.

Sr-rich series (I4/*mcm*)						Ca-rich series (P*bnm*)					
	Nd0	Nd01	Nd03	Nd08	Nd20		Nd0	Nd01	Nd03	Nd08	Nd20
A–O1 ×4	2.74614(6)	2.74634(7)	2.74756(6)	2.75044(6)	2.76059(2)	A–O1 ×1	2.4862(32)	2.489(4)	2.492(4)	2.4969(31)	2.5085(27)
A–O2 ×4	2.62389(4)	2.62372(34)	2.62488(29)	2.62868(32)	2.64267(2)	A–O1 ×1	2.6659(21)	2.6674(31)	2.6688(28)	2.6762(26)	2.7068(30)
A–O2 ×4	2.88561(5)	2.8867(4)	2.88820(32)	2.8898(4)	2.89176(2)	A–O1 ×1	2.8376(20)	2.8366(30)	2.8369(27)	2.8296(26)	2.8187(30)
						A–O1 ×1	2.9929(32)	2.992(4)	2.990(4)	2.9905(31)	3.0025(27)
						A–O2 ×2	2.5003(18	2.5021(24)	2.5020(20)	2.5118(18)	2.5464(17)
						A–O2 ×2	2.6946(18)	2.6964(24)	2.6942(20)	2.6942(18)	2.6920(18)
						A–O2 ×2	2.7463(16)	2.7458(22)	2.7479(17)	2.7585(16)	2.7875(15)
						A–O2 ×2	3.0336(16)	3.0346(22)	3.0346(18)	3.0233(16	2.9987(16)
						Mean (short 8)	2.6293(3)	2.6306(96)	2.6311(9)	2.6377(8)	2.6584(1)
						Mean (long 4)	2.9744(46)	2.9745(7)	2.9741(4)	2.9666(97)	2.9546(7)
[A–O1]	2.74614	2.74634	2.74756	2.75044	2.76059	[A–O1]	1.9526(3)	1.9526(43)	1.9532(1)	1.95328(2)	1.9596(7)
[A–O2]	2.75475	2.75521	2.75654	2.75924	2.767215	[A–O2]	1.954	1.9547(7)	1.9545(2)	1.9556(2)	1.9604(4)
Mean (12) [A–O]	2.74980(55)	2.75015(9)	2.75144(79)	2.75424(5)	2.76313(67)	Mean (12) [A–O]	2.7378(14)	2.7388181	2.7390(4)	2.7413(46)	2.7519(78)
B–O1 ×2	1.94953(4)	1.94999(5)	1.95100(4)	1.95288(4)	1.95739(2)	B–O1 ×2	1.95263(14)	1.95264(30)	1.95320(26)	1.95328(22)	1.95967(11)
B–O2 ×4	1.95067(4)	1.95090(7)	1.95178(6)	1.95366(6)	1.96000(1)	B–O2 ×2	1.9487(10)	1.9506(20)	1.9514(18)	1.9478(15)	1.9512(9)
						B–O2 ×2	1.9592(9)	1.9589(19)	1.9576(18)	1.9634(15)	1.9695(9)
Mean(6) [B–O]	1.95028(99)	1.95059(7)	1.95151(9)	1.95339(99)	1.95912(96)	Mean(6) [B–O]	1.9535(39)	1.9540(58)	1.9540(8)	1.9548(27)	1.9601(69)
Oxygen 1 occupancy	1.004(7)	0.998(7)	0.996(7)	0.9993	0.985(5)		0.999(2)	0.997(2)	1.057(3)	1.052(2)	1.002(3)
Oxygen 2 occupancy	1.005(8)	1.007(7)	1.003(5)	1.0133	1.011(5)		1.004(1)	1.008(4)	1.057(3)	1.008(1)	1.002(3)

Table 4.5: Room temperature bond lengths extracted from our NPD refinements compared to literature values for materials of interest to this study.

Bond Type	Material	Bond Length (Å)	Structural Symmetry	Reference	T (K)
$[^{XII}Ca^{2+}-O]$	$Sr_{0.73}Ca_{0.27}$ and $Sr_{0.50}Ca_{0.50}$	2.7117(45)	I4/mcm and Pbnm	This Study	300
	$CaTiO_3$	2.7022(76)	Pbnm	Ref [27], NPD	296
	$Ca_{1-x}Sr_xTiO_3$ solid solution (x=0)	2.706(8)	Pbnm	Ref[180], X-ray	300
$[^{XII}Sr^{2+}-O]$	$Sr_{0.73}Ca_{0.27}$ and $Sr_{0.50}Ca_{0.50}$	2.76388(3)	I4/mcm	This Study	300
	$Ca_{1-x}Sr_xTiO_3$ solid solution (x=1)	2.760(1)	Pm -3 m	Ref[180], X-ray	300
$[^{XII}Nd^{3+}-O]$	Nd-doped Sr-rich series (Mean)	2.75100(9)	I4/mcm	This Study	300
	Nd-doped Ca-rich series (Mean)	2.7618(32)	Pbnm	This Study	300
	$NdTiO_3$	2.7943(3)	Pbnm	Ref[191], X-ray & NPD	290
$[^{VI}Ti^{4+}-O]$	$Sr_{0.73}Ca_{0.27}$	1.95028(9)	I4/mcm	This Study	300
	$Sr_{0.50}Ca_{0.50}$	1.9535(39)	Pbnm	This Study	300
	$CaTiO_3$	1.95083(9)	Pbnm	Ref [177], NPD	296
	$CaTiO_3$	1.956	Pbnm	Ref[160], X-ray	298
	$CaTiO_3$	1.952(6)	Pbnm	Ref[180], X-ray	300
	$SrTiO_3$	1.952(1)	cubic	Ref[180], X-ray	300
	$SrTiO_3$	1.954	cubic	Ref[160], X-ray	298
$[^{VI}Ti^{3+}-O]$	Nd-doped Sr-rich series (Mean)	1.98896(9)	I4/mcm	This Study	300
	Nd-doped Ca-rich series (Mean)	1.9821(1)	Pbnm	This Study	300
	$LaTiO_3$	2.040(3)	Pbnm	Ref[191],, X-ray & NPD	290
	$LaTiO_3$	2.0392(28)	Pbnm	Ref[194],NPD	293
	$LaTiO_3$	2.0346(5)	Pbnm	Ref[195], NPD	298
	$NdTiO_3$	2.0426(3)	Pbnm	Ref[191],, X-ray & NPD	290

factor remains constant as intended for each series. Finally, the combination of multiple compositions with various degrees of Sr, Ca and Nd contents at the disordered A-site and the high-resolution NPD data allow us to disentangle the average A-site to oxygen distances and to determine the individual Sr-O, Ca-O, Nd-O, Ti^{3+}-O and Ti^{4+}-O bond lengths. Values are summarized in Table 4.5 together with related values extracted from the literature [27, 160, 180, 191, 194, 195].

4.5 Effects of Nd Substitution/Temperature on the Tolerance Factor

The essentially constant room temperature tolerance factors upon increased Nd doping range between 0.9969(8) [Nd-free sample] and 0.9979(7) [Nd 20%], and

0.9909(9) [Nd-free] and 0.9927(4) for the Sr-rich and the orthorhombic Ca-rich series, respectively. Phase transition temperatures T_S both measured (from our NPD structural refinement results in the temperature range 13-300K) and calculated by extrapolating and fitting the t factor above room temperature to a power law in T in the form $t(T) = t_{0(T=0)} + AT^n$, with $n = 2$ assuming an intermediate tetragonal phase transition ($I4/mcm$) for the orthorhombic Ca-rich samples ($0.994 \leq t < 1$) as shown in Figs. 4.10 and 4.11 are summarized in Table 4.6 and compared to the values acquired from synchrotron x-ray data and to the available literature data [27, 168, 188, 196]. The values of the fitted parameter A is in the range 1.53–1.55 $\times 10^{-8} K^{-2}$ for Nd-doped materials and $\sim 1 \times 10^{-8} K^{-2}$ for Nd-free system.

In Fig. 4.10, literature data are used for the parent $SrTiO_3$ [188] and $CaTiO_3$ [27, 168].For $SrTiO_3$, low temperature data [188] in the 1.5 to 50 K range were extrapolated to $t = 1$ using the same power law employed with the other materials from which we obtained a transition temperature, T_S, to the cubic symmetry at $\sim$ 110 K in excellent agreement with the literature [196].

The tolerance factor is determined by various factors. Nonetheless, the capability of this structural parameter to predict the high temperature tetragonal to cubic transitions (regardless of actual symmetries) has been demonstrated in several other systems [159]. The actual transition temperatures, T_S, from $I4/mcm$ to $Pm\bar{3}m$ are very well known for the $Ca_{1-x}Sr_xTiO_3$ system with Ti^{4+} and can be found in Refs. [27, 166, 179, 196]. In addition to the results of our own two samples of Nd-free $Ca_{1-x}Sr_xTiO_3$, other published room temperature neutron diffraction studies provided very similar values of the Sr-O, Ca-O and Ti^{4+}-O bonds from which very precise room temperature tolerance factor t(300 K) can be derived for any value of x [27, 170, 172, 174, 176, 180, 197]. Moreover, several neutron diffraction studies

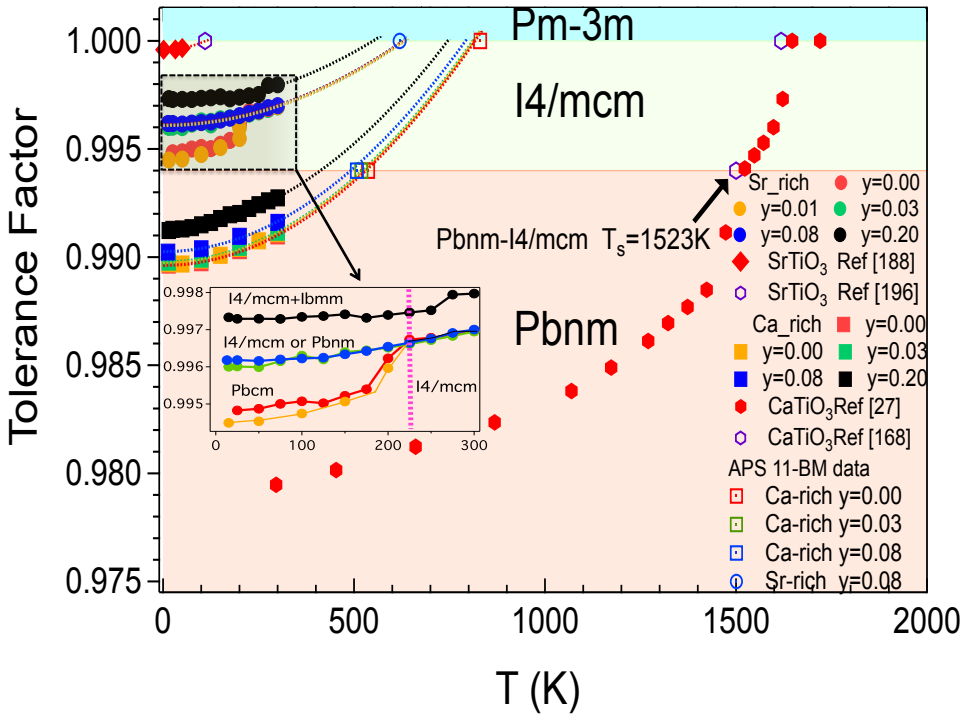

Figure 4.10: Tolerance factor versus temperature for the full $Sr_{(1-x-y)}Ca_{(x)}Nd_{(y)}TiO_3$ system.Solid lines correspond to the fitting of the NPD data (10-300K) to elevated temperatures. Open symbols shown on the critical cubic and tetragonal transition lines are data obtained experimentally from the APS 11BMB x-ray beamline for comparison.Inset shows the thermal variation of tolerance factor for the Sr-rich series where various low-T crystal structures were observed.

have been reported as a function of temperature for $Ca_{1-x}Sr_xTiO_3$ from which we derived the temperature dependence of tolerance factor $t(x,T)$ for selected compositions x, as well as an average tolerance factor equation $t(T) \sim AT^2$. Table 4.7 shows a remarkable agreement between the actually measured T_S values and the T_S estimated from the condition of transition to the cubic structure when the tolerance factor reaches the value of 1 for specific compositions x, $t(x, T = T_S) = 1$ of the $Ca_{1-x}Sr_xTiO_3$ series (see Figure 4.12). We have used the same procedure to estimate the transition from $I4/mcm$ to $Pm\bar{3}m$ for the charge substituted system $(Sr,Ca)_{1-x}Nd_xTiO_3$ with $Ti^{(4-x)+}$ and elongated Ti – O bond lengths but with

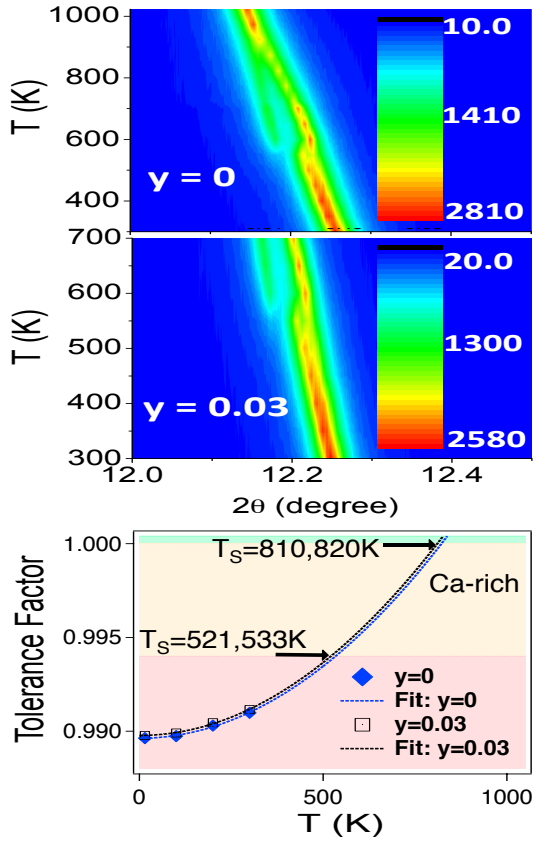

Figure 4.11: Representative x-ray contour maps collected at the APS showing the structural transition temperatures for the Ca-rich samples with Nd content y of 0 and 3 %. The bottom panel displays the orthorhombic to tetragonal and tetragonal to cubic phase transition temperatures for the same samples extracted by fitting the tolerance factor curves as a function of temperature t (T) to a power law of the form $t(T) = t_{0(T=0K)} + AT^n$ with $n = 2$.

an almost room temperature fixed tolerance factor. In summary, this method of estimation of the cubic $t(x,T) \geq 1$ to non-cubic $t(x,T) < 1$ structural transition with decreasing temperature is highly reliable because it does not depend on phases/symmetries below T_S and the T^2 dependence of the tolerance factor on temperature is well known and has been observed for many other perovskite systems [177].

Table 4.6: Transition temperatures T_S (Orthorhombic to Tetragonal to Cubic) for the $Sr_{(1-x-y)}Ca_{(x)}Nd_{(y)}TiO_3$ system with the Nd content y= 0, 0.01, 0.03, 0.08, and 0.20. The superscript c refers to extrapolated estimates from the tolerance factor curves to higher temperatures. The superscript (xr) refers to the APS 11BMB data represented by open circles and squares in Fig. 4.10 while NPD T_S values are obtained from our refinement using measured NPD data. Superscripted numbers represent literature references.

Sample	T_S(K) Ortho (Pbcm, Pbnm, Ibmm) $\rightarrow I4/mcm$	T_S(K) $I4/mcm \rightarrow Pm\bar{3}m$
$CaTiO_3$	1523 [27], 1500 [168]	1647 [27], 1618 [168]
$SrTiO_3$		110 [196]
$Sr_{0.50}Ca_{0.50}TiO_3$	575 [168], 536.5 ^{xr}, 533 ^{c}	923 [168], 830^{xr}, 820^{c}
$Sr_{0.50}Ca_{0.49}Nd_{0.01}TiO_3$	524^{c}	813^{c}
$Sr_{0.51}Ca_{0.46}Nd_{0.03}TiO_3$	519^{xr}, 521^{c}	810^{c}
$Sr_{0.53}Ca_{0.39}Nd_{0.08}TiO_3$	507.44^{xr}, 493^{c}	792^{c}
$Sr_{0.57}Ca_{0.23}Nd_{0.20}TiO_3$	410^{c}	746^{c}
$Sr_{0.73}Ca_{0.27}TiO_3$	200^{NPD}	643.1 [168], 630^{c}
$Sr_{0.73}Ca_{0.26}Nd_{0.01}TiO_3$	200^{NPD}	632^{c}
$Sr_{0.74}Ca_{0.23}Nd_{0.03}TiO_3$	125^{NPD}	631.8^{c}
$Sr_{0.76}Ca_{0.16}Nd_{0.08}TiO_3$	-	619.2^{xr} 628^{c}
$Sr_{0.80}Nd_{0.20}TiO_3$†	250^{NPD}	550^{c}

†A mixed-phase sample with T_S =250K corresponding to the boundary between $(I4/mcm + Ibmm)$ and $I4/mcm$.

4.6 Enhanced Thermoelectric Properties by Charge Doping and Point Defect Scattering

4.6.1 Lattice Thermal Conductivity

Low thermal conductivity is required for the successful development of materials suitable for *TE* applications. For example, thermoelectric effectiveness has been

Table 4.7: Transition temperatures $T_S^{\bullet}$ values (tetragonal to cubic) calculated from extrapolation of the measured structural tolerance factor near room temperature: $t(T) \sim aT^2$ for the $Ca_{1-x}Sr_xTiO_3$ perovskite system (where x is the Sr content) as compared to the measured $T_S^{\dagger}$ values from various references.

x in $Ca_{1-x}Sr_xTiO_3$	0 ($CaTiO_3$)	Refs	0.25	Refs	0.50	Refs	0.57	Refs	0.70	Refs
$T_S^{\dagger}$ (K)	1634±13	[27]	1260	[166]	923	[168]	810	[166]	618	[166]
	1618	[168]								
$I4/mcm \rightarrow Pm\bar{3}m$	1580	[175]			911	[166]				
	1630	[166]								
$T_S^{\bullet}$(K)	1580		1270		930		840		600	
x in $Ca_{1-x}Sr_xTiO_3$	0.73	Refs.	0.75	Refs.	0.88	Refs.	x=1 ($SrTiO_3$)	Refs.		
$T_S^{\dagger}$(K)	643	[168]	546	[166]	400	[166]	110	[?]		
$I4/mcm \rightarrow Pm3m$	584	[166]					105	[166]		
$T_S^{\bullet}$(K)	580		560		395					

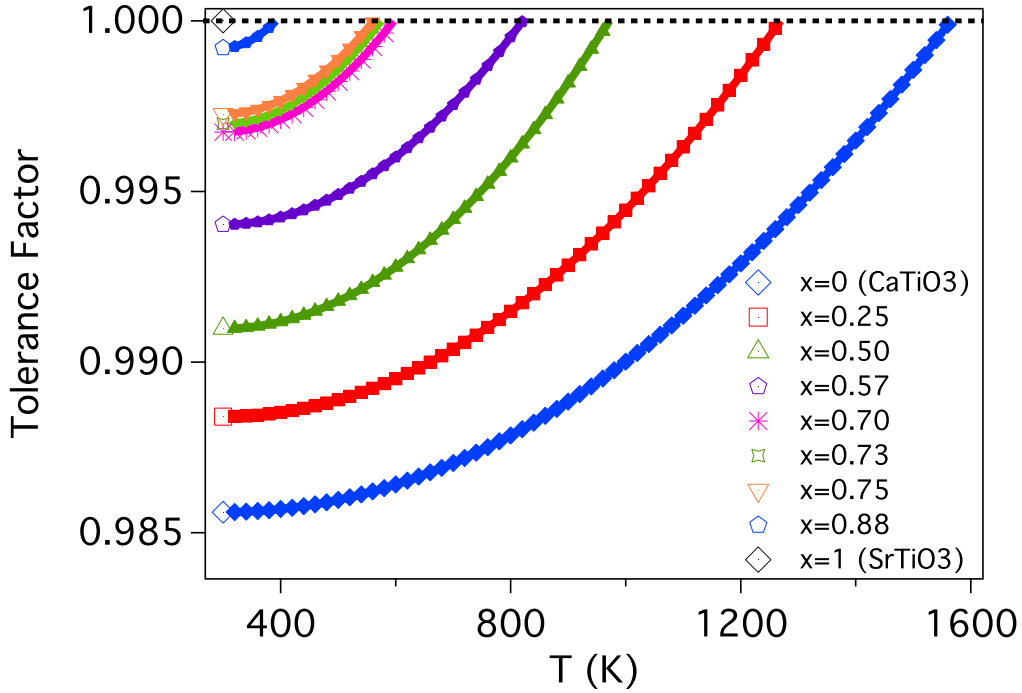

Figure 4.12: Measured room temperature tolerance factor values from Refs. [170, 172, 174, 176, 180, 197] extrapolated as a function of temperature for selected x compositions across the solid solution perovskites $Ca_{1-x}Sr_xTiO_3$.

repeatedly confirmed to be limited by the phonons thermal conductivity in n-type $SrTiO_3$ oxides [34, 38, 76].

Seebeck coefficient is an intrinsic thermoelectric parameter that is essentially dependent only on the concentration and degeneracy/entropy of the charge carries [67] whereas the bulk electrical conductivity is likely to include extrinsic effects that depend on the material's growth conditions. Therefore, reducing the lattice thermal conductivity κ_L has become one of the most popular strategies to improve the *TE* performance of materials [83]. To that end, various novel methods have been implemented to curb the phonon conduction. In conventional *TE* semiconductors, alloying [198] is at the center of methods designed for reducing thermal conductivity and has become the main factor behind their fascinating *TE* capabilities with

ZT values exceeding 1 in most cases. Also proven successful is the introduction of heavy rare earth atoms into materials with large lattice voids whose free rattling atom serves as additional phonon point defect scattering centers [199] for the acoustic (long wavelength) phonons that are involved in heat conduction such as in the cage-filled skutterudite structures $Ce(Fe,Co)_4Sb_{12}$ [200, 201] in which thermal conductivity is lowered significantly as compared to unfilled compounds $CoSb_3$.

Materials such as clathrates [202] with a large number of atoms or those with complex structures typically scatter phonons more effectively [76].

Attempts at reducing κ_L in the simpler bulk $SrTiO_3$-based materials usually involve the deliberate lattice distortion from the cubic structure by rare-earth substitution which reduces the phonon mean free path as in Dy- and Y-doped $SrTiO_3$ [203]. Heavy rare-earth dopants are also considered effective phonon scattering centers [80].

Measurements of the thermal conductivity κ of our materials are presented in Fig. 4.13 (a,b). The figure demonstrates a significant reduction in with room temperature values are as low as $\sim$ 1.5 W/K.m approaching the limit reported in amorphous silicon [204]; significantly smaller than $\sim$ 12 W/K.m for both the parent $SrTiO_3$ [34, 205] and Nb-doped $SrTiO_3$ [38, 76] materials. Such a large order-of-magnitude suppression of κ whose electronic contribution is a function of the charge carrier concentration (electrons) can be mainly attributed to effective phonon scattering as will be discussed below.

$SrTiO_3$-based oxides are strongly correlated materials with pronounced lattice vibrations that arise from the presence of light oxygen [206] making the electronic contribution practically negligible. To confirm this assertion, the electronic κ_e and phonons κ_L contributions to the total thermal conductivity are separately evaluated.

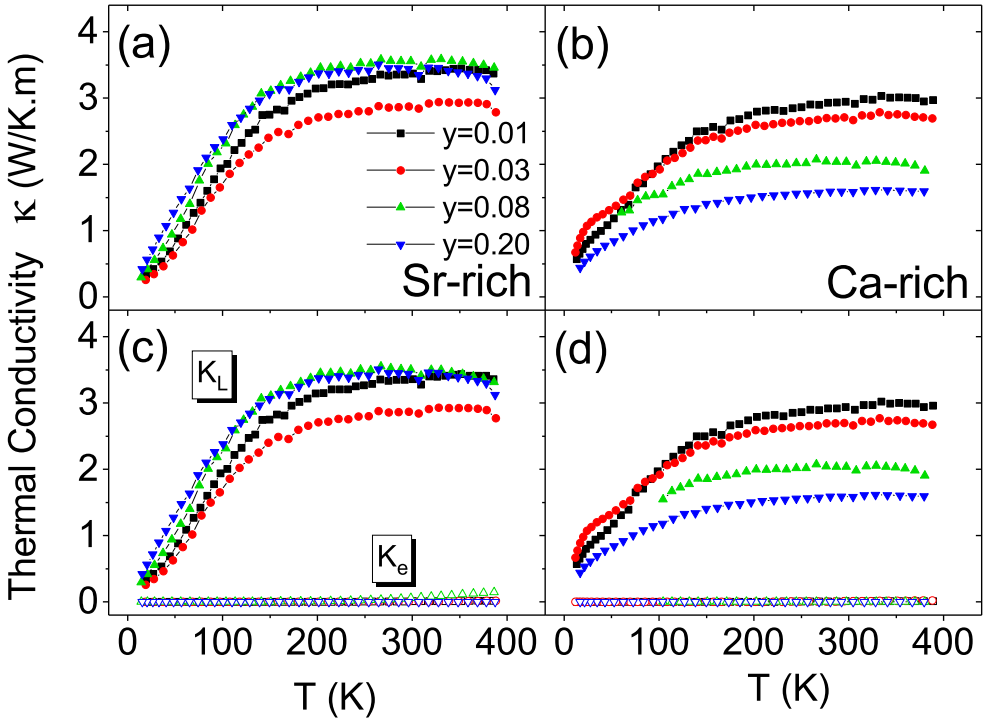

Figure 4.13: op panels (a, b), total measured thermal conductivity κ for the two $Sr_{1-x-y}Ca_xNd_yTiO_3$ series. Bottom panels (c, d), separating the temperature dependence of the electronic κ_e (open symbols) and lattice κ_L (filled symbols) thermal conductivities shows that the latter greatly dominates as the electronic part is negligibly small accounting for less than 2% of κ.

An estimate of κ_e was made using the resistivity data with fits modeled according to Wiedemann Franz law [88] $\kappa_e = LT/\rho$. We note here that the Lorenz number in the degenerate limit $L = \pi^2/3(k_B/e)^2$ is not suitable for calculating κ_e since our ceramic materials exhibit transport properties typical of semiconductors rather than metals. Therefore, L is instead calculated as a function of temperature from the absolute value of the measured Seebeck coefficient S in μV/K as L_S $(W\Omega K^{-2})$ $= 1.5 + \exp -|S|/116$ [207].

In the Ca-rich sample with Nd content y=1% for instance, we find that $L_S = 1.53 \times 10^{-8}\ W\Omega K^{-2}$ at T = 390 K while its low temperature/low Seebeck value of

2.2×10^{-8} $W\Omega K^{-2}$ is comparable to the degenerate limit which corresponds to a Seebeck value $S \sim 7\mu$V/K.

The range of L_S values in our materials is found in agreement with that of the recently reported magnetic field dependence of thermal conductivity in typical semiconductors [208]. The room temperature electronic thermal conductivity κ_e of our samples spans a wide range between 0.0001 and 15 mW/K.cm showing a range similar to La-doped $SrTiO_3$ (0-23 mW/K.cm) [34] with lightly-doped compounds (Nd 1–3 %) having an average κ_e of about 3 mW/K.cm comparable to that found in polycrystalline (Na,Ca)Co_2O_4 materials [209]. Such low κ_e values confirm that the electronic contribution is negligible compared to the lattice contribution κ_L, calculated as $(\kappa - \kappa_e)$, which is the dominant mechanism for heat conduction in our materials, see Fig. 4.13 (c,d) and Table 4.8.

Table 4.8: Ratio of the electronic κ_e to the total thermal conductivity κ at room temperature calculated using Lorenz number L ($W\Omega K^{-2}$) in the degenerate limit vs. L_S that is dependent on the Seebeck coefficient.

Nd content	κ_e/κ (%) ($L_S = 1.5 + e^{-\lvert S\rvert/116}$) $W\Omega\ K^{-2}$	κ_e/κ (%) (L= 2.44×10^{-8} degenerate limit) $W\Omega K^{-2}$
Sr-rich 0.01	0.24	0.39
0.03	0.12	0.18
0.08	1.54	2.07
0.2	1x10^{-3}	1x10^{-3}
Ca-rich 0.01	0.27	0.43
0.03	0.31	0.46
0.08	1x10^{-5}	1.3x10^{-5}
0.2	4x10^{-4}	5x10^{-4}

As temperature increases above 200 K, the measured lattice thermal conductivity κ_L in both series levels off and becomes nearly temperature independent. This

behavior could indicate a significant contribution from the temperature-independent point defect scattering to the thermal conductivity [210, 211].

The significant role of point defects was early identified around 1928 and promoted as a chief culprit of lattice thermal conductivity reduction in heavily doped semiconductor alloys by Eucken and Kuhn [212]. They found that random distribution of atomic mass difference decreases acoustic phonon velocity efficiently.

In addition to other sources of thermal resistivity, i.e. boundary conditions and the processes of phonon-phonon scattering (Umklapp and normal or momentum conserving three-phonon), point defects resulting from doping-induced mass fluctuations act as additional scattering centers for phonons and reduce the phonon mean free path λ_P [203], see Fig 4.14 for examples of phonon scattering mechanisms.

The different phonon scattering techniques shown in Fig. 4.14 are already employed to reduce κ_L in various materials as summarized for few examples in Table 4.9 to increase phonon scattering and reduce its mean free path.

Table 4.9: Phonons scattering methods applied to various materials.

Phonon scattering method	Material Example
"Rattling" centers	Skutterudites, Clathrates [201]
Complex structures	$Yb_{14}MnSb_{11}$ [215]
Vacancies, solid solutions	Half-Heusler systems [82]
Embedded Nanodot systems	Pb(Te,Se) [216]
Grain boundary	nanocrystalline BiSbTe [101, 217]

Our confirmed stoichiometric materials are characterized by the absence of extrinsic vacancies such that point defects are only present via doping process (viz. substitutional impurity point defects). Here, we investigate the effectiveness of doping in suppressing κ_L by numerically reproducing the measured data and evaluating separately the influence of A-site dopants as extrinsic phonon scatterers as compared

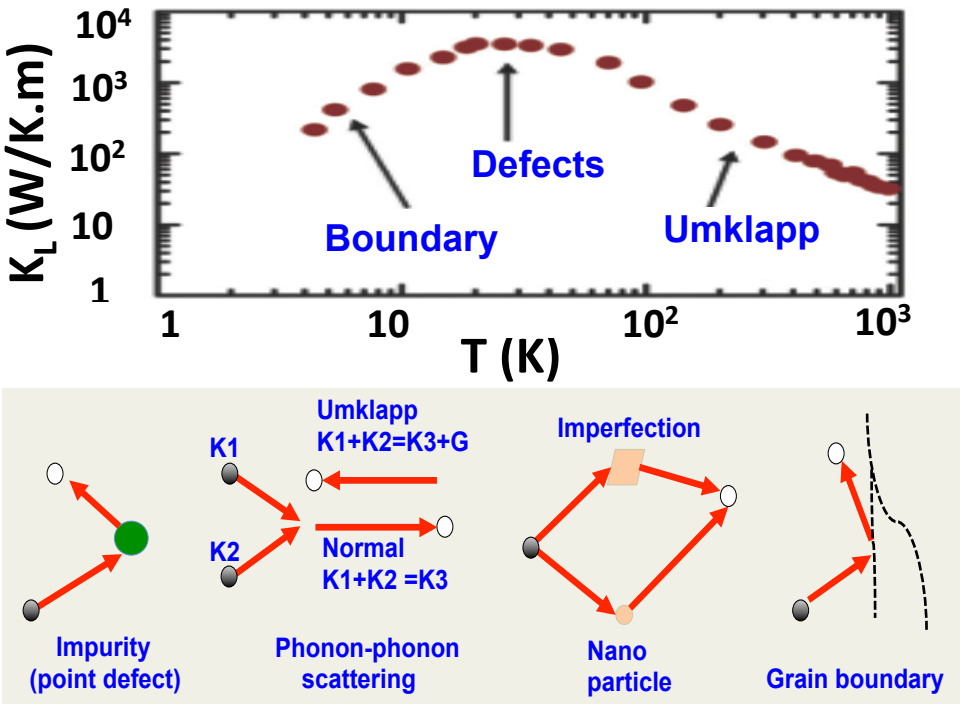

Figure 4.14: Top: Nearly universal shape of temperature dependence of thermal conductivity in typical solid (bulk silicon) [213,214] outlining the dominant phonon scattering mechanism depending on the temperature region. Bottom: Different sources of phonon scattering. All mechanisms except the normal phonon-phonon collisions (phonon redistributing effects) do not conserve the momentum in an attempt to restore the equilibrium Plank (thermal resistance) of the phonons in the materials.

to other heat conduction reducing mechanisms. Based on considerations of thermal resistivity due to exclusively phonon-phonon interactions, the expected lattice thermal conductivity κ_L can be estimated using $\kappa_L = 5.72 \times 10^{-6}\ M\theta^2\ V_0^{13}/\gamma^2$ [218] as $\sim$ 19.2 and 17.6 W/K.m for the parent $SrTiO_3$ and $Sr_{0.57}Ca_{0.23}Nd_{0.20}TiO_3$, respectively. V_0 is the average volume per atom in Å^3, M is the average atomic mass per atom, θ is the Debye temperature (we used θ = 400 K for $SrTiO_3$ [219] and 384 K for our Ca-rich sample determined from the refined U_{iso} values as will be shown below), and γ is the Grüneisen constant with an upper limit $\sim$ 2. While the measured

$\kappa_L = 11.8$ W/K.m for pure $SrTiO_3$ [34, 205] is indeed comparable to our estimated values, we find that the experimentally measured value for $Sr_{0.57}Ca_{0.23}Nd_{0.20}TiO_3$ sample is approximately one order of magnitude lower (i.e., $\kappa_L = 1.59$ W/Km), Fig. 4.13 (b). Such a large difference between the observed and calculated values agrees with the assessment that significant contributions to thermal resistivity are present from other mechanisms chief among them is phonon scattering by point defects.

The quantum theory of solids treats the bulk lattice excitations (atomic vibrations around equilibrium atomic coordinates) as quantized acoustic waves called "phonons" where the acoustic phonon frequency (energy) w is given in Debye model approximation by the linear dispersion relation $w = v_S k$, v_S is the average sound velocity and w_{max} is upper limit Debye frequency of vibrations which is characteristic of material [220]. At a given temperature, the number of phonons present in the solid is given statistically by Plank distribution [221]. Under thermal gradient, the thermal conductivity depends on how long it takes the material to reach an equilibrium distribution state (i.e. relaxation time between phonons scattering events) where better thermal conduction is associated with larger relaxation time which in turn depends on the phonon frequency.

My calculations for lattice thermal conductivity κ_L that takes into account point defect contributions will be based on the model proposed by Callaway and von Baeyer [210, 211] in which it is assumed that heat is carried by acoustic phonons obeying linear dispersion relations and κ_L is directly proportional to the phonons overall frequency-dependent relaxation time $\tau(w)$ representing the sum of all possible phonon scattering processes and takes the form:

$$\kappa_L = \frac{K_B}{2\pi^2 v_s} \int_0^{K_B\theta/\hbar} \tau(w) \left(\frac{\hbar w}{K_B T}\right)^2 \frac{e^{\frac{\hbar w}{K_B T}}}{\left(e^{\frac{\hbar w}{K_B T}} - 1\right)^2} w^2 dw \tag{4.1}$$

$$\tau^{-1}(w) = Aw^4 + BT^3w^2 + v_s/L \tag{4.2}$$

K_B is the Boltzmann constant and v_S is the speed of sound. It is immediately clear from this set of equations that reducing lattice thermal conductivity (or equivalently reducing relaxation time) requires less contribution to heat transfer from acoustic long wavelength (low w) phonons. These specific heat carrying phonons are known to be scattered effectively by point defects.

The first term in Eq. 4.2 is associated with the scattering of phonons by atomic mass variations and its T-independent parameter A can be expressed as [222] $A = (V_0\Gamma)/(4\pi v_s^3)$

where Γ is the phonon scattering coefficient with a strength that depends on the degree of cationic intermixing at the perovskite's A-site having different atomic masses with smallest values of Γ corresponding to A-site single-ion compounds as shown in Fig. 4.15.

Each of our materials with a unique combination of (Sr,Ca,Nd) ions possesses a distinct Γ value (or equivalently a compositional mass disorder [223]) (see Fig. 4.15) calculated as [218, 224]

$$\Gamma(A) = \frac{N_A}{N}\left(\frac{M_A}{< M >}\right)^2 \sum_{i=1} f_i \left(\frac{m_i - M_A}{M_A}\right)^2 \tag{4.3}$$

Here, f_i and m_i are the fractional occupancy and atomic mass of the ith cation at the A-site, respectively. M_A is the average mass of A-site cations and <M>is the average atomic mass of the unit cell and N_A/N is the atomic number ratio of the A-site to the total unit cell content.

Surprisingly, as the Nd doping increases in our materials (Nd atomic mass = 144.2 g/mol larger than Sr = 87.6 g/mol and Ca = 40.1 g/mol combined), the linear increase of the average atomic weight of the A-site does not directly correlate with

the measured lattice thermal conductivity (as opposed for instance to the simple case in isostructural materials in Fig. 2.3 of chapter 2 where κ_L reduces with increased atomic weight). This can be seen for instance by examining the heaviest compositions in both series with the Nd content of 20% (i.e. Ca-rich $Sr_{0.57}Ca_{0.23}Nd_{0.20}TiO_3$ and Sr-rich $Sr_{0.80}Nd_{0.20}TiO_3$) with a very comparable A-site average atomic mass of 36.8 and 38.96 g/mol, respectively. Their atomic weight ratio ~ 1 does not account for the clear contrast in their measured thermal conductivity as the first exhibits the lowest room temperature $\kappa_L = 1.59$ W/K.m of all the studied materials while the thermal conductivity of the latter is twice as much or 3.44 W/K.m yielding a κ_L ratio ~ 2.2.

As shown in Fig. 4.15, we find that the measured κ_L for both series is rather related to the magnitude of the material's scattering coefficient Γ given by Eq. 4.3 (the ratio of Γ values for the two materials discussed above is ~ 2.5 close to their κ_L ratio). This observation clearly shows that κ_L is directly affected by the degree of mass disorder rather than the combined weights of the constituents. Of particular importance is the noted positive influence of Ca on reducing κ_L. In the Ca-free $Sr_{0.80}Nd_{0.20}TiO_3$ for example, the cations' mass fluctuation is minimized by the presence of only two constituents (Sr and Nd) at the A-site thus resulting in a small value for Γ (large κ_L) as opposed to enhanced scattering coefficient in Ca-added materials.

To be evaluated numerically, Eq. 4.1 for the lattice thermal conductivity κ_L can be re-written by setting a single integral parameter $x = \hbar w/K_B T$ with the maximum allowed phonons frequency wgiven by the Debye limit as:

$$\kappa_L = \frac{K_B}{2\pi^2 v_s}\left(\frac{K_B T}{\hbar}\right)^3 \int_0^{\theta/T} x^4 \frac{e^x}{\left(Dx^4 + Ex^2 + v_s/L\right)\left(e^x - 1\right)^2} dx \qquad (4.4)$$

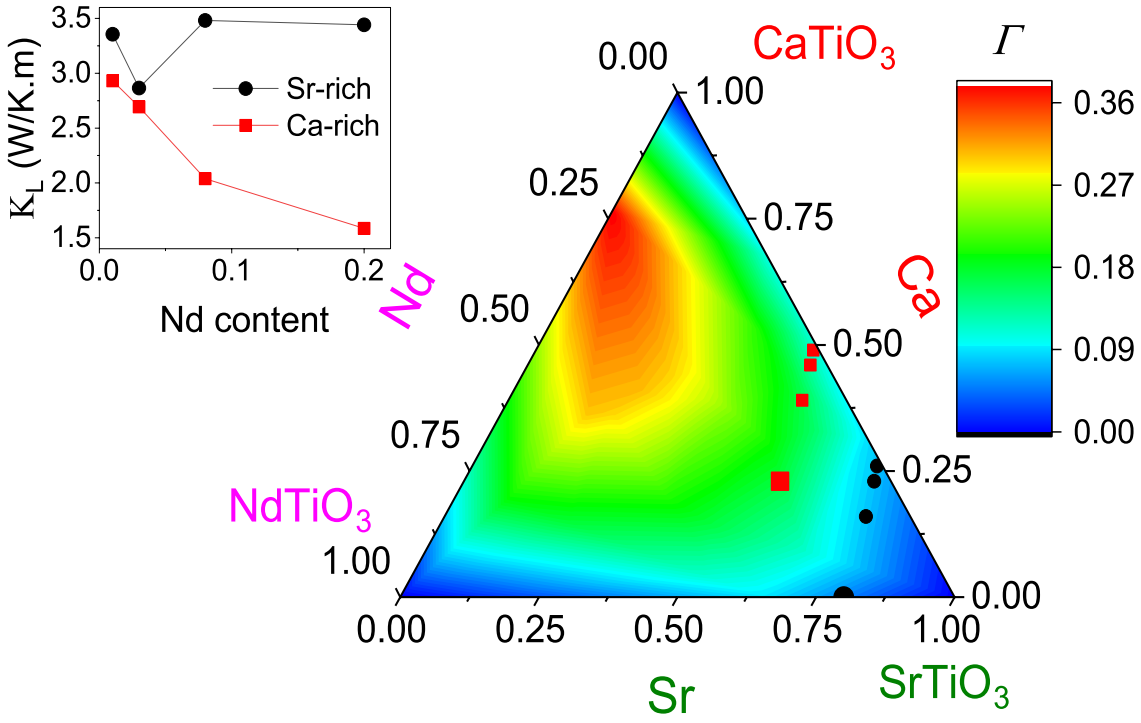

Figure 4.15: Ternary contour plot of Γ as a function of A-site compositions is shown where smallest Γ values (blue regions) correspond to single-ion compounds. Room temperature lattice thermal conductivity κ_L and scattering coefficient Γ are correlated. For instance the two heaviest compositions with Nd 20% (their Γ values are emphasized by the larger symbols in the ternary contour graph) have nearly identical unit cell atomic weight but κ_L for the Ca-rich material is the lowest ~ 1.5 W/K.m due to the presence of Ca that maximizes Γ while the Sr-rich analog has the highest value ~ 3.5 W/K.m among all studied materials due to its small Γ value.

$D(T) = A(K_BT/\hbar)^4$ is the point defects scattering, $E(T) = CT(K_BT/\hbar)^2$ corresponds to phonon-phonon scattering with C parameter approximated from the measured κ_L of pure $SrTiO_3$ as [211, 225] $\kappa_L = K_B^2\theta/(2\pi^2 v_s \hbar CT)$ where contributions from point defects are minimal, resulting in relaxation time CT value ~ 1 femtosecond. The term v_S/L is the boundary scattering contribution which has no explicit temperature dependence with L as the characteristic length scale of the

material. The speed of sound v_S is given by the Debye approximation [221, 226] as $v_S = (V_0/6\pi^2)^{1/3} K_B\theta/\hbar$.

In order to accurately model κ_L, Debye temperatures of the materials in this study are determined from fitting atomic displacement parameters U_{iso} (Å^2) of the A-site and B-site cations that we obtain from applying the Debye model to fit highly-reliable NPD refinements results, as shown in Fig. 4.16 for Ca-rich series, from which θ values were estimated (listed in Table 4.10) according to the integral expression [190, 227].

$$U_{iso}(T) = \frac{3h^3T^2}{4\pi^2 K_B M\theta^3}\int_0^{\theta/T}\frac{xdx}{e^x-1} + A \tag{4.5}$$

A is the zero-point parameter of the atoms giving U_{iso} near zero Kelvin. The displacement parameters for each atomic site for all samples converge to nearly equal values at very low temperatures.

Table 4.10: Debye temperatures θ obtained from refined atomic displacement parameters

Nd Content (y)	Ca-rich θ (K)	Sr-rich θ (K)
0.01	373.8	370
0.03	385.9	405.2
0.08	410.2	379.2
0.20	384.2	446.2

Contributions to room temperature κ_L from different scattering mechanisms are separately examined and their values are summarized in Table 4.11. Point defects are indeed found to be the dominant scattering process and disregarding their influence would result in a three-fold discrepancy between the calculated and measured thermal conductivity values as shown in Fig. 4.17 for a representative sample (Ca-rich Nd = 20%). The characteristic length scale L that yields the best fit is $\sim$ 10–60

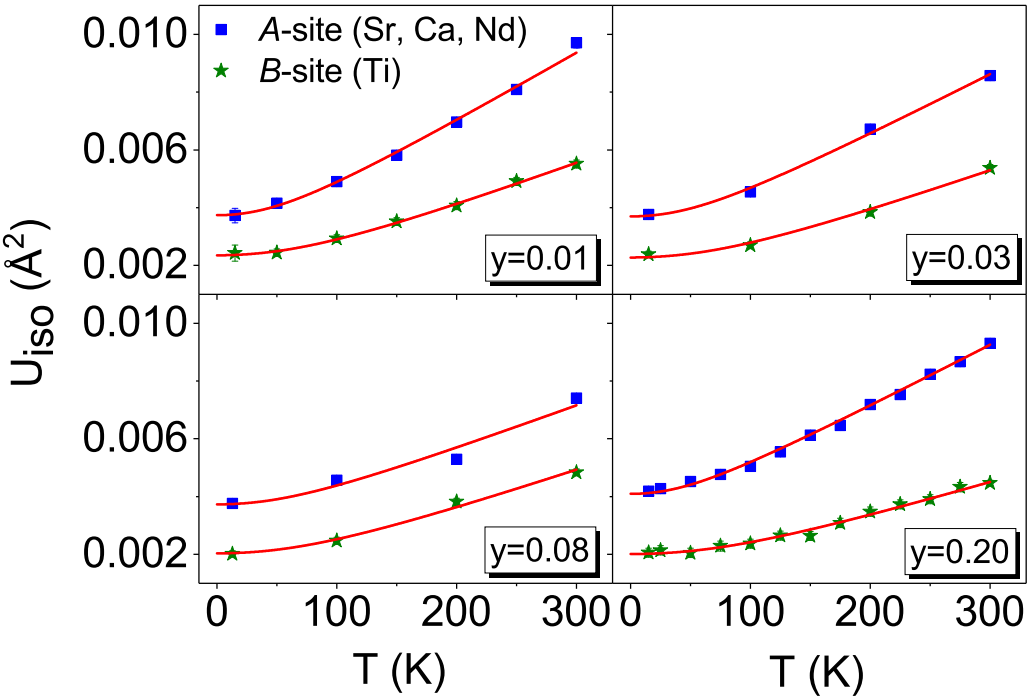

Figure 4.16: Debye model fits of the atomic displacement parameters U_{iso} for the Ca-rich series obtained from refinements using time-of-flight neutron powder diffraction. U_{iso} varies smoothly with temperature and converges to similar values for all materials at sufficiently low temperature.

nm which indicates that the phonons scatter effectively at the boundary of about 100 unit cells.

The fitting of measured κ_L(T) of all samples in the temperature range 10– 400K is shown in Fig. 4.18. The observed deviation of calculated κ_L at low T is expected as the normal phonon-phonon scattering term has a complex dependence on temperature and phonon frequencies [211]. Despite recent efforts to identify the limitations of Callaway's classical model for phonon thermal transport [228], including the assumption of weak Umklapp scattering and excluded optical phonon

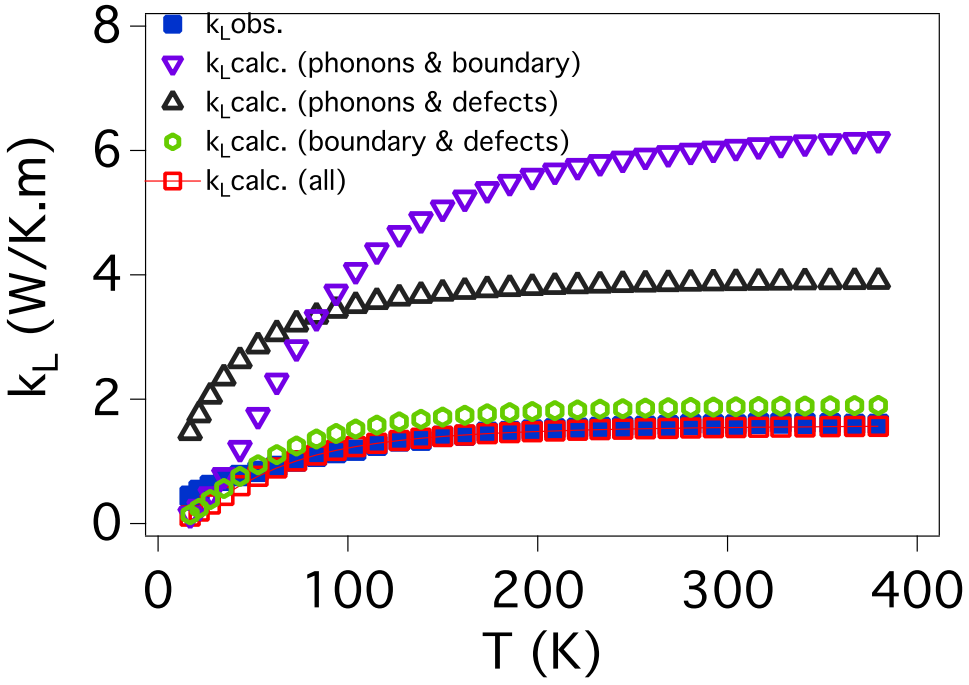

Figure 4.17: Contributions from different phonon-reducing processes evaluated analytically using Callaway and von Baeyer's model and compared to the measured lattice thermal conductivity κ_L of the Ca-rich sample with Nd content y = 20%. Best fit to the observed data corresponds to the presence of appreciable point defect contributions to phonon scattering.

contributions, we find it practically sufficient as it describes well the κ_L behavior for all the oxide materials studied here to a relatively high temperature of $\sim$ 400 K.

4.6.2 Electrical Conduction in $Sr_{1-x-y}Ca_xNd_yTiO_3$

Tuning the electrical conductivity σ of ceramic oxides is possible either by doping or by creating oxygen vacancies [106]. The highest conductivity measured in our materials is that in the Sr-rich Nd 8% sample with resistivity (10 $m\Omega.cm$ at 300

Table 4.11: Calculated room temperature lattice thermal conductivity κ_L in (W/K.m) at room temperature for the two $Sr_{1-x-y}Ca_xNd_yTiO_3$ series assuming the presence of different combinations of phonon scattering mechanisms.

Nd Content (y)	κ_L Obs.	κ_L Calc.(All)	κ_L ($v_S/L \sim 0$)	κ_L (E$\sim$0)	κ_L (D$\sim$ 0)	κ_L (Only E)
Sr-rich 1%	3.36	3.32	5.1	5.51	8.82	11.31
3%	2.87	2.84	5.11	4.21	7.63	11.31
8%	3.5	3.38	4.99	5.78	9.01	11.29
20%	3.44	3.42	5.73	5.59	7.77	11.26
Ca-rich 1%	2.94	2.83	4.28	4.41	8.96	11.36
3%	2.7	2.66	4.27	4.05	8.86	11.36
8%	2.04	1.99	4.06	2.62	7.33	11.35
20%	1.59	1.55	3.88	1.87	6.05	11.30

K) significantly lower than that reported for polycrystalline $Ca_3Co_4O_9$ (15 $m\Omega.cm$) [104] but about one or two orders of magnitude larger than $NaCo_2O_4$ [81] and Bi_2Te_3 [80] single crystals which is still considered practically acceptable considering the polycrystalline nature of our materials.

Thermal variations of the resistivity $\rho(T)$ of our Nd-doped materials are shown in Fig. 4.19. Upon warming, the samples exhibit a non-metallic semiconducting/insulating behavior with negative $d\rho/dT$ slopes that seem to indicate that the transport of charge carriers (electrons) is thermally activated.

4.6.2.1 Lightly doped materials (y=1– 8 %)

The thermal evolution of the logarithmic resistivity in the Ca-rich materials is depicted in Fig. 4.20. A careful examination of the resistivity data reveals distinct behavior at three different temperature regions. According to a simple band-gap picture, conduction occurs when electrons injected into the lattice via Nd^{3+} dop-

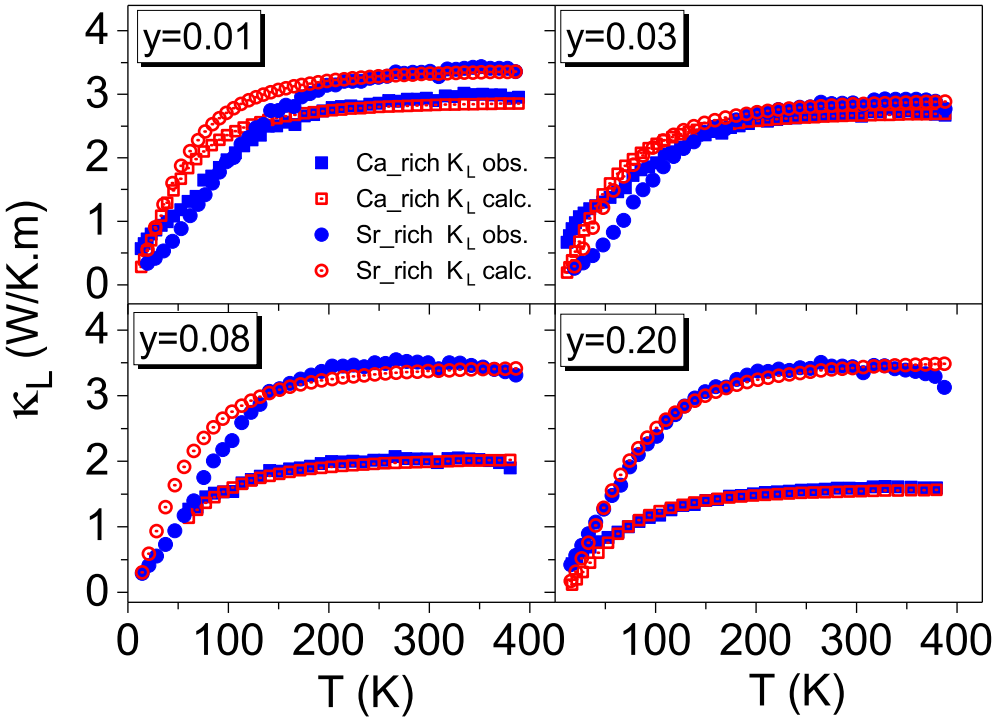

Figure 4.18: Measured lattice thermal conductivity κ_L of Ca-and Sr-rich materials fit analytically with a lattice heat conduction model that takes into account phonons scattering by point defects. Experimental data are reproduced to a sufficient accuracy in the temperature range 100-400 K.

ing and forming a Ti^{3+} 1-electron t_{2g} impurity states are thermally activated into conduction band akin to the conduction process in n-type semiconductors [229]. Electronic transport can then be modeled using the Arrhenius relation [230]

$$\rho(T) = A\ exp\left(\frac{E_a}{K_B T}\right) \tag{4.6}$$

Where A is a pre-exponential temperature-independent factor, T is the absolute temperature and K_B is Boltzmann's constant and E_a is the activation energy [229, 231] and its value corresponds to the charge carriers contributions to the measured conductivity from various depths of the impurity energy levels.

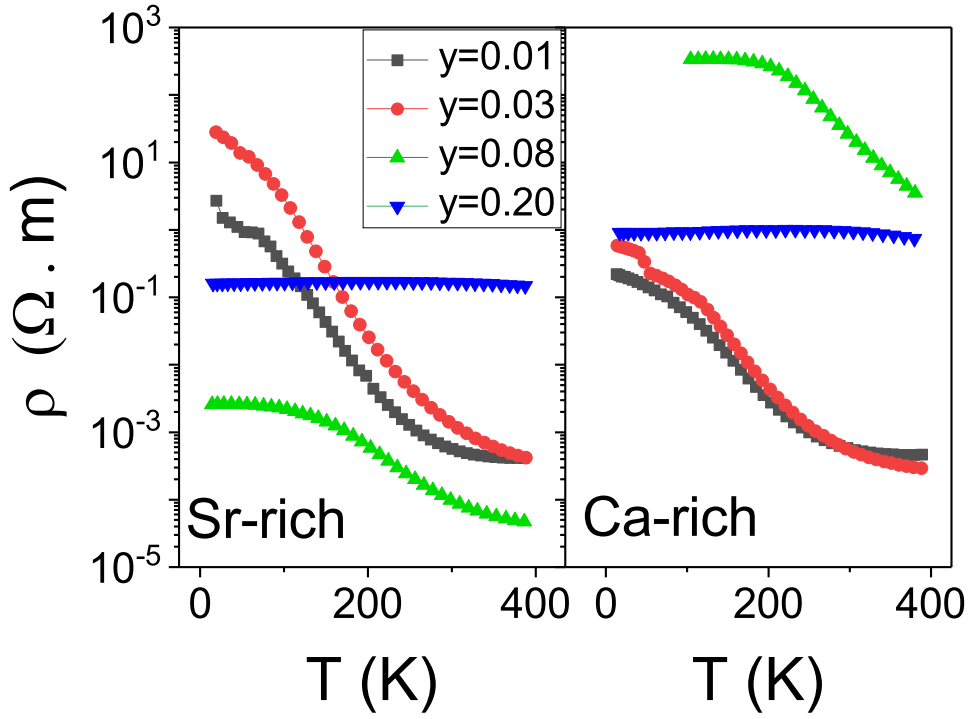

Figure 4.19: Temperature dependence of the resistivity ρ for our two series. Clear negative slopes (non-metallic behavior) indicate underlying thermally activated conduction processes in the lightly doped samples (y = 1– 8%).

Resistivity data (Fig. 4.20) of $Sr_{0.50}Ca_{0.49}Nd_{0.01}TiO_3$ (y =0.01) in a wide-T region (T= 400 – 115 K) follows the thermal activation conduction mechanism by exhibiting a perfect linearity between $\log \rho$ vs. 1/T in accordance with Eq. 4.6. The temperature-independent activation energy E_a obtained from the slope is 75.1 meV indicating that the conduction is this region is likely dominated by contributions from moderately deep donor levels [232]. Around T $\sim$ 115 K, a non-linear but smooth transition in a narrow temperature window of about 40 K is followed by the resistivity taking a linear detour characterized by a shallower slope. Such a behavior is fully accounted for by considering a second thermally activated region in the range T = 76 – 40 K for which the obtained activation energy decreases to E= 4.15 meV. The available thermal energy in this region is only sufficient for the

excitation of shallow band electrons. A simple picture of the process of thermal activation is shown schematically in Fig. 4.21.

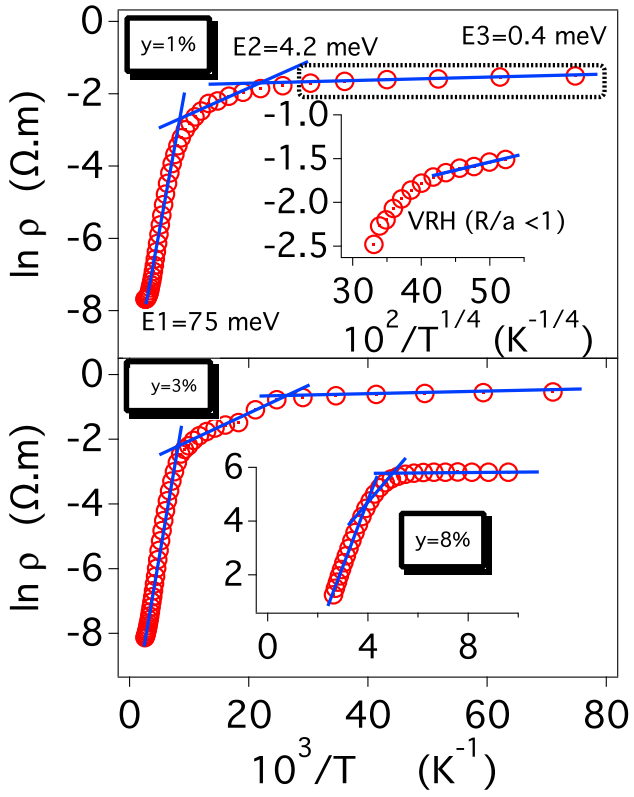

Figure 4.20: Variations of the logarithmic resistivity as a function of inverse temperature in the lightly doped Ca-rich series (Nd: y = 0.01 – 0.08). Thermal activation of 1-electron band is the predominant charge transport mechanism for these compositions.

Variable range hopping (VRH) is a different transport mechanism put forward by Mott [233] as a plausible source for low-T conduction in doped semiconductor and some perovskite oxides [234] in which the temperature dependence of resistivity takes the form [233, 235]

$$\rho(T) = B\ exp\left(\frac{T_0}{T}\right)^{1/4} \tag{4.7}$$

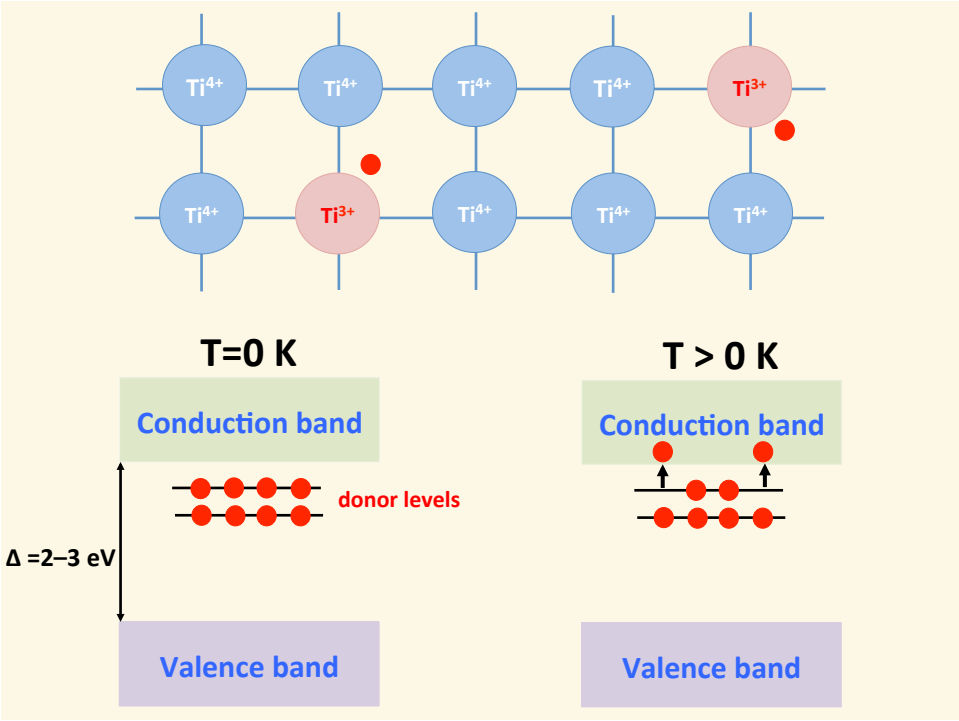

Figure 4.21: Thermal activation of impurity level states to final states in doped semiconductors where resistively dependence on temperature closely follows the Arrhenius law.

B and T_0 are constants. I have investigated this alterative model for data below 40 K in the Ca-rich sample (y = 0.01) as shown in Fig. 4.20. While Mott's VRH model fits the data very satisfactorily, the obtained value of the characteristic temperature T_0 = 12 K, from the slope of the line of ln(ρ) vs. $T^{-1/4}$, implies that the hopping range (R) between localized states beyond nearest neighbors is not attained [236] as R/a (= 3/8 $[T_0/T]^{1/4} > 1$) is significantly less than one ($\sim$ 0.3) in the entire region below T = 40 K. Electrons localization length (a) is equivalent to the distance between two TM ions which we obtain from NPD refinements of lattice constants. Thus, the measured conductivity is explained instead based on a third channel of very shallow electron levels being able to become thermally excited with E_a = 0.37 meV.

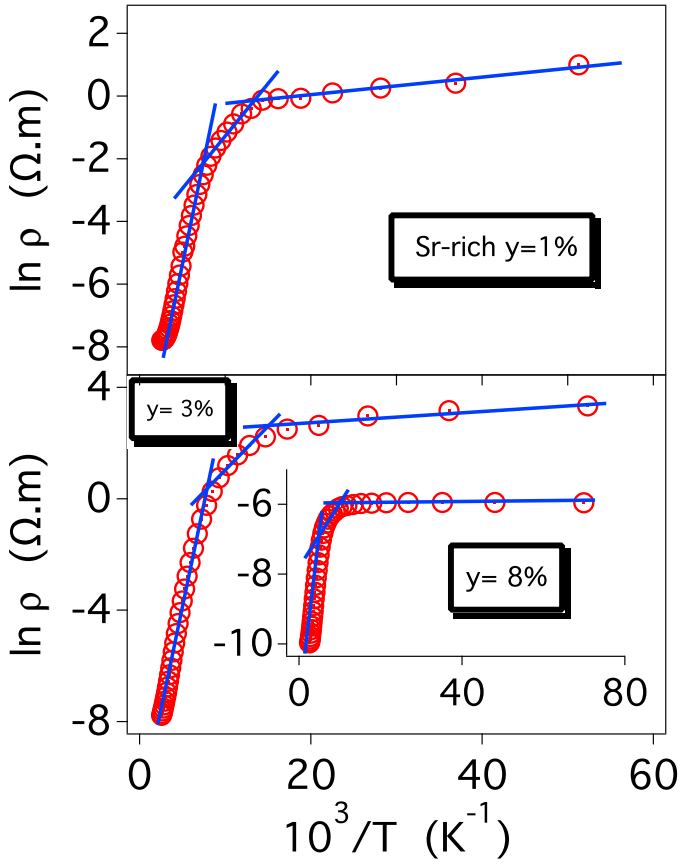

Figure 4.22: Logarithmic resistivity as a function of inverse temperature for the Sr-rich samples (y = 0.01 – 0.08) where the conduction is described as thermally activated with dissimilar activation energies (slope changes/discontinuities) in different temperature regions.

Analysis of the temperature dependence of resistivity of Ca-rich (y = 3 and 8 %, see Figs. 4.20 and 4.23) and Sr-rich materials (y = 1– 8 %, Fig. 4.22) reveals that the conduction behavior is identical to Ca-rich with y = 1 % sample and follows thermally activated mechanism. The linearity of the logarithmic resistivity vs. T^{-1} is well sustained across the entire studied range of temperatures 10–400 K with different slopes corresponding to the activation energies $E_1 > E_2 > E_3$ and thus data can be well described by a single expression [237] $\rho(T) = A_1\, exp(E_1/K_BT) +$

$A_2\ exp(E_2/K_BT)+A_3\ exp(E_3/K_BT)$. Similar slope discontinuities are also found in resistivity plots of reduced $SrTiO_{3-\delta}$ [238] and n-type doped Skutterudite compounds [239].

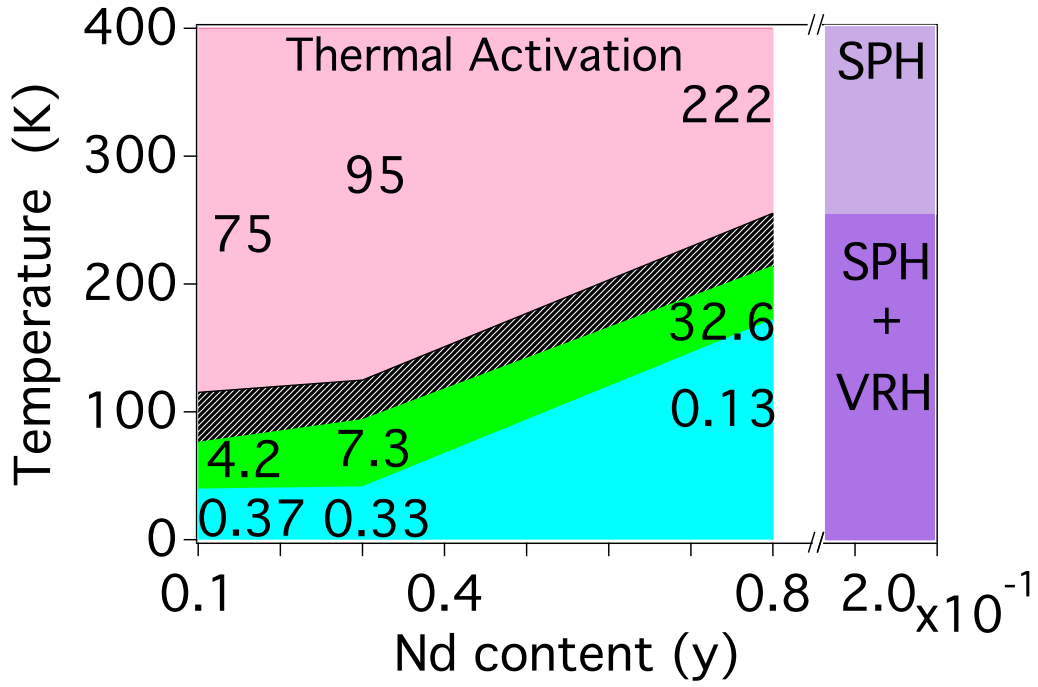

Figure 4.23: Resistivity activation mechanisms as a function of Nd doping in the Ca-rich series. The activation energy (numbers printed in the different regions) is strongly dependent on the Nd doping levels or charge carrier concentrations. The hashed/shaded region corresponds to transitions from deep to intermediate-donor conduction. Increased band filling to Nd (20%) leads to the formation of small polarons.

4.6.2.2 Heavily doped materials (y = 20 %)

Electrical conduction of the heavily doped (y = 20%) samples in both series is shown in Fig. 4.24. Both models of Arrhenius band-like thermal activation and VRH conduction fail to account for the observed complex resistivity patterns that

fundamentally differ from the behavior in the lightly doped samples (show no direct correlation between $\log \rho$ and $1/T$) and might be due to the significantly larger concentrations of Ti^{3+} ions.

It has recently been suggested that an increased level of carrier concentrations in titanates such as in reduced $SrTiO_{3-\delta}$ could lead to the formation of small polarons [240, 241] which requires large presence of mixed valence states (Ti^{3+}/Ti^{4+}) and consequently the charge transport occurs via thermally activated hopping of small polarons (SPH) which is a widely recognized conduction mechanism in rare-earth doped manganites, for example, in their insulating (semiconducting) regimes [234, 242]. The stability of small polarons requires the strong localization of electrons which in the heavily doped samples is provided via a highly disordered mixture of multivalent Ti ions (Ti^{4+}, Ti^{3+}) and the presence of strong doping-induced fluctuations in the lattice potential [230, 231]. Additional evidence for the stability of small polarons formation can be inferred from the increase in the measured average bond length [Ti –O] in the heavily doped sample with an elongation by $\sim$ 0.01 Å sufficient for the development of localized small polarons on the isolated Ti^{3+} sites [241].

Electrical transport by small polarons hopping through successive nearest neighbor sites is given by Mott expression [233] as

$$\rho = \rho_0 T \; exp\left(\frac{E_P}{K_B T}\right) \tag{4.8}$$

Resistivity data of Ca-rich material (y = 20 %) is fitted using this model with a best fit for T >244 K, a temperature that is comparable to T $\sim \theta/2$ (θ is the Debye temperature) at which the theory indeed predicts that thermal energy is enough for dominated hopping by nearest neighbors by thermal activation [233]. Activation

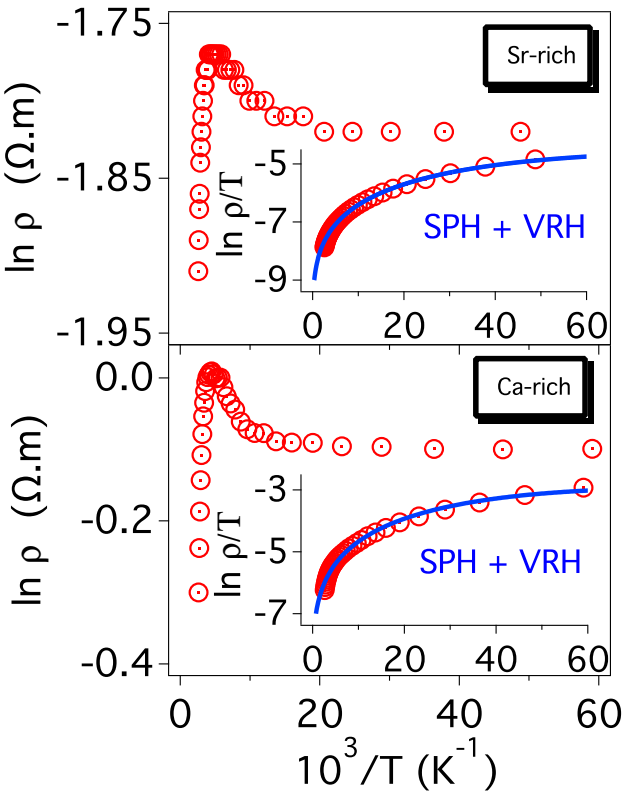

Figure 4.24: Variation of the logarithmic resistivity as a function of inverse temperature in the heavily doped y = 20% materials. Unlike the lightly doped materials, there is no clear correlation between $\log \rho$ and $1/T$. High-T region (above $\sim \theta/2$) corresponds to thermally activated small polarons whereas variable range hopping explains well the low temperature data.

energy E_p determined from the slope is 42.8 meV. Useful information about the different parameters in small polarons model can be obtained from the fit which gives the value for the prefactor $[K_B/v_{ph}Ne^2R^2y(1-y)]e^{(2\alpha R)}$ as $\rho_0 = 5.789 \times 10^{-4}\ \Omega.m$ for the heavily doped Ca-rich material. N is the number of transition metal ions per unit volume obtained from NPD refinements ($N = 4.24 \times 10^{21} cm^{-3}$), y is the polaron occupied site which is equal to the Nd doping level (y = 0.20), α is the electron wave function decay constant (localization length = $1/\alpha$ = 1.6 Å), R is the average spacing between transition metal ions [242] ($R = (1/N)^{1/3} \sim R = 6.2$

Å),and v_{ph} is the optical phonon frequency determined from Debye temperature to be 8x10^{12} Hz. The carriers localized as small polarons have a radius r_p that can be estimated as [243] $r_p = (1/2)[\pi/6N]^{1/3} = 2.5$ Å which is close to the average Ti–O bond length and comparable to small polaron sizes found in some manganite systems [243, 244].

Below T = 244 K where small polarons are not exclusively transported via thermally activated hopping to nearest neighbors, both SPH and VRH models mutually failed to explain the measured resistivity pattern and applying a convoluted model that combines the two becomes necessary which gives resistivity variations with temperature according to the expression [231]

$$\rho = \rho_0 \, T \, exp \left[\frac{E}{K_B T} + \left(\frac{T_0}{T} \right)^{1/4} \right] \tag{4.9}$$

Resistivity data for the heavily doped materials can now be well fitted as shown in the insets of Fig. 4.24 for both the Sr and Ca-rich series.

It is worth noting that while Ca-rich series is found to be single-phased *Pbnm* in the entire temperature range 10–400 K, the various first or second order phase transitions observed in Sr-rich series are not detected from transport measurements. The absence of anomalies in the thermoelectric measurements at the temperatures of phase transitions is indeed puzzling but not uncommon. For instance, despite the phase transition at 108 K from cubic to $I4/mcm$ in $SrTiO_3$, the absence of anomalies in the measurements of the dielectric constant was reported [108]. We believe the absence of any evidence of phase transitions in conductivity data is due to the nature of charge carrier conduction in our strongly correlated system. Doping created an impurity band whose conduction is not characteristic of itinerant electrons moving through the lattice and scattered by phonons rising from octahedral

rotations/titling associated with phase transitions. As such, phase transitions won't be reflected in measured conductivity. Nonetheless, large increase in tolerance factor upon warming up in our materials has impacted the thermoelectric properties via a marked enhancement of the material's power factor (PF) as will be discussed below.

4.6.3 Correlation Between Structural Properties and The Thermoelectric Power Factor (PF)

The TE performance of a material is greatly influenced by its Seebeck coefficient S (thermopower) which appears as a quadratic term in the expression for ZT and depends fundamentally on the carrier concentration n [91] and on the effective mass m* [245, 246].

Many transition metal oxides exhibit S values that increase upon warming and the materials presented here fall in line with a steady increase in S with temperature as shown in Fig. 4.25 approaching 400 μV/K which is twice the thermopower measured for some of the best TE semiconductors such as Bi_2Te_3 [80] and nearly four times that observed in TE oxides such as p-type $NaCo_2O_4$ [81] and n-type $SrTi_{0.80}Nb_{0.20}O_3$ [246].

The observation of nearly identical Seebeck values displayed by each pair of materials with nominally the same Nd content (i.e. same carrier concentration, n) indicates a well-controlled stoichiometry in agreement with the nature of the thermopower as an intrinsic property of the material [76, 205].

At the highest measured temperature T $\sim$ 400 K, Seebeck coefficient in our materials becomes closely comparable in value to Heikes prediction for transition

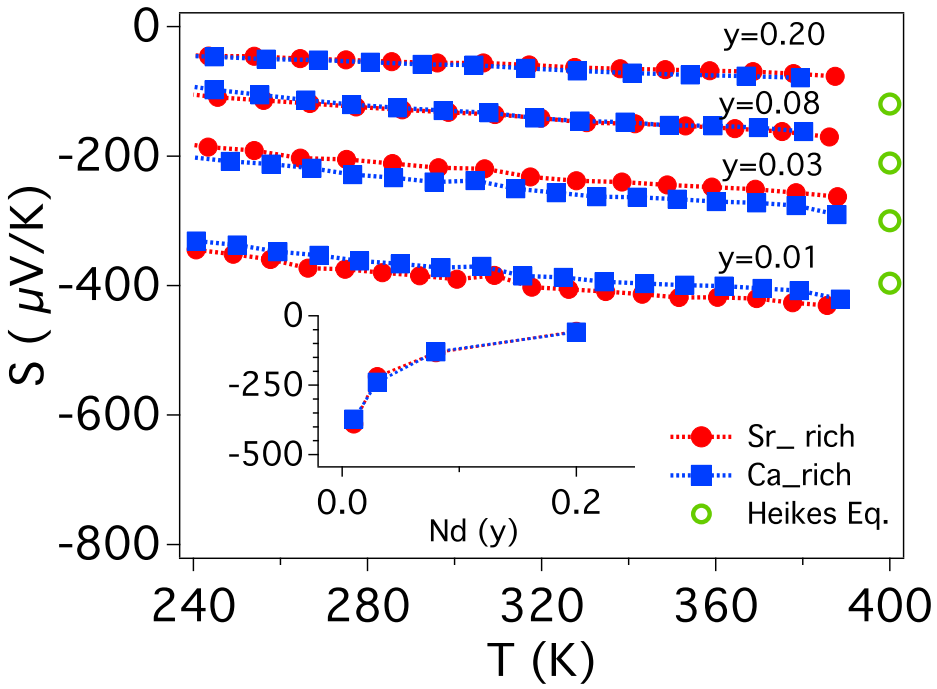

Figure 4.25: Steady increase in negative S values with increasing temperature for all materials approaching Heikes' predicted values (open green circles). Incorporation of Nd^{3+} ions into the lattice (increased carrier concentration) leads to a pronounced decrease in room temperature Seebeck coefficient S as shown in the inset where S values behaving in accordance with Heikes prediction.

metal oxides (shown as open circles in Fig. 4.25 without degeneracy term) [90, 91, 247] given as we have seen in chapter 2 for $Sr_{1-x-y}Ca_xNd_yTiO_3$ as [80]

$$S_{(T\to\infty)} = -\frac{K_B}{e}\left(\ln\frac{1-y}{y} + ln\ 6\right) \tag{4.10}$$

The negative sign indicates the nature of doping (n-type). The K_B/e ratio is equal to 86.25 μV/K. Seebeck coefficient for strongly correlated electron systems as the case in our materials is governed by the entropy of electronic states though Heikes standard formula [90, 91, 247].

The inverse proportionality between S and n is shown in Fig. 4.26 for S(T = 400 K) where the Nd doping greatly reduces the thermopower from around $S \sim 400$ μV/K for materials doped with only y = 1% to less than 100 μV/K in the heavily doped samples. The undesired effect of charge doping on S can be reversed and enhancement in the thermopower is expected due to possible spin/orbital degeneracy terms which in the case of Ti^{3+} ions can optimally boost the S value by $(-[K_B/e]\ln(6) = -154\ \mu\text{V/K})$ which takes effect when the material's structure transitions to the cubic symmetry at sufficiently high temperatures.

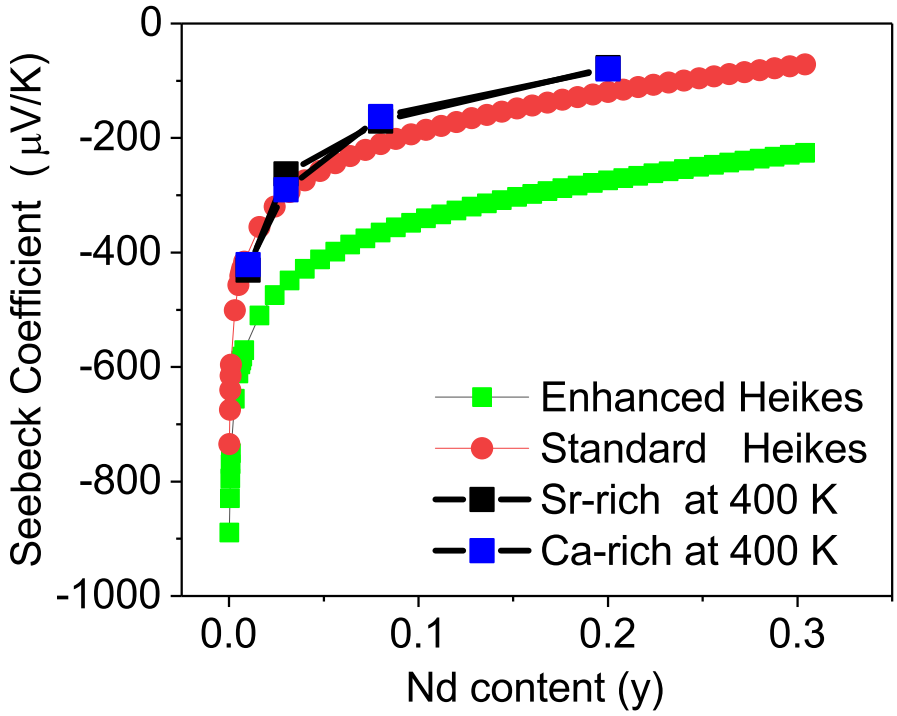

Figure 4.26: Using Eq. 4.10, calculated S values in Nd doping range y= 0 – 30 % are shown along with measured S values for y = 1, 3, 8 and 20 % at 400 K presented as square points in the same figure. This figure shows that full degeneracy enhancement is not yet reached perhaps due to the reduced ($I4/mcm$ and $Pbnm$) structural symmetry of both series at 400 K.

Temperature dependence of the thermopower is quite similar for all studied materials. Seebeck coefficient S data for both series shows a steady linear increase with increasing temperature but a clear transition to logarithmic dependence (see Fig. 4.27) occurs around $\sim$ 200 K above which we find that S varies linearly with $\ln T$ characteristic of a non-metallic behavior.

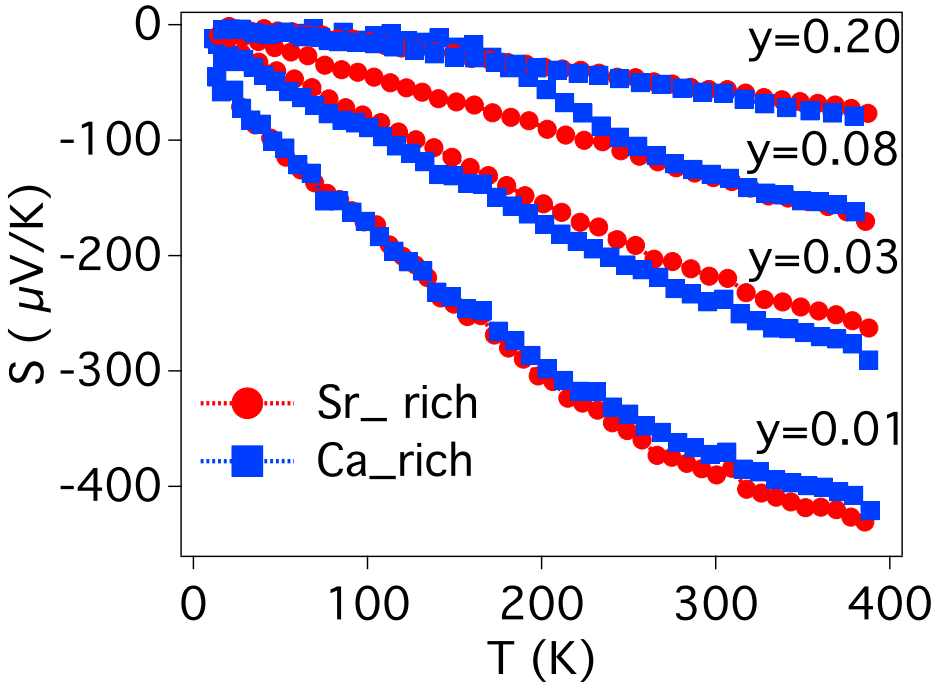

Figure 4.27: Plots of the measured Seebeck coefficient transition from linear dependence on temperature to a logarithmic dependence at T $\sim$ 200 K for all samples.

According to Mott, the intrinsic dependence of S on the carrier concentration n, effective mass m* and scattering mechanism of charge carriers r as a function of temperature for non degenerate impurity-doped semiconductors is given as [103,248]

$$S = -\frac{K_B}{e}\left[\frac{E_F - E_C}{K_B T} + r + 2\right] \tag{4.11}$$

This explains why value of S in semiconductors and metals are large where the Fermi level E_F lies deep within the energy band gap away from the edge of the conduction band E_C [95]. Eq. 4.11 will be used below to estimate the semiconducting energy gap in our materials and compare it to activation energies obtained from conductivity data. The value $E_F - E_C/K_BT$ depends on the effective mass m^* and n such that S is given as

$$S = -\frac{K_B}{e}\left[\ln\frac{2(2\pi m^* K_B T)^{3/2}}{h^3 n} + r + 2\right] \tag{4.12}$$

Equation 4.12 is simply another form of Eq.4.11 for S where E_F-E_C corresponds to the distance of the impurity level in (n-type) semiconductor from the (conduction) band edge [103]. The scattering factor r is equal to 0 for acoustic phonon scattering and 2 for ionized impurity scattering [249] and thus parameter r = 1 for mixed scattering seems to be the most suitable for our materials [250]. This formula can be re-written for S in units of μV/K by separating the competing effects of m* and n and thermal energy as

$$S(\mu V/K) = -86.25\ [53.68 + 3/2\ln T + 3/2\ln(m^*) + 3/2\ln(n) + r + 2] \tag{4.13}$$

The logarithmic dependence of S on n as required by this expression is already established for our materials as shown previously in Figs. 4.25 and 4.26. From the best fit of our measured thermopower to this equation, we were able to estimate effective mass of charge carriers in our materials as shown in Fig. 4.28 as function of carrier concentration. Not surprising is the finding that samples with same doping level have comparable m* (or equivalently similar S values as shown earlier).

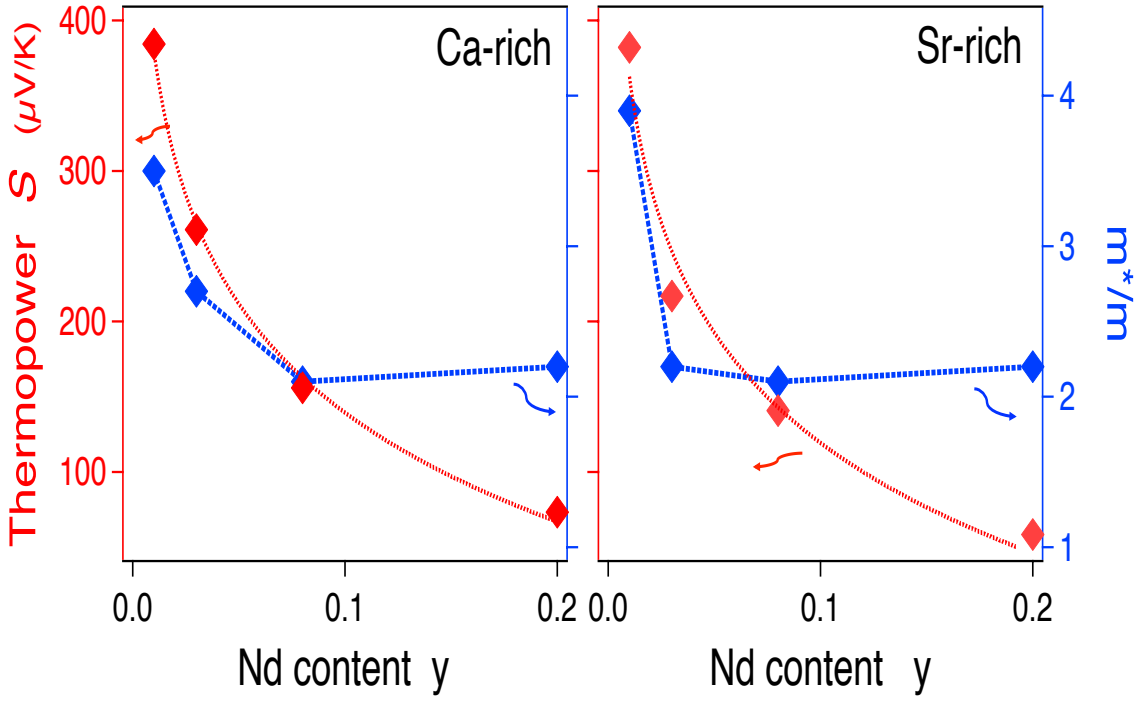

Figure 4.28: Incorporation of Nd ions into the lattice leads to a pronounced decrease in the effective mass m* (obtained from fitting Eq. 4.13 to measured Seebeck S data above 200 K) which in turn is reflected as reduction in S.

The theoretical prediction [245] of an inverse relationship between $m*$ and n is therefore sustained. The values of $m*$ for Nd 1% samples is comparable to effective mass m* of pure $SrTiO_3$ ($\sim$ 6 m_0) [108, 251] while heavily doped samples have m* value similar to the reported values for B-site doped bulk materials such as polycrystalline Nb 5%-doped $SrTiO_3$ ($\sim$ 1.9 m_0) [252]. On the other hand, Okuda and coworkers [34] estimated the effective mass of $SrTiO_3$ and 5% La-doped single crystal to be 1.17 and 1.62 m_0, respectively. The range of $m*$ of our samples is in good agreement with the literature values.

The highlight of this chapter is probably our observation of a strong correlation between the thermoelectric properties represented by the power factor $PF(= S^2\sigma)$ and the structural tolerance factor (representing all the structural parameters) for

all the materials in the present study in the temperature range between 13 and 400 K as shown in Fig. 4.29.

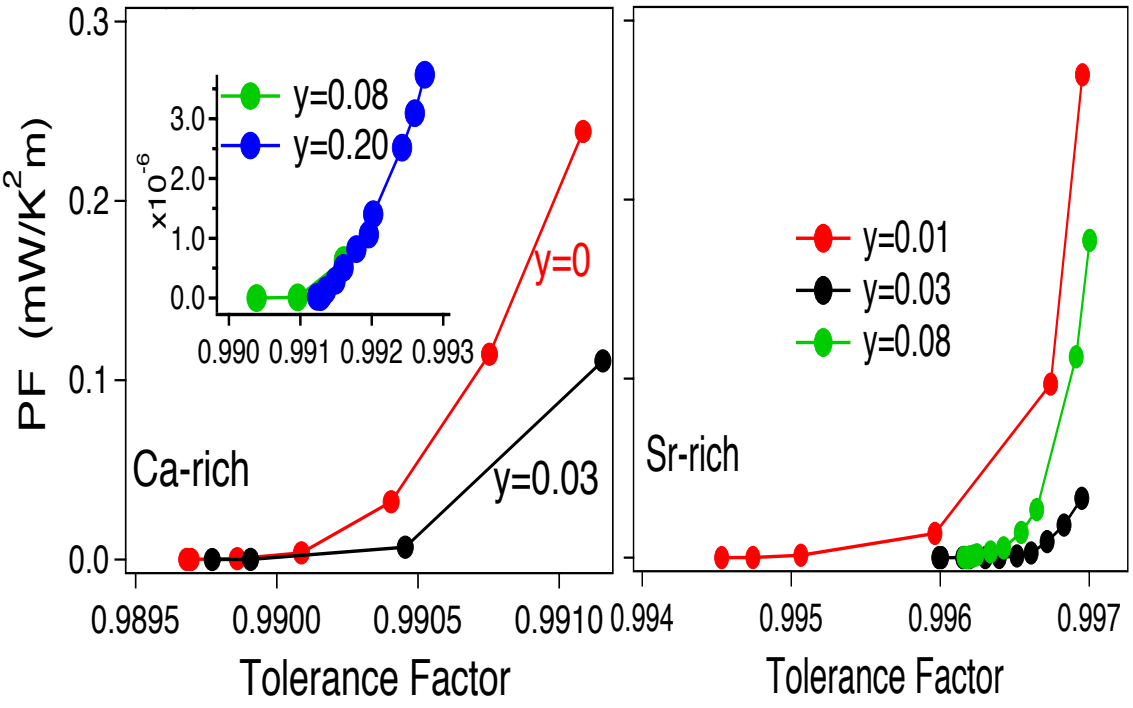

Figure 4.29: Variation of the TE power factor ($S^2\sigma$) with the tolerance factor. Strong correlation is observed between the two parameters for all the samples.

Since thermopower S values reflect the materials electronic properties, we expect S to show trends with temperature similar to that exhibited in the form of thermal activation of charge carriers in the conductivity data. Figure 4.30 shows representative samples from both series of material where S plotted as function of inverse temperature according to Eq. 4.11 in which the negative S decreases with increasing temperature exhibiting semiconducting behavior from which three distinct regions are identified. Semiconducting band gaps $= 2(E_F - E_C)$ as obtained from the slopes of the fits (listed in Table 4.12 for lightly doped samples) are comparable in magnitude to the activation energies Ea as determined earlier from the Arrhenius

plots of resistivity data as function of T^{-1}. This further confirms our assumption of thermally activated conduction in lightly doped materials.

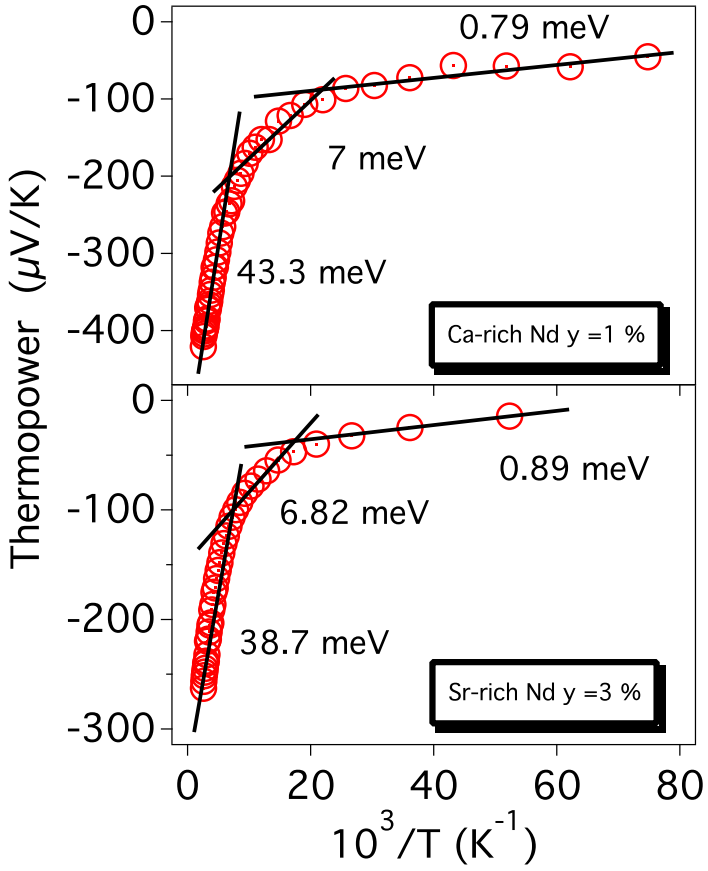

Figure 4.30: The thermopower S as function of inverse T in two representative compositions shows similar trend as the temperature dependence of resistivity with three distinct linear regions.

4.6.4 Figure of Merit (ZT)

The values of ZT appear to trend upward as temperature increases. While thermal conductivity is nearly constant above 200 K, this increase in ZT is primarily

Table 4.12: Comparison of the semiconducting band gap Δ obtained from variation of Seebeck coefficient as function of 1000/T vs. Arrhenius plots of resistivity measurements in the high T region for lightly doped materials (Nd y: 1–8 %).

Material	$\Delta = 2(E_F - E_C)$ from $S(T) = -K_B/e[(E_F - E_C)/(K_BT)]$	$\Delta = E_a$ (activation energy) from $\rho(T) = A\ exp(E_a/K_BT)$
Sr-rich Nd 1%	77.3	104
Sr-rich Nd 3%	97.09	133
Sr-rich Nd 8%	70.47	87.1
Ca-rich Nd 1%	86.49	75
Ca-rich Nd 3%	87.4	95
Ca-rich Nd 8%	91	222

driven by increased conduction of charge carriers as we saw in the section on electrical conductivity analysis. The increased localization of electrons and formation of small polarons in heavily doped samples is manifested by the suppression of the figure of merit despite the increase in their band filling compared to other studied samples. Only samples with the log of resistivity below 10^{-2} ($\sigma \geq 10^2\Omega^{-1}m^{-1}$) which is on the high end of conductivity range of a typical semiconductor) display non-vanishing figure of merit.

The highest figure of merit obtained in this study is for the 8% Nd-doped Sr-rich sample with a ZT value of ~ 0.07 at 400 K as shown in Fig 4.31 which is comparable to the value ($ZT = 0.08$) reported for 20% Nb-doped $SrTiO_3$ that possesses to the best of our knowledge the highest ZT value reported so far for n-type oxides. Additionally, our materials offer important advantages like the measured thermal conductivity κ which is less than half that in Nb-doped $SrTiO_3$ (=8 W/m.K) [76] and a Seebeck value $\sim 140\mu V/K$ for $Sr_{0.76}Ca_{0.16}Nd_{0.08}TiO_3$ which is significantly larger than the 100 μV/K reported for $NaCo_2O_4$ single crystals known to exhibit the best TE capabilities among all the related oxide materials. Taking these factors into

account, we can justifiably predict that our Sr-rich $Sr_{0.76}Ca_{0.16}Nd_{0.08}TiO_3$ sample should possess a ZT value at higher temperatures, when transition to the higher cubic symmetry with optimal orbital degeneracy occurs, that could easily exceed 0.37 [38] and thus could emerge as a very promising n-type oxide material for thermoelectric applications.

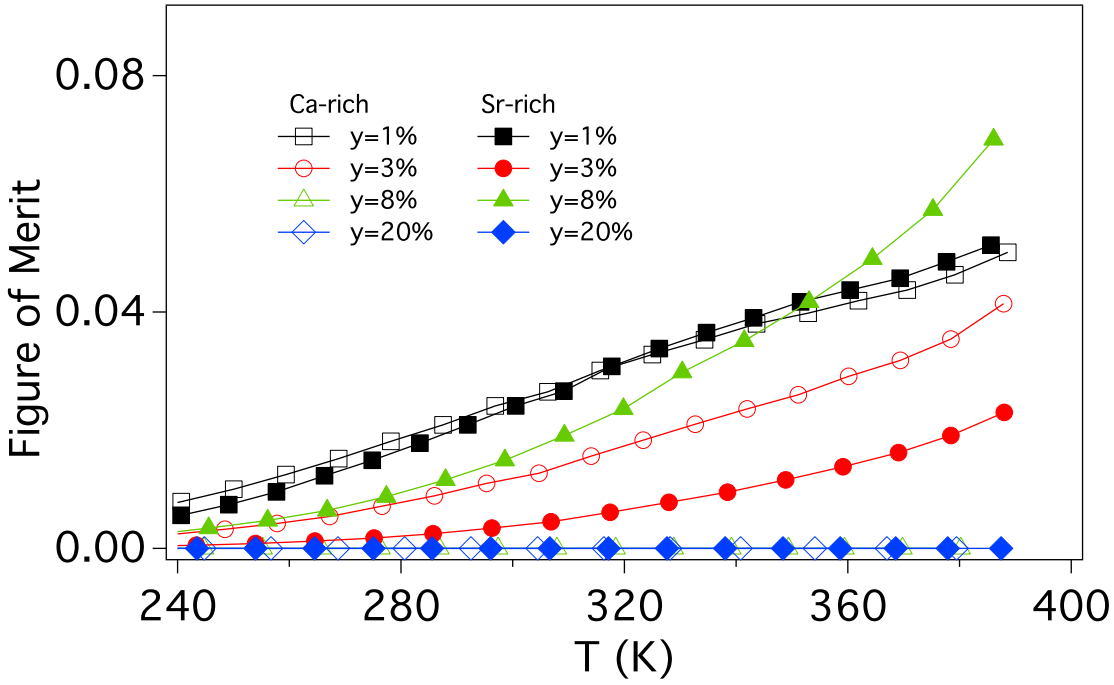

Figure 4.31: Figure of merit ZT in our martials with Sr-rich y=0.08 sample showing a relatively large value 0.07 thanks to a unique balance between high mobility, thermopower and low lattice thermal conductivity.

4.7 Conclusion

In conclusion, this chapter aimed to explore the thermoelectric potential of our substituted strontium titanates for meeting some of the rapidly increasing demand

for alternative energy. Two series of A-site doubly substituted $(Sr_{1-x-y}Ca_xNd_y)TiO_3$ materials have been successfully synthesized with various concentrations designed to exhibit two distinct nominally constant tolerance factor values at room temperature in agreement with our tolerance factor rules. The crystal structures of these materials have been characterized using high-resolution neutron powder diffraction as a function of temperature and Nd doping. At room temperature, the Sr-rich and Sr-poor series crystallize in the space group symmetries of tetragonal $I4/mcm$ and orthorhombic $Pbnm$, respectively, and remain so upon increasing the Nd^{3+} content. However, three different orthorhombic phases, $Pbnm, Ibmm, Pbcm$, are determined for the Sr-rich series as a function of decreasing temperature; whereas, for the Ca-rich series the $Pbnm$ structure persists throughout the studied temperature range.

Variations of structural parameters such as lattice parameters and tolerance factor were successfully correlated to changes in octahedral tilt angles. Room temperature bond lengths derived from NPD data for our oxygen stoichiometric samples were found to be consistent with the formation of Ti^{3+} ions which elongate the Ti–O bonds.

We have explored the thermoelectric properties enhanced by the incorporation of heavy Nd^{3+} atoms playing a dual role as effective scattering centers and as a source for conduction electrons. Thermal conductivity was measured for all samples and the electronic contribution was found to be negligible with heat conducted mainly though lattice vibrations (phonons). We were successful at experimentally achieving low thermal conductivity by enhancing phonon scattering which found to scatter effectively in our materials due to the presence of point defects introduced through a unique combination of A-site cations resulting in strong mass fluctuations (mass disorder) on the A-site that reduce the lattice thermal transport κ_L. Analytical modeling of the experimental data shows that point defects are the chief source for

phonon scattering events in the temperature range 100-400 K. The ability to assess contributions made by phonon scattering mechanisms separately is valuable for the design and prediction of thermoelectric properties of novel oxide materials.

Electrical resistivity behavior is found to be identical in both series. With light Nd doping levels, the resistivity is well explained by thermal activation of the electrons across impurity band gap. The electron localization increases in the heavily doped materials leading to the formation of small polarons. A convoluted model based on variable range hopping of polarons is necessary to describe the temperature dependence of resistivity below $\theta/2$, where θ is Debye temperature.

A combination of low thermal conductivity and enhanced carrier concentration has led to the creation of materials with very promising TE properties. The best stoichiometry lies in the neighborhood of 8% Nd-doped Sr-rich $Sr_{1-x-y}Ca_xNd_yTiO_3$ which is comparable to the best *TE* values reported for any oxide material; notably the n type *B*-site substituted $SrTi_{0.80}Nb_{0.20}O_3$ thermoelectric material. We succeeded in achieving a high figure of merit $ZT = 0.07$ at 400 K in the Sr-rich composition $Sr_{0.76}Ca_{0.16}Nd_{0.08}TiO_3$ which represents the best compromise between lowered the Seebeck coefficient and enhances conductivity with Nd concentration.

Further optimization of *TE* properties is possible for this system and single crystals with superior conductivity might boost figure of merit well above current reported value of 0.07 for polycrystalline materials. Additionally, with enhancement of the Seebeck coefficient together with even more reduced thermal conductivity expected at higher temperatures, we predict that our $Sr_{0.76}Ca_{0.16}Nd_{0.08}TiO_3$ and similar compositions have the great potential to become among the best known thermoelectric materials with practical *TE* capabilities.

In the next chapter, we shall continue the process of varying the structural properties of ABO_3 perovskite oxides with A-site doping but in contrast to doping

with smaller ions (Ca,Nd), a larger ionic size Alkaline earth (Ba) will be substituted for Sr utilizing its large size to strain the materials and promote ferroelectricity. Replacing Ti on the *B*-site with magnetic ion Mn, we will investigate the multiferroic properties of $Sr_{1-x}Ba_xMnO_3$ system and the controlling of structural behavior (such as the enhancement of Curie temperature) with variation of Ba content. We will limit the doping to *A*-site only similar to the case in titanates in this chapter since long range antiferromagnetic ordering in manganites can easily be disrupted by the doping of non-magnetic ion such as Ti which would lead to only diluted ordering.

CHAPTER 5

STRAIN-INDUCED TETRAGONAL DISTORTIONS AND MULTIFERROIC PROPERTIES IN POLYCRYSTALLINE $SR_{1-X}BA_XMNO_3$ (X = 0.43 - 0.45) PEROVSKITES

5.1 Introduction

The exciting discovery, two decades ago, of colossal magnetoresistance [253] in manganese-based perovskites led to intense explorations for other exotic ground states in this system including search for thermoelectric and multiferroic properties and materials with enhanced oxygen storage and fuel cell capabilities, etc. The rich playground that the manganites offer arises from a wide range of oxidation states, ionic sizes and coordination to oxygen the Mn ion assumes, and the delicate balance of a highly flexible structural framework coupled with complex electronic and magnetic properties.

With the search for new multiferroic materials reaching new heights, theoretical first-principles work predicted that polar distortions [33, 254, 255] should exist in alkaline-earth perovskite manganites $A\mathrm{MnO}_3$ (A= Ca^{2+}, Sr^{2+}, or Ba^{2+}) as a consequence of an overly increased A-site ionic size that enhances the local structural strains and promote ferrodistortive modes via the suppression of the more common antiferrodistortive (AFD) local instabilities [33]. In these studies, it was determined that Ba ions are large enough to stabilize a FE ground state in a hypo-

thetical $BaMnO_3$ perovskite material and for ferroelectricity to coexist with G-type antiferromagnetic (AFM) ordering [255]. Relatively large strains of $\sim$ 1–2% were determined as necessary to induce ferroelectricity in the paraelectric and magnetic $SrMnO_3$ [254] and $CaMnO_3$ [33] counterparts. Furthermore, recent conducted ab initio calculations [256] showed that if put under enough chemical pressures and epitaxial strains $Sr_{1-x}Ba_xMnO_3$ can be tuned between two distinctly different multiferroic states; one antiferromagnetic state coupled with small polarization and another ferromagnetic state producing a larger polarization.

In this chapter, I am exploring the multiferroic properties in the $Sr_{1-x}Ba_xMnO_3$ polycrystalline perovskites which share the common high symmetry (ideal) cubic structure with $(Sr_{1-x-y}Ca_xNd_y)TiO_3$ materials examined in chapter 4. The theoretically anticipated multiferroic properties of $Sr_{1-x}Ba_xMnO_3$ were experimentally demonstrated by Sakai et al. [125] who correlated the spontaneous polarization of their floating-zone grown SBMO crystals with strain-induced off-center displacements of the Mn and O ions akin to the singly ferroic $BaTiO_3$ system. $Sr_{1-x}Ba_xMnO_3$ (SBMO hereafter) is classified as a type-I multiferroic system in which independent microscopic origins give rise to the observed ferroelectric and AFM properties [135]. The novelty of SBMO is that the Mn in the Mn-O sublattice is the sole element responsible for both the ferroelectric and magnetic ordering and therefore the coupling between the two order parameters is expected to be strong. Indeed, recent work demonstrated the strong spin-phonon coupling properties [257–259] of SBMO making it, together with its large spontaneous polarization, a promising class of unique multiferroics.

Aside from a few limited investigations, most of the work hitherto on perovskite-type SBMO is either theoretical or performed on thin films and single crystals grown under non-equilibrium conditions. The synthesis of high quality $Sr_{1-x}Ba_xMnO_3$

(SBMO) polycrystalline samples crystallizing in the cubic perovskite structure is a daunting task as one would have to overcome challenging conditions that usually favor the formation of a more stable hexagonal polymorphs as in hexagonal $BaMnO_3$, for example [124].

Using an elaborate multistep fabrication technique, we previously produced pure $Sr_{1-x}Ba_xMnO_3$ samples with extended Ba solubility in a narrow phase space range $0 \leq x \leq 0.20$ [124]. The structure of these samples is cubic at all temperatures above their magnetic transitions with no sign observed for any ferro- or antiferrodistortive tetragonal distortions (i.e. MnO_6 octahedra rotations and distortions or Mn octahedra off centering). The purpose of the work in this chapter is to further extend the solubility limit of Ba and to explore the synthesis and structural properties of high quality bulk materials prepared under highly controlled equilibrium conditions. This includes achieving the desired multiferroicity and the determination by neutron diffraction of accurate values for the Mn^{4+} and O^{2-} atomic displacements in $Sr_{1-x}Ba_xMnO_3$ (x=0.43 and 0.45) that trigger the ferroelectric ordering [125, 259].

Results from this work should enable the development of newer multiferroic materials with enhanced properties by single or combined substitutions at the *A*- and/or *B* sites of the perovskite $SrMnO_3$ parent structure.

5.2 Magnetic measurements

Magnetic measurements were performed under Zero field-cooled (ZFC) in which the dc magnetization (M) data are collected as function of temperature in a magnetic field range of H=10 - 70 kOe as shown in Fig. 5.1 for $Sr_{0.57}Ba_{0.43}MnO_3$ and $Sr_{0.55}Ba_{0.45}MnO_3$ together with its first derivative with respect to tempera-

ture (dM/dT). Neel temperature of the antiferromagnetic transition of Mn^{+4} ions for each sample is corresponding to the global maximum of the temperature derivative of the magnetization (dM/dT) as shown in the insets of same figure. A dM/dT peak corresponding to the maximum magnetization slope (kink or steep steps in the M-T curve) [115] is observed at 196 ± 5 and 195 K for the x = 0.43 and 0.45 samples, respectively, in agreement with the neutron diffraction results.

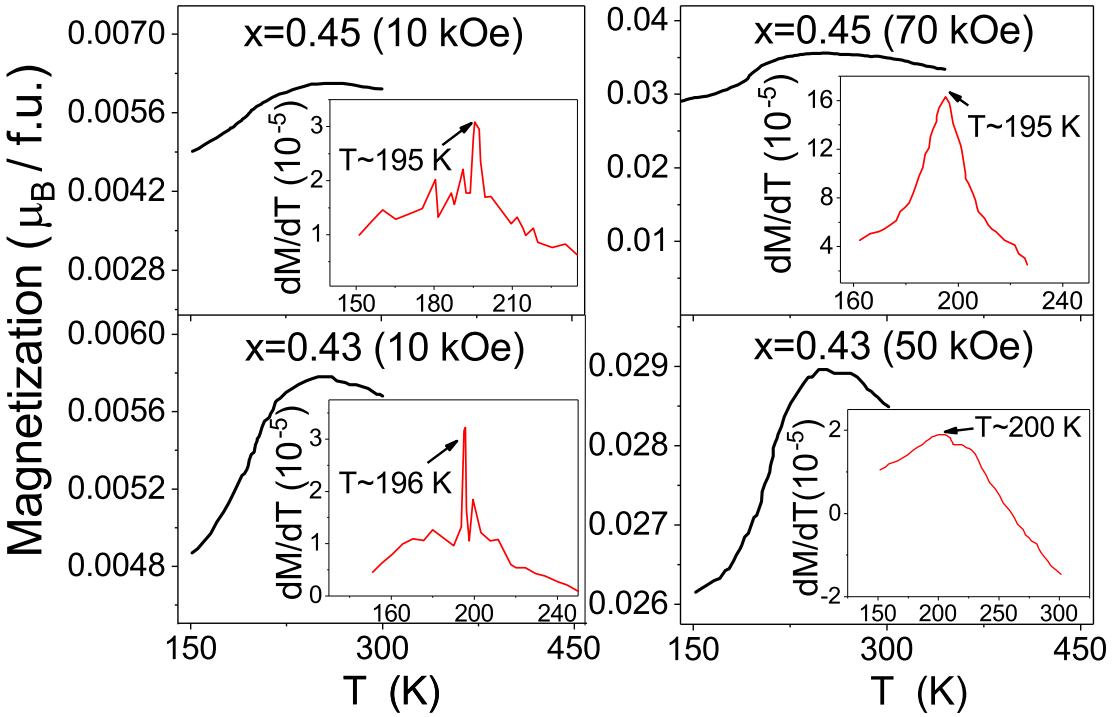

Figure 5.1: T profile of the "zero-field-cooled" (ZFC) DC magnetization measured in different magnitudes of external magnetic fields ranging between H= 10 – 70 kOe for $Sr_{0.57}Ba_{0.43}MnO_3$ and $Sr_{0.55}Ba_{0.45}MnO_3$ where a clear anomaly is observed around 196 ± 5 and 195 K, respectively, that is corresponding to the magnetic ordering transition.

5.3 Phase diagram of SBMO in the Ba compositional range (0 - 0.5)

The extended Ba solubility limit shown in Fig. 5.2 delineates the compositional phase space of the ferroelectric (FE) and multiferroic (MF) materials. The figure shows that the parent cubic $Pm\bar{3}m$ structure fails to distort for all the $x < 0.43$ synthesized compositions despite the significant strains they are subjected to. At low temperatures, these materials with half-filled t_{2g} orbitals, exhibit the expected G-type antiferromagnetic structure [124] with the Néel temperature, T_N, slightly decreasing with increasing Ba ($\sim$ 230–185) K in agreement with recent theoretical work [260]. The achievement of ferrodistortive properties is attained with larger A-site ionic size average accomplished by the Ba^{2+}substitution (ionic size radius R = 1.61 Å for twelve-coordinated Ba) for Sr^{2+} (1.44 Å) [261]. Tiny variations of the material's cationic stoichiometry allows not only for enhanced ferroelectric properties but also controls coupling strength of the ferroelectric and magnetic order parameters.

5.4 Ferroelectricity in SBMO (x=0.43 – 0.45)

The paraelectric (cubic) to ferroelectric (tetragonal) structural transition line shown in Fig. 5.2 is relatively broad. While $Sr_{0.60}Ba_{0.40}MnO_3$ does not provide any evidence for long or short range tetragonal distortions, these distortions first appear with $x \sim 0.43$ and increase steeply in a very small Ba substitution range. The c/a ratio, corresponding to the degree of strain-induced tetragonality, increases to a maximum of 1.0051 and 1.006 at T $\sim$ 250 K for $Sr_{0.57}Ba_{0.43}MnO_3$ and $Sr_{0.56}Ba_{0.44}MnO_3$,

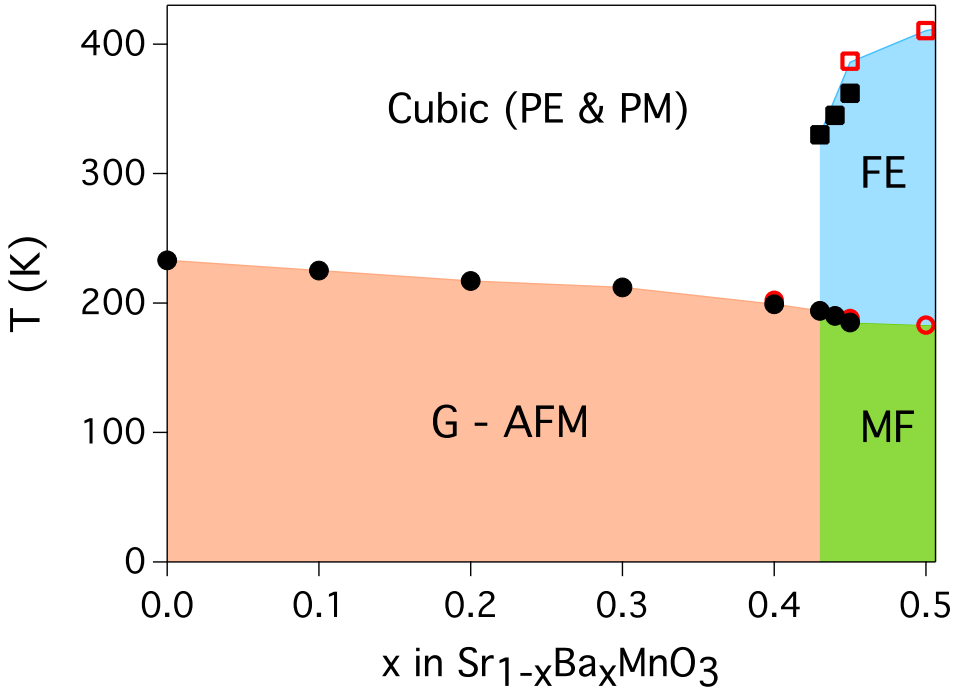

Figure 5.2: Phase diagram of structural, magnetic and ferroelectric properties as a function of Barium content (x) in the multiferroic $Sr_{1-x}Ba_xMnO_3$ system. PE, PM, FE, MF refer to paraelectric, paramagnetic, ferroelectric and multiferroic properties, respectively. Transitions to a G-type antiferromagnetic phase (G-AFM) are denoted by filled circles for the data taken from our current (this thesis) and previous work [124,262] and by the open circles from Sakai et al. [125]. Magnetic and ferroelectric ordering (MF region) coexist at x=0.43 and above.

respectively. Likewise, the tetragonal transition temperature T_C rises sharply from around room temperature for $Sr_{0.57}Ba_{0.43}MnO_3$ to about 362 K and 420 K for the x = 0.45 sample (this work) and x = 0.5 [125, 259], respectively.

At temperatures above T_C, the x = 0.43 - 0.45 samples crystallize in the common cubic $Pm\bar{3}m$ space group symmetry [54, 263] with consistent structural refinement reliability factors χ^2 and R_{wp} of about 2.8 and 5%, respectively. The cubic structure is best described as a three dimensional stack of regular corner-sharing MnO_6 octahedra with the exact center of the octahedral cavities occupied by Sr or Ba [26].

Progressive deterioration of the reliability factors below T_C (with χ^2 becoming as large as 25 at 300 K) is observed if one continues to impose the cubic symmetry as shown in Fig. 5.3 (x = 0.43 and 0.45 for time of flight neutron refinements) and Fig. 5.4 (x = 0.44 from synchrotron x-ray APS data).

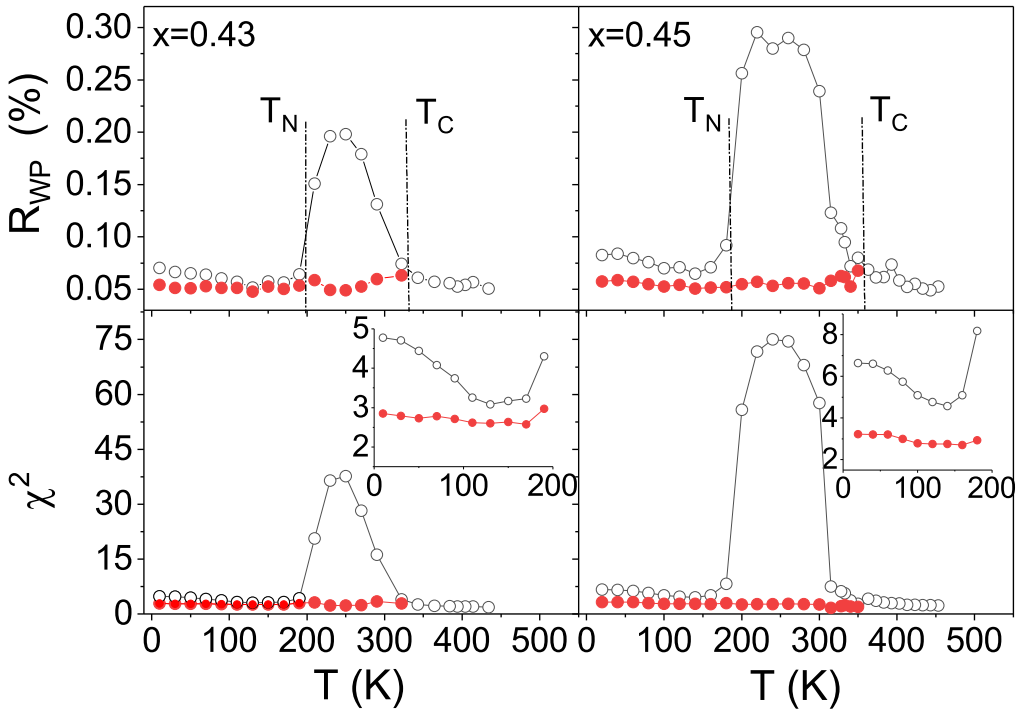

Figure 5.3: Left panels ($Sr_{0.57}Ba_{0.43}MnO_3$), right panels ($Sr_{0.55}Ba_{0.45}MnO_3$): Weighted profile residual agreement factor and the goodness of fit χ^2 obtained from time of flight neutron diffraction refinements using cubic $Pm\bar{3}m$ (open circles) and noncentrosymmetric tetragonal P4mm (filled circles). Significant improvements in the refinements are obtained below T_N when assuming the tetragonal polar symmetry.

This expected result signals the onset of a phase transition to a lower symmetry in agreement with the clear splitting of various characteristic peaks observed in both the neutron and x-ray diffraction patterns; see Fig. 5.5 for example. We define the ferroelectric Curie transition temperature T_C as the temperature of cubic

to tetragonal structural transition. Given the relative width of the ferroelectric transition, T_C is determined from the divergence of the Rietveld agreement factors obtained with fits performed using both the cubic and tetragonal models.

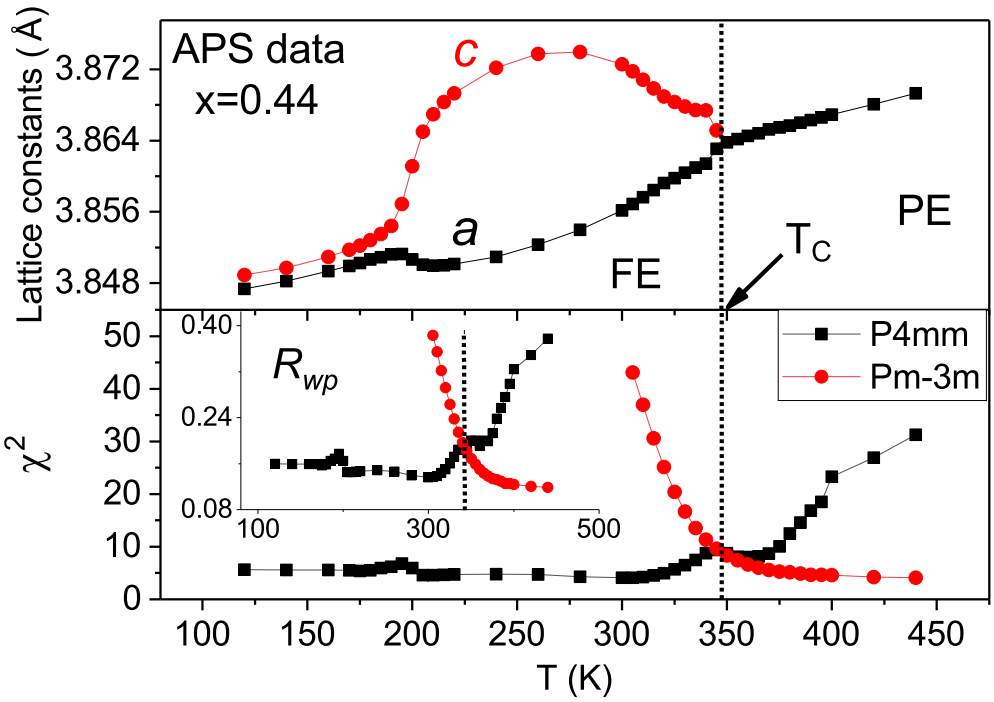

Figure 5.4: Top: Refined lattice constants of $Sr_{0.56}Ba_{0.44}MnO_3$ as obtained from APS high-resolution synchrotron x-ray diffraction refinements. Bottom: The ferroelectric Curie transition temperature T_C =345 K of cubic to tetragonal structural transition determined from the divergence of the Rietveld agreement factors. Significant improvements in the refinements are obtained below T_C when assuming the tetragonal polar symmetry.

While various possible polar structures have been observed and proposed for the ferroelectric $BaTiO_3$ analog [134, 264], my structural refinements together with previous work [125, 259, 262] indicate the stability of only one single tetragonal symmetry for SBMO persisting between the ferroelectric and magnetic transition temperatures. Due to favorable displacements of the manganese and oxygen ions

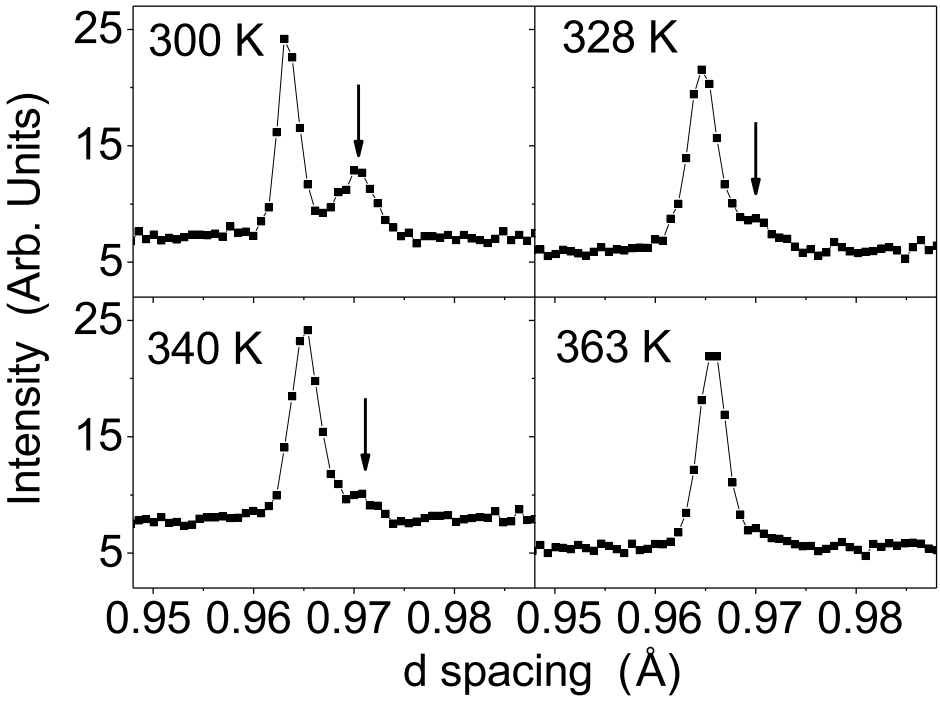

Figure 5.5: High temperature TOF NPD for $Sr_{0.55}Ba_{0.45}MnO_3$ at selected temperatures in the narrow d-spacing range of 0.95-0.98 Å showing the sustained splitting of the 400 peak in the ferroelectric region at room temperature and up to $T_C \sim 362$ K above which the structure becomes cubic paraelectric.

from their equilibrium positions, the tetragonal distortions of SBMO are best described using the noncentrosymmetric symmetry of the $P4mm$ space group [125], see Table 5.1 for atomic positions in this phase.

The displacement of the Mn ions away from their original central positions coupled with the concomitant displacement of the equatorial oxygen atoms in the opposite direction give rise to the tetragonal elongation of the c-axis and the associated ferroelectric order. This behavior is similar to the observed Ti and O opposite displacements in tetragonal $BaTiO_3$ at temperature range $\sim$ 280–400 K [263] as shown in Fig. 5.6. Displacements directions in $PbTiO_3$ lead to larger octahedral deforma-

Table 5.1: Structural parameters for noncentrosymmetric tetragonal ($P4mm$) in $Sr_{0.55}Ba_{0.45}MnO_3$ obtained from neutron diffraction refinements at 300 K. Lattice parameters a = 3.85393(4) Å, and c = 3.88053(2) Å. Residual agreement factors:χ^2 = 2.63 and R_{wp} = 5.10 %. X,Y and Z denote the fractional atomic coordinates.

Atom	Wyckoff Site	X	Y	Z
Sr/Ba	1a	0	0	0
Mn	1b	0.5	0.5	0.4923(9)
O1 Apical	1b	0.5	0.5	0.0103(9)
O2 Equatorial	2c	0.5	0	0.5111(7)

tion ($< O2 - Ti - O2 >$ angle buckling) and hence larger displacive character and electric polarization values as shown in Table 2.2 of chapter 2. In both modes, the equatorial oxygen atoms (O2) seem to always oppose the direction of B-site ion.

Time-of-flight neutron data collected at select temperatures are shown in Fig. 5.7 for the $Sr_{0.57}Ba_{0.43}MnO_3$ sample. Fig. 5.8 shows synchrotron x-ray powder diffraction data for the {200} reflection for the x=0.43 - 0.45 samples. In these samples, minute traces of the MnO impurity phase, with a refined weight fraction of no more than 0.5 – 0.6%, were observed (crosses) and successfully included in the refinements and final fits. Tetragonal splitting of characteristic peaks (e.g., [002] and [200] in Fig. 5.8) is observed in the diffraction patterns below T_C followed by the partial suppression of the tetragonal order below T_N and the appearance of new magnetic peaks (arrows in Fig. 5.7).

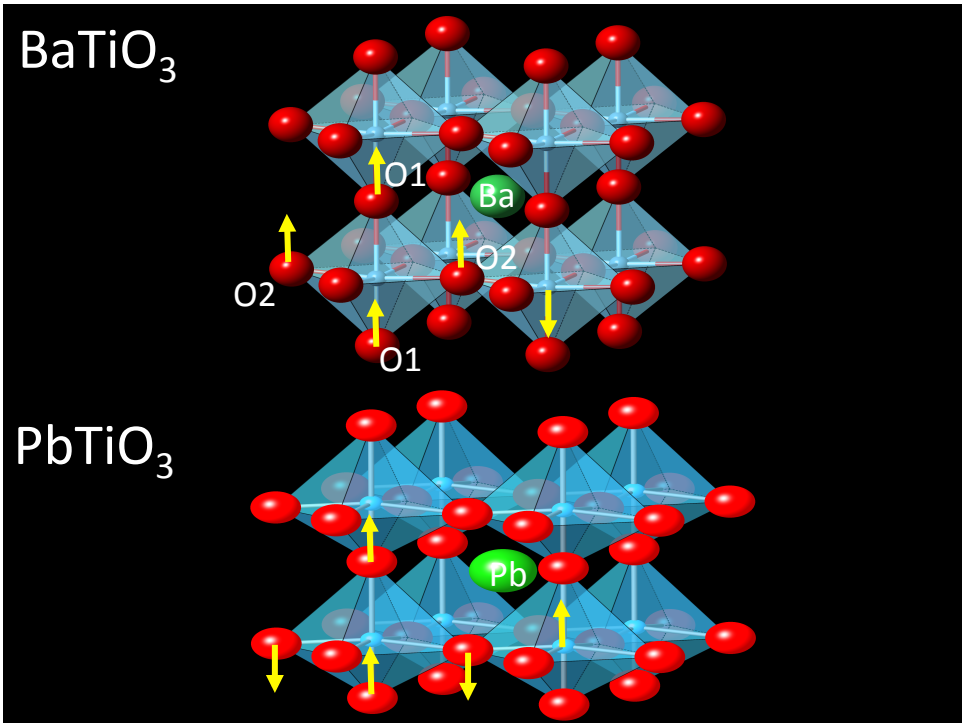

Figure 5.6: A view of the non-centrosymmetric P4mm unit cell where two distinct polar modes exist and lead to ferroelectric distortion. Arrows are attached to the arrangement of oxygen ions and Mn cations indicating the direction of ions displacements.

5.5 The coupling between strain-induced polar distortion and spin order in SBMO

As the temperature approaches the magnetic transition on cooling, the c/a ratio shown in Fig. 5.10 for x=0.43 collapses sharply to indicate the suppression of the tetragonal distortion with a possible return to the high temperature cubic symmetry. The complete or partial suppression of the tetragonal order can be determined by carefully examining the behavior of characteristic peaks below T_N. Indeed, while the tetragonal {400}, {311}, {220}, and {200} peaks are no longer split they remain

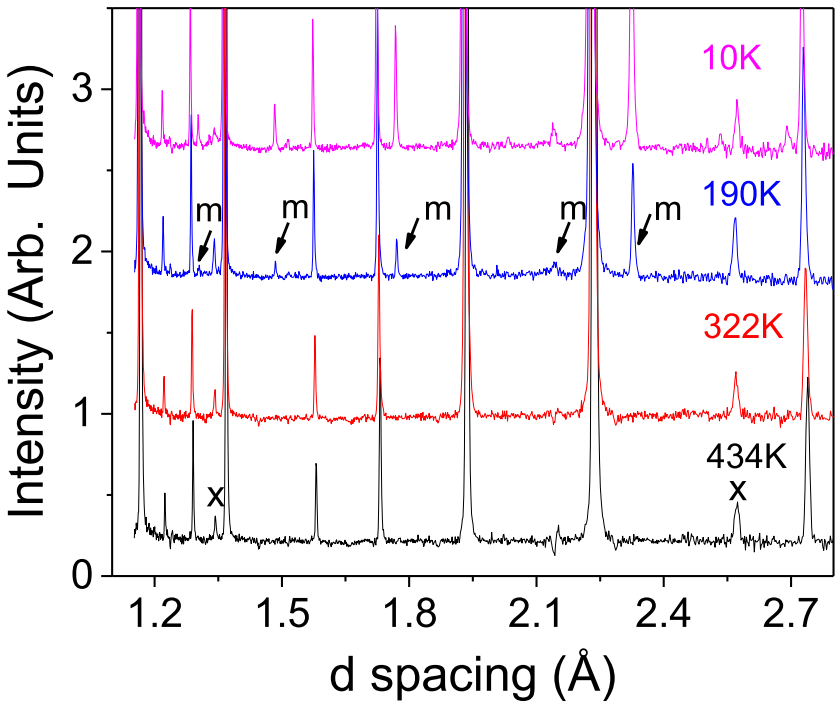

Figure 5.7: Time-of-flight neutron-diffraction patterns in a 1.6 Å wide d-spacing range showing reflections for $Sr_{0.57}Ba_{0.43}MnO_3$ at selected temperatures. Cross symbols correspond to small MnO impurity phase ($\sim 0.6\%$ by weight) while the arrows indicate the reflections that arise from the antiferromagnetic ordering below T_N.

significantly broader than their corresponding cubic peaks in the paraelectric region above T_C leading me to conclude that the tetragonal distortion is not fully suppressed. Additionally, significantly better agreement factors are obtained with the refinements performed assuming a continuous $P4mm$ symmetry below T_N instead of a return to the cubic symmetry, Fig. 5.3. Suppression of tetragonality c/a observed around T_N is clear manifestation of the strong coupling between magnetism and ferroelectricity (spin-lattice coupling) attributed to the systems's energy gain from spins exchange interaction which favors straight Mn-O-Mn angle in these materials.

The refined lattice parameters as a function of temperature are shown in Figs. 5.4, 5.10, and 5.11 for x= 0.44, 0.43, and 0.45, respectively. In all samples, the

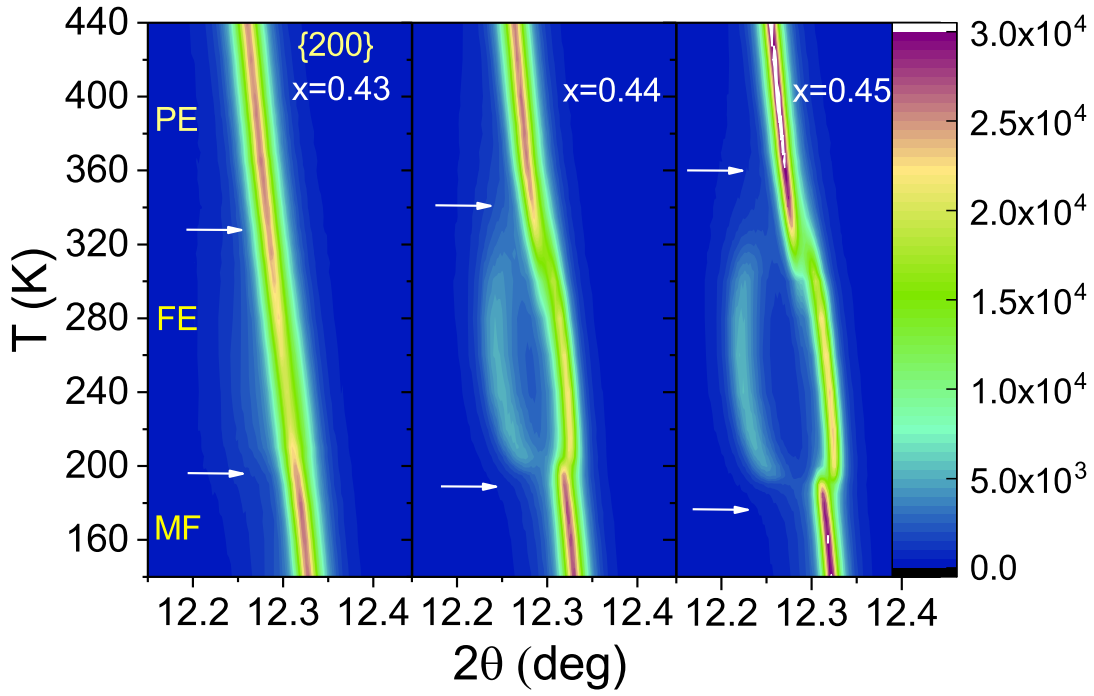

Figure 5.8: Contour maps of the cubic {200} reflection from synchrotron x-ray powder diffraction for the x = 0.43, 0.44 and 0.45 samples. The tetragonal splitting of the peak is observed at T_C (top arrows) which changes as a function of the Ba content. The splitting is partially suppressed below T_N (bottom arrows).

high temperature cubic lattice parameter "a" exhibits a slight thermal contraction on cooling, typical of similar oxides, as it approaches the ferroelectric transition temperature. The lattice distortion expressed as the ratio of lattice parameters c/a serves as an approximate measure for the ratio of the average apical Mn-O1 to equatorial Mn–O2 bond lengths [265] and hence can be directly related to the magnitude of the polarization [125]. There exists a relatively narrow region over which the lattice distortion (c/a ratio) increases rapidly to reach maximum values at T$\sim$ 260 K of $\sim 1.005, 1.006$, and 1.008 for x = 0.43, 0.44, and 0.45, respectively as shown in Fig. 5.11. larger tetragonal distortion is observed for $Sr_{0.55}Ba_{0.45}MnO_3$ compared to the consistently smaller distortion values in $Sr_{0.57}Ba_{0.43}MnO_3$ and

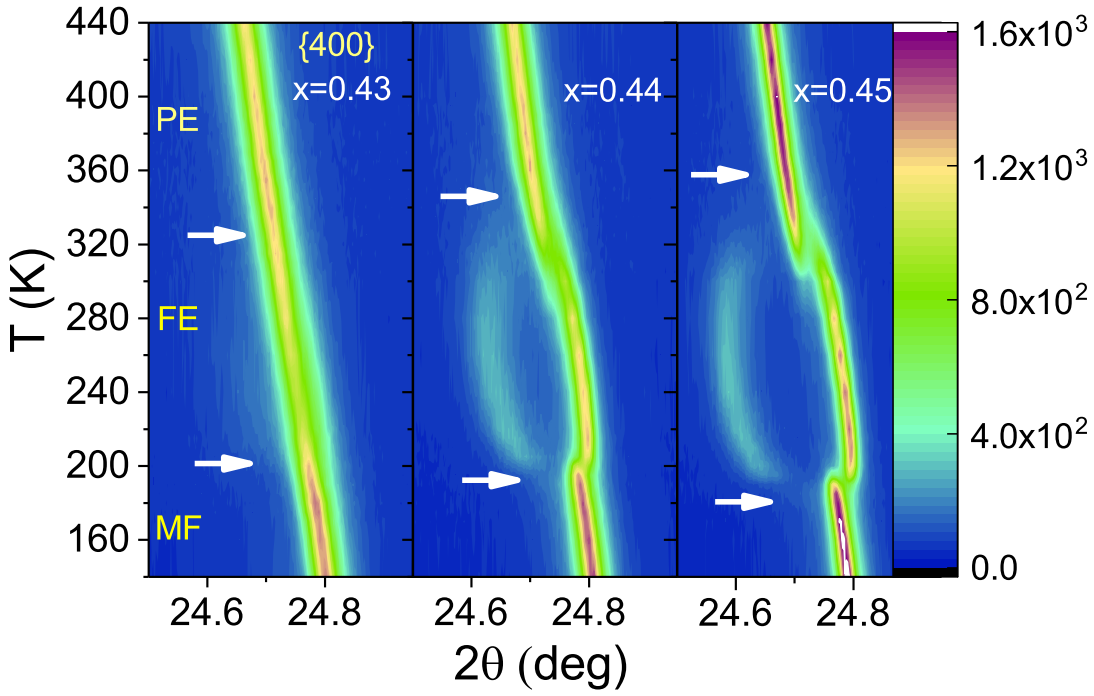

Figure 5.9: Contour maps of the cubic {400} reflection from synchrotron x-ray powder diffraction for the x = 0.43, 0.44 and 0.45 samples. The tetragonal splitting of the peak is observed at T_C (top arrows) which changes as a function of the Ba content. The splitting is partially suppressed below T_N (bottom arrows).

$Sr_{0.56}Ba_{0.44}MnO_3$ at all the measured temperatures. Lattice parameters range is well between the calculated relaxed values of a_0=3.806 [149] and 3.920 Å for $SrMnO_3$ and $BaMnO_3$,respectively [33].

The ferroelectric distortion below T_N is alleviated in various degrees by the magnetic ordering and consequently the *"c"* lattice parameter drops to values comparable to *"a"* as discussed above. However, when the temperature is further lowered, the strains increase again and the gap between the *a* and *c*-lattice parameters widens. This structural trend of the strains bears a strong resemblance to the temperature evolution of the soft mode phonon which is associated with ferroelectric ordering as observed in spectroscopic studies [257]. It has been found that the soft mode

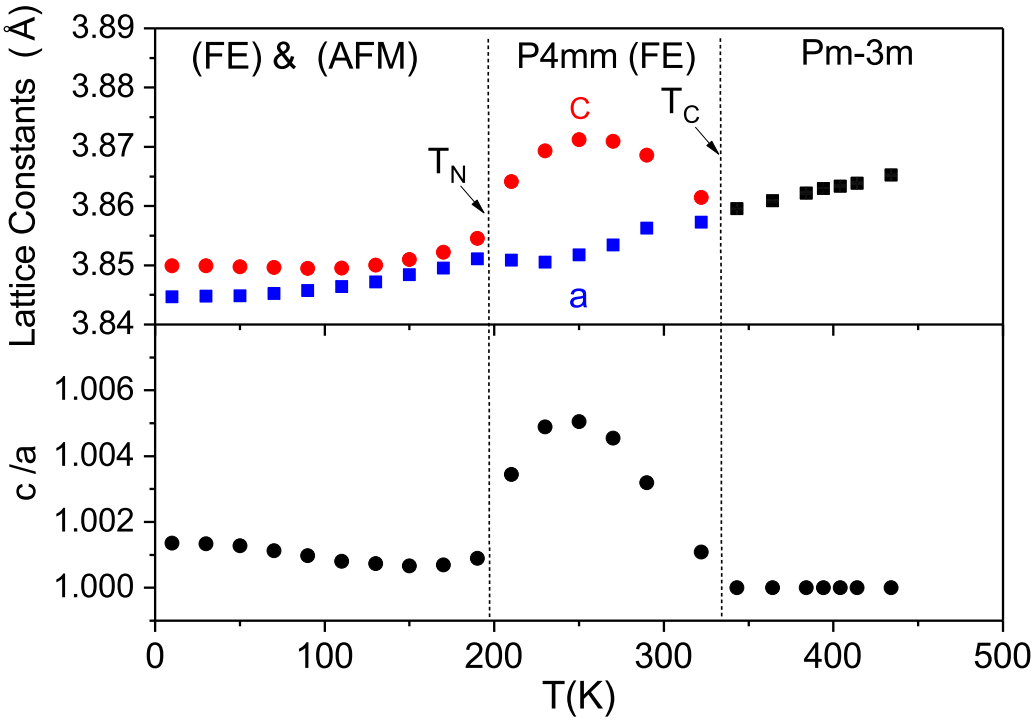

Figure 5.10: Top panel: Refined lattice parameters as a function of temperature for $Sr_{0.57}Ba_{0.43}MnO_3$. Error bars are smaller than the symbol size. Bottom panel: Tetragonal distortion in this material given as the ratio of lattice constants c/a, which equals unity in the cubic phase. . A maximum value of 1.0051 recorded in the FE region at ~ 250 K.

frequency sharply drops at the onset of magnetic transition but continues to harden at the lowest temperatures. Since the soft mode is a direct measure of polarization [266], this indicates a strong coupling between strains and polarization in our materials.

5.6 Characteristics of the Magnetic ordering

While the nuclear structure is noncentrosymmetric $P4mm$, the antiferromagnetic structure of the Mn sublattice is best described using the higher-symmetry of

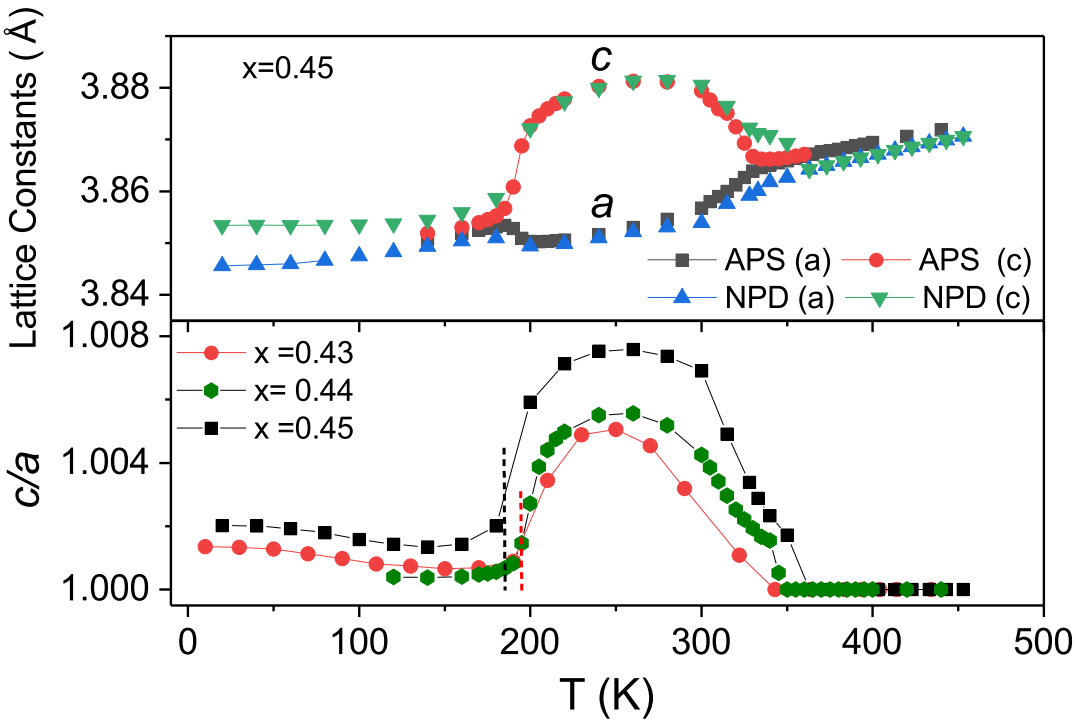

Figure 5.11: Top panel: Temperature evolution of the lattice parameters of $Sr_{0.55}Ba_{0.45}MnO_3$ determined from synchrotron x-ray (11-BM-B) and from TOF neutron diffraction data (POWGEN).Ferroelectric tetragonal distortions are drastically reduced upon approaching magnetic ordering below 195 K demonstrating the strong magnetoelastic coupling in this system. Bottom panel: Strain-induced tetragonal distortion shown as c/a ratios.

the centrosymmetric tetragonal $P4/mmm$ space group. Regardless of whether the material exhibits ferroelectric properties or not, magnetic ordering requires that the cubic structure distorts to become tetragonal below T_N in agreement with discussions made in the preceding paragraph. From a crystallographic perspective, the magnetic symmetry is described as $P4/m'm'm$ which is the result of taking the time reversal symmetry of the plane mirrors normal to the 4- and 2-fold symmetry axes along the [001] and [100]/[010] directions, respectively. Such spin arrangement results in a G-type AFM ordering where the direction of the magnetic moment of each Mn^{4+} ion is opposite to its six nearest neighbors as shown in Fig. 5.12. Also shown

in the same figure are select magnetic diffraction peaks for the x = 0.45 sample successfully modeled with the magnetic $P4/m'm'm$ symmetry.

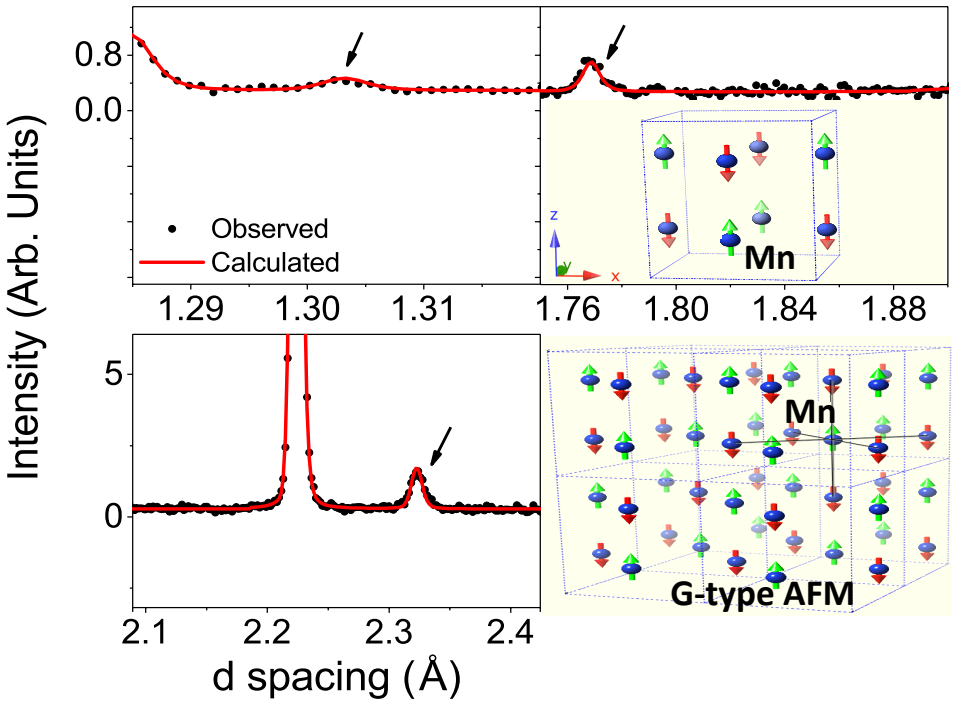

Figure 5.12: Select diffraction peaks (indicated by arrows) for the x = 0.45 sample arising from magnetic ordering on the Mn^{4+} sublattice at T = 40 K which were properly fit with the $P4/m'm'm$ magnetic space group symmetry. The inset shows the directions of energetically favored magnetic moments exhibiting a G-type AFM ordering in an extended cell view.

The refined magnetic moment as a function of temperature is presented in Fig. 5.13. We find that the temperature dependence of the magnetic moment (μ) can be well fit using a power-law function of the form: $\mu(T) = \mu_0 \left(1 - \frac{T}{T_N}\right)^{\alpha}$. The obtained values for T_N are in excellent agreement with those determined by Rietveld refinements and take the values of 194 and 185 K for the x = 0.43 and 0.45 samples, respectively. For both samples, the critical exponent (α) converges to 0.12– 0.13 which is comparable to the critical exponent value of 2D Ising materials ($\alpha = 1/8$).

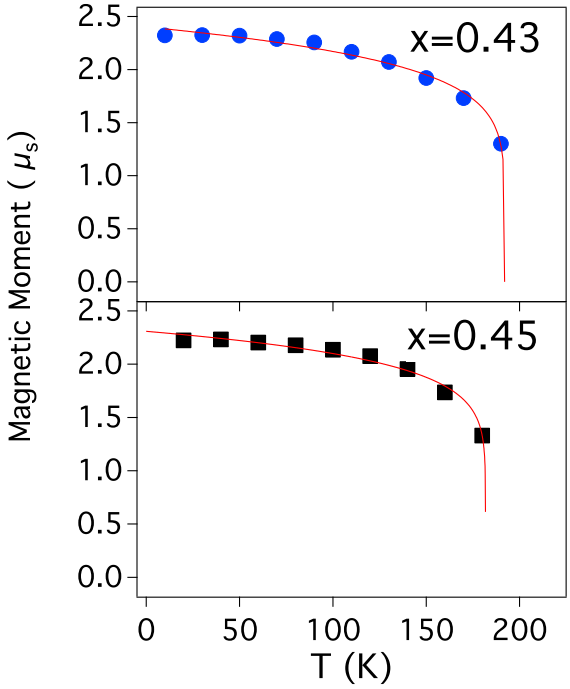

Figure 5.13: Refined magnetic moments obtained from time-of-flight neutron diffraction data. A power law was fit to the moments from which the obtained T_N values ($\mu_s = 0$) are in good agreement with values determined from the Rietveld refinements as described in the text and the magnetic measurements. Reduced moments from the expected 3 μ_B value is strong evidence for the finite bandwidth of 3d states and large covalency of Mn–O bonds that stabilize the *FE* phase [267].

5.7 Atomic displacements driven by polar instabilities

Figure 5.14 shows the refined atomic positions as a function of temperature for $Sr_{0.57}Ba_{0.43}MnO_3$ and $Sr_{0.55}Ba_{0.45}MnO_3$. As discussed above, our neutron refinement results demonstrate that the Mn and O ions in the ferroelectric regime displace in directions similar to that of the prototypal ferroelectric $BaTiO_3$ [264] with the Mn atoms shifting along the $-z$ direction while the oxygen atoms (O1 and O2) displace independently along the $+z$ direction. We also demonstrate a strong

influence/coupling of the magnetic ordering to ferroelectricity manifested by the partial to near complete suppression of these displacements below T_N. Therefore, we experimentally confirm here the recent ab intio predictions of magnetic ordering partial suppressing of ferroelectricity by reducing the ionic displacements in $AMnO_3$ system [267, 268].

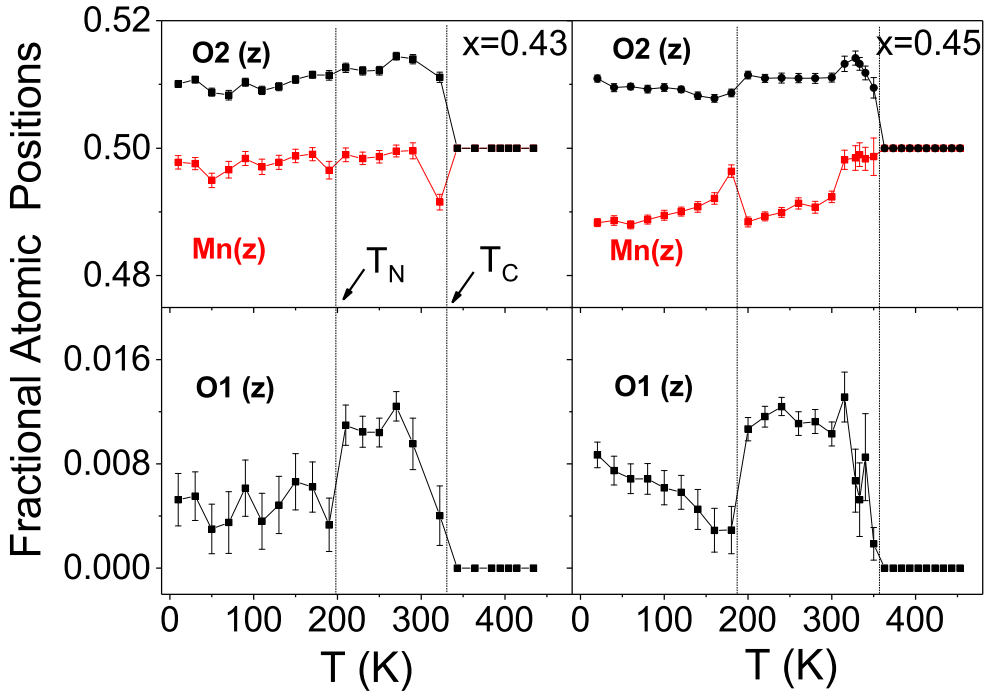

Figure 5.14: Fractional z-coordinates as a function of temperature for Mn and O refined using neutron powder TOF diffraction data for $Sr_{0.57}Ba_{0.43}MnO_3$ (left panels) and $Sr_{0.55}Ba_{0.45}MnO_3$ (right panels). Displacements of the apical (O1) and planar/equatorial (O2) oxygen atoms as well as the Mn atoms are all along the c-axis direction with z Wyckoff sites given as $(0+u), (+v), and (-w)$, respectively.

5.8 Calculation of electric polarization from measured bond lengths and angles

In a centrosymmetric MnO_6 octahedral cage, the two apical (along the c axis) bond lengths [Mn–O_1] are equal in magnitude and the same can be said about the other four planar (in the ab-plane) [Mn–O_2] bond lengths leading to a zero-sum electric dipole. On the other hand, in the $P4mm$ phase, our neutron refinements show that the octahedra deform into three distinct bond lengths whose temperature evolution is shown in Fig. 5.15. A pronounced distortion is observed for the apical bond length Mn–O_1 due to the Mn displacement along the c axis towards one of the two apical oxygen ions to form a strong covalent bond. Consequently, this creates alternating long and short Mn–O_1 bonds along the c-axis with the short bond being comparable with the equilibrium Mn–O bond length ($\sim$ 1.897 Å [269]). Conversely, the uniformly spaced medium-length Mn–O_2 shows a smooth thermal compression as T decreases across the different phase boundaries. The lowest octahedral distortion is recorded at temperatures near the magnetic ordering transition (T_N) for both samples.

In the paraelectric region (above T_C), the atomic special positions are all fixed by the high symmetry structure resulting in zero polarization. Because of the atomic displacement below T_C, the $< O_2–Mn–O_2 >$ bond angle buckles to values less than the ideal 180° while the apical $< O_1–Mn–O_1 >$ angle remains straight at all temperatures as shown in Fig. 5.16. The length difference between the two apical bonds [Mn–O_1] leads to a net electric dipole in the $-z$ direction. Likewise, the four equidistant equatorial bonds [Mn-O_2] produce a net dipole moment canceling out in the ab-plane but with a vertical component in the same direction as the apical

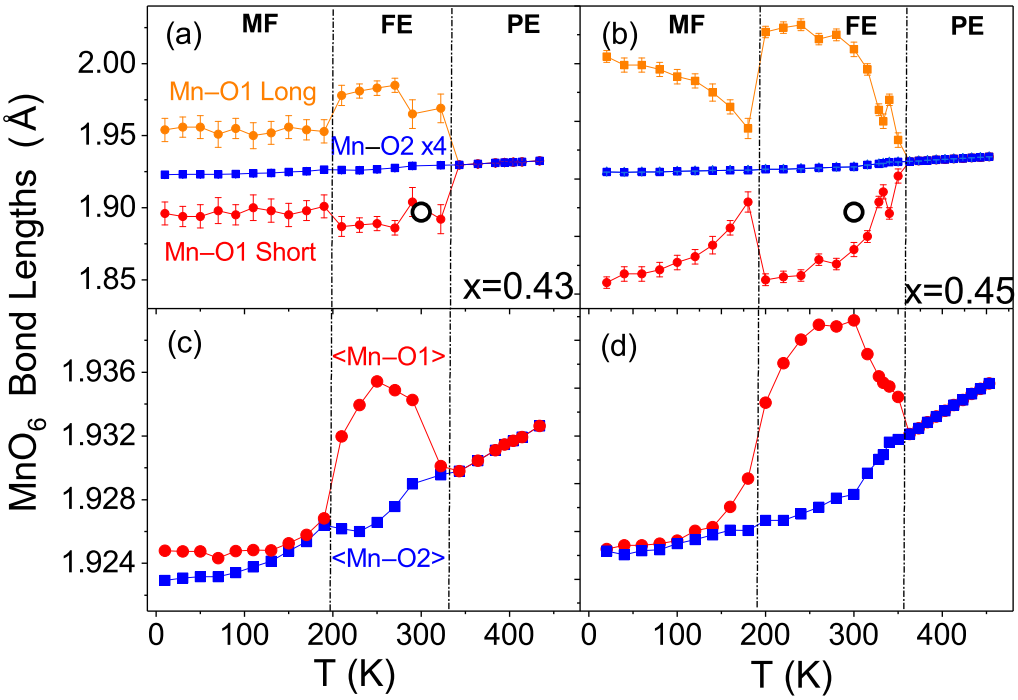

Figure 5.15: Detailed temperature evolution of the Mn-O bond lengths in MnO_6 octahedra for both the x = 0.43 and 0.45 materials. The [Mn–O_1] apical bonds distortion is greatly reduced below T_N. Dotted vertical lines correspond to the ferroelectric and magnetic transitions of the materials. Mn^{4+} ions shift towards one of the apical oxygen atoms in order to retain an equilibrium interatomic Mn–O distance ($\sim$ 1.897 Å) [269]shown as open circles.

bonds dipole. Thus, the net electric dipole of the MnO_6 octahedron with a non-zero component in the $-z$ axis can be directly computed from the refined structure, see Fig. 5.16 (in units of C. m) as:

$$|\mathbf{P}| = q\left\{\Delta\left[Mn\text{–}O_1\right] + \left(4 \times \left[Mn\text{–}O_2\right] \times \sin\frac{180 - < Mn\text{–}O_2\text{–}Mn >}{2}\right)\right\} \quad (5.1)$$

Where q = 1.95 e, is the electronegativity difference between Mn^{4+} and O^{2-} ions times the electron charge. It then follows from the expression above that the polarization is expected to be quite sensitive to the magnitude of the bond angle which on the other hand influences the superexchange interactions. The maximum net spontaneous polarization is calculated as $P_s = 18.4\ \mu C/cm^2$ and $29.5\ \mu C/cm^2$ for the x = 0.43 and 0.45 samples, respectively. It is worth noting the large polarization achieved in this system and how similar it is to that of the $BaTiO_3$ benchmark ferroelectrics.

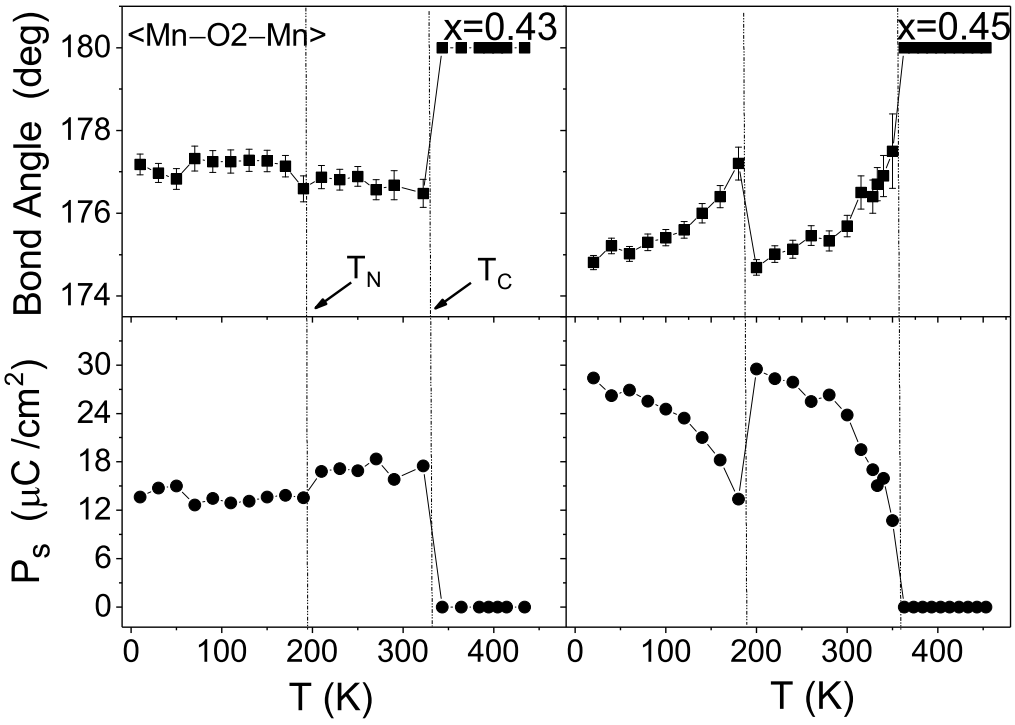

Figure 5.16: Top Panels: Measured $< Mn–O_2–Mn >$ bond angle as a function of temperature. Below T_N, the bond angle in $Sr_{0.57}Ba_{0.43}MnO_3$ (left panel) is essentially constant with an average value of $\sim 177°$ while in $Sr_{0.55}Ba_{0.45}MnO_3$ it exhibits a wider range of values. Bottom panels: Spontaneous polarization P_s calculated from the measured bond lengths and bond angles. P_s is very sensitive to the magnitude and variations of the bond angle.

Our previous studies on (Sr, Ca, Ba)MnO_3 manganites [124, 177, 269] have allowed us to estimate relaxed interatomic distances at room temperature as [Sr^{2+}– O] = 2.691 ± 0.002 Å, [Ba^{2+}– O] = 2.783± 0.004 Å, and [Mn^{4+}– O] = 1.897 ± 0.002 Å. By comparing these equilibrium values to the measured bond lengths in the present study we have found that despite being highly strained due to the presence of Ba, the measured $< A\text{–}O >$ bond length is ∼ 2.731(2) Å for both the compositions x = 0.43 and 0.45 in the *FE* region showing a negligible deviation from the equilibrium value (percent error ∼ 0.03%). On the other hand, the MnO_6 octahedra are most sensitive to the Ba substitution and the $< Mn\text{–}O >$ bond length for both the x = 0.43 and 0.45 samples is significantly stretched beyond its equilibrium value.

5.9 Variation of ferroic transitions (T_N, T_C) with Ba content

Fig. 5.17 shows the evolution of the lattice parameters and Néel temperature T_N as a function of the Ba content. Unlike some perovskite manganites which exhibit AFM ordering at low T such as found in $DyMnO_3$ with T_N ∼ 10 K as described in Ref. [270], AFM ordering occurs in SBMO materials for the Mn^{4+} at relatively high T_N ∼ 180 – 233 K.

Previous arguments have been made for the strong correlation between the magnetic ordering temperatures and the average $< Mn\text{–}O\text{–}Mn >$ bond angle (θ) which suggested that the orbtial overlap integral which modulates the exchange itneractions is reduced for θ <180° [260, 269, 271]. While a linear relationship between T_N and $\cos^2\theta$ is well established for the rare earth manganites $RMnO_3$ [269, 271],

one can see from Fig. 5.17 that T_N in the SBMO series is clearly a decreasing function of the Ba content even in the cubic regime (with 180° Mn–O–Mn bond angles). As shown in previous work [124], this observed decrease from $T_{N(max)}$ = 233 K for the parent $SrMnO_3$ cannot be explained by solely considering the bond angle. Using an empirically established relationship which takes into account the magnetic interactions sensitivity to local distortions and instabilities [269](i.e. the size variance of the A-site ions or σ^2 [272]), the calculated $T_N(\theta, \sigma^2)$ is compared to the measured value in Fig. 5.15 as a function of the average size of the A-site cations $< r_A >$ which scales linearly with the Ba substitution. The average size progressively increases with Ba doping and can be expressed for the SBMO system as $< r_A >= (1-x)r_{Sr} + (x)r_{Ba}$ where r_i are the ionic sizes [261]. The difference between the measured and calculated T_N values is less than 1 K for $Sr_{0.57}Ba_{0.43}MnO_3$.

The ferroelectric transition T_C is greatly enhanced from a value that is around room temperature for the x = 0.43 sample to 400 K for Ba = 0.50. It has been suggested [273] that this enhancement could be a result of difference between apical and equatorial Mn-O bond lengths.

In SBMO materials, it is interesting to notice that while the Ba substitution has definitely led to larger expansion of the unit cell (see Fig. 5.18 for the Room temperature unit cell volume of the full $AMnO_3$ system [A= Ca, Sr, Ba (up to 0.5)], the oxygen and Mn atoms shift collectively in such a way that the overly stretched average $< Mn–O >$ bond length for both samples maintain a nearly constant length difference of no more than $\sim$ 0.002 Å at all the examined temperatures between 450 – 10 K. The marked difference in T_C is attributed to the difference in apical bonds as the in-plane Mn–O_2 bonds in both samples are nearly the same as shown in Fig. 5.15. Engineering epitaxially strained thin films, which play a role similar to Ba substitution in their bulk counterparts, has been widely used for the purpose of

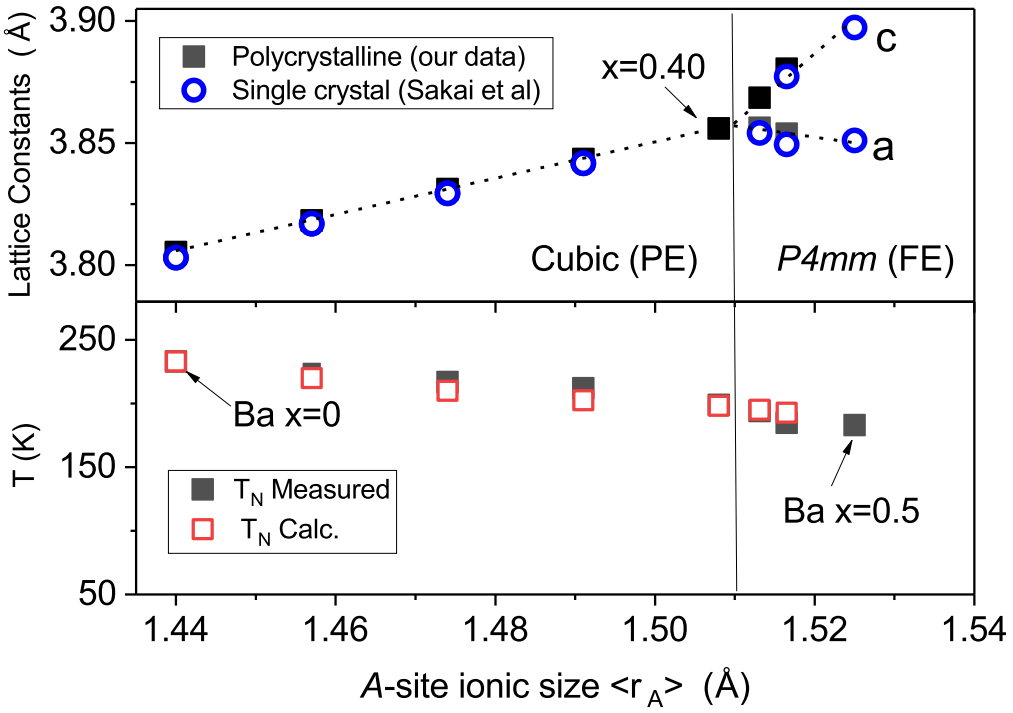

Figure 5.17: Top panel: Room temperature lattice constants of the SBMO materials where the FE tetragonal $P4mm$ distortion is first observed at x = 0.43. Tetragonal distortion (c/a) (not shown) increases progressively from this composition on. Dotted line is a guide to the eye. Bottom panel: Continuously decreasing magnetic transitions T_N from their maximum value of 233 K for Ba-free $SrMnO_3$. Measured T_N transitions compared to values calculated using an expression that takes into account the influence of bond angle buckling and A-site ionic size variance as described in this dissertation and in reference [124].

inducing or enhancing ferroelectricity, in general, and for tuning both the T_C and the coupling strength of the order parameters, in particular [33, 144, 145, 274].

Room temperature pseudocubic unit cell volume of the $AMnO_3$ system [A= Ca, Sr, Ba (up to 0.5)] trending steadily upward as function of A-site ionic size. Shaded blue region corresponds to multiferroic materials with Ba x = 0.43–0.5 where the ferroelectric distortion first appears at $< r_A > \sim$ 1.51 Å and volume $\sim$ 57.5 Å^3. Data obtained from this dissertation as well as other Refs. [124, 125]. which equivalently

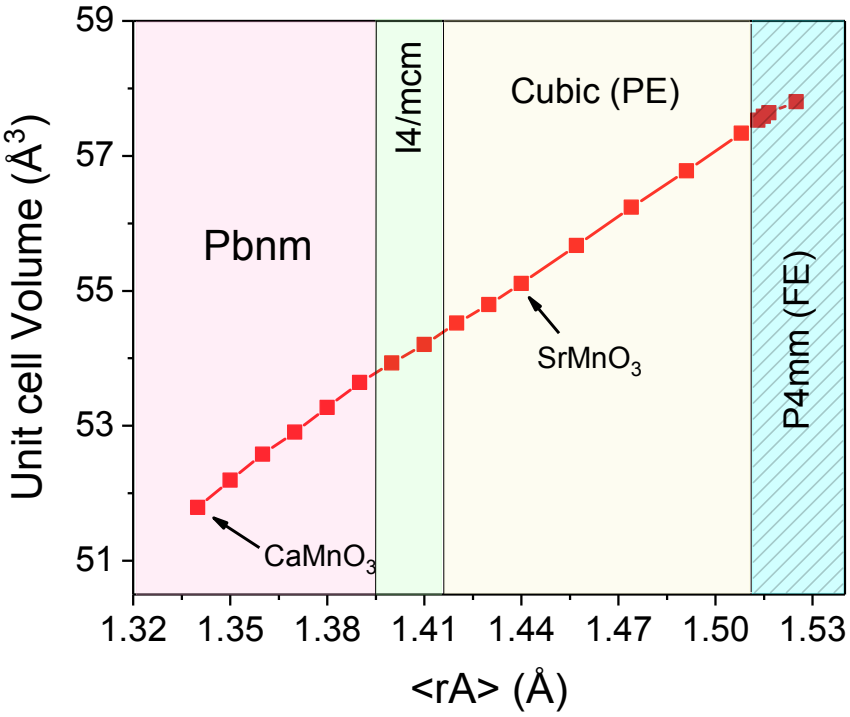

Figure 5.18: Top Panels: Measured $< Mn–O_2–Mn >$ bond angle as a function of temperature. Below T_N, the bond angle in $Sr_{0.57}Ba_{0.43}MnO_3$ (left panel) is essentially constant with an average value of $\sim 177^\circ$ while in $Sr_{0.55}Ba_{0.45}MnO_3$ it exhibits a wider range of values. Bottom panels: Spontaneous polarization P_s calculated from the measured bond lengths and bond angles. P_s is very sensitive to the magnitude and variations of the bond angle.

indicate linear increase with the Ba substitution. At unit cell volume value of ~ 57.5 Å^3 , the structure becomes noncentrosymmetric tetragonal. *FE* instabilities is strongly sensitive to volume [33].

5.10 Discussion and Conclusion

I have investigated the development of spontaneous polarization due to strain-induced displacements in $Sr_{1-x}Ba_xMnO_3$. This effect arises from the opposite dis-

placements of manganese and the surrounding oxygen anions in response to large strains. Quantifying these displacements is critical for understanding the nature of the ferroelectric order. Neutron powder diffraction is of special importance for this work because of its effectiveness in accurately determining the atomic positions of the light oxygen anions. This is particularly the case when considering the coexistence of magnetism and ferroelectricity. The x = 0.43 and 0.45 compositions which are clearly ferrodistortive above T_N are partially suppressed at the onset of magnetic ordering. Below T_N, the energetically favorable ferroelectric distortions are likely suppressed by the gain in energy from maintaining a straight bond angle as close to 180° as possible. The ferroelectric suppression is evidenced by the reduction of the tetragonal order as the c/a ratio drops by $\sim$ 40, 47, and 55 % of its maximum value for the x = 0.43, 0.44, and 0.45, respectively. This behavior is similar to that observed in Sakai et al.'s SBMO single crystal with a Ba content of 45 % [125].

One possible way to characterize the appearance of ferroelectric ordering in SBMO system is to establish a strain parameter based on the optimal length of the Mn-O bond length. We have previously studied the phase diagram of the (Sr-Ca-Ba)MnO_3 system from which the individual relaxed bond lengths were determined. As the Ca substitution (y) in $Ca_{1-y}Sr_yMnO_3$ increases to 0.8, the structure at room temperature becomes cubic. This critical value can be considered to define the equilibrium room temperature Mn^{4+}- O bond length = 1.897 ± 0.002 Å in the cubic perovskite manganite system. Additional substitution of larger cations at the Ca/Sr site is certain to induce strains in a cubic symmetry. As I emphasized the importance of perovskite flexible structure in chapter 1, the cubic structure in $Sr_{1-x}Ba_xMnO_3$ accommodates the larger-size ions by stretching the Mn-O bonds to beyond their equilibrium limits with all compositions with $x < 0.43$. However, as

shown here for x = 0.43 and beyond, the structure must relieve the strains by the sudden displacements of the Mn and oxygen atoms.

The electric polarization is sensitive to small changes in the atomic positions [122] and it has been proposed [125, 268] that ferroelectricity in SBMO materials results in a spontaneous electric polarization which can be calculated from the ionic displacements with maximum values comparable to the prototypal $BaTiO_3$ (27 $\mu C/cm^2$ [266]). For instance, Sakai et al.'s single crystal with x = 0.50, a value of P_s ~14 $\mu C/cm^2$ just below T_N is predicted from the thermal evolution of the tetragonal distortion ($(1 - c/a) \sim P_s^2$) to reach a maximum of 25 $\mu C/cm^2$ in the FE region [125]. Indeed, from the measured bond lengths and bond angles we have calculated maximum P_s values of 18.4 and 29.5 $\mu C/cm^2$ with a sharp drop below T_N to 13.6 and 13.4 $\mu C/cm^2$ for $Sr_{0.57}Ba_{0.43}MnO_3$ and $Sr_{0.55}Ba_{0.45}MnO_3$, respectively.

The larger spontaneous polarization in $Sr_{0.55}Ba_{0.45}MnO_3$ as compared to $Sr_{0.57}Ba_{0.43}MnO_3$ is a result of consistently larger structural distortions as quantified by the (c/a) ratio for the former across different T regions as shown in Fig. 5.11. It is well-known that ferroelectric materials with higher Curie temperature possess larger values of polarization [117] which is also the case in our materials in agreement with previous first-principles [255] and ab initio calculations [267] predicting large P_s values in $Sr_{1-x}Ba_xMnO_3$ of 12.8 $\mu C/cm^2$ and 17 $\mu C/cm^2$ for $BaMnO_3$ (x = 1) and paramagnetic $Sr_{0.50}Ba_{0.50}MnO_3$, respectively. The possibility of smaller P_s values is rather unlikely for a system such as SBMO in its ferroelectric state which microscopically shares the same underlying mechanism of ferroelectricity as in $BaTiO_3$. On the other hand, improper ferroelectrics are known to exhibit small polarization values [[129]] as in the hexagonal $YMnO_3$ in which ferroelectricity is geometrically induced with a P_s of ~ 6 $\mu C/cm^2$ [133]. Larger tetragonal distortions c/a is the culprit for obtaining high spontaneous polarization. While our materials

have reached a maximum of ~ 1.008 for x=0.45 (P_S =29.5 C/cm^2), higher c/a values ~ 1.016 obtained for instance in epitaxially strained $BiFeO_3$ resulted in P_S of 50–60 μC/cm^2 [117].

Tensile strains were found to favor polar distortions in Ba-doped $SrMnO_3$ by reducing the energy gap and the simultaneous promotion of strong covalent Mn–O bonding [33, 255]. Equivalent strain effects due to increased Ba doping from $Sr_{0.57}Ba_{0.43}MnO_3$ to $Sr_{0.55}Ba_{0.45}MnO_3$ not only lead to expanding the stability range of the ferroelectric phase with a higher transition temperature, T_C, but also to decreasing on-site Coulomb repulsion U [275, 276] in agreement with the reduced refined magnetic moments of the Mn^{4+} ions from their expected $3\mu_B$ value ($t_{2g}^3, S = 3/2$) [267]. The calculated moments of the parent compound $SrMnO_3$ are $2.47\mu_B$ from a DFT study [276] and 2.7 μ_B from first-principles calculations [254] both of which are in agreement with the experimentally determined value of $2.6 \pm 0.2\mu_B$ [277]. Similar moment values were reported for SBMO system with 10% Ba substitution where the experimentally refined moment yielded 2.4 μ_B at the lowest measured temperatures [124] whereas moments of 2.6 μ_B [268] and 2.75–2.53μ_B [267] have been estimated for Ba =50% composition by ab initio calculations.

Negative chemical pressure (tension), which increases the cell volume through doping with larger ionic size such as Ba substitution for Sr, has a varying degree of influence on the crystal structure of manganite materials [275]. This effect could range from complete suppression of the antiferrodistortive transitions (rotations of oxygen in MnO_3 octahedra) as found in Ba-doped $La_{0.5}Sr_{0.5}MnO_3$ system [273] to the extreme case observed here where it favors the competing ferrodistortive ordering and Mn^{4+} ions are displaced off the octahedra centers .

CHAPTER 6

FUTURE WORK

We have seen in the preceding chapters a clear demonstration of the diverse and highly tunable properties exhibited by two classes of perovskite materials (namely, the titanates and manganites) as they distort from their simple cubic structure.

Transition metal oxides crystallizing in the perovskite-type structure have been and will remain at the center of focus in the field of condensed matter physics, both theoretically and experimentally. Thermoelectricity continues to gain a lot of interest with the ever-increasing demand for efficient energy resources. Titanate materials examined in chapter 4 clearly reveal promising n-type thermoelectric properties but significant (possible) improvements are still needed. As we saw from the measurements of electrical conduction, the conductivity is an integral part of the power factor PF and its magnitude will determine to a large degree the resultant figure of merit ZT. While we have succeeded in reducing thermal conductivity by an order of magnitude from the parent compound $SrTiO_3$, the 400 K figure of merit $ZT \sim 0.07$ indicates that more work remain needed to allow these materials to compete with other functional and well-established TE semiconductors. One possible way of improving ZT is to enhance conduction in high quality single crystals of these materials by eliminating grain boundaries resistivity and other polycrystalline-related effects. It is also as important to understand the underlying physics of transport properties by developing a full theory of the Seebeck coefficient in the temperature range below Heikes's entropy limit. Calculations of the effective mass using methods such as DFT will provide valuable insight into the nature of transition metal 3d bands and

how its degeneracy affects the material's thermopower. It would be interesting to examine the changes in TE coefficients (i.e., $S, \sigma, and\ \kappa$) at high enough temperature around 800-1000 K where S is expected to reach maximum values as predicted by Heikes and κ_L is often known to progressively decrease in oxides as the Umklapp phonon scattering becomes prominent.

The discovery of the best TE properties in $SrTiO_3$-based materials in the n-type B-site substituted $SrTi_{0.80}Nb_{0.20}O_3$, along with the good TE properties that we have established in this study for the A-site doubly substituted $(Sr_{1-x-y}Ca_xNd_y)TiO_3$ leads us to believe that combining the best of both worlds by simultaneously doping at the A and B-sites should result in better ZT values thus providing a wide avenue for further investigations.

Multiferroicity in manganites is a fascinating subject on its own. While single crystals and thin films are allowing researchers to establish and stabilize multiferroic properties in a non-equilibrium phase space, it is extremely desirable to synthesize and extend the solubility range of multiferroic materials in the polycrystalline form beyond the limitations of standard ceramic synthesis conditions.

We succeeded in stabilizing the perovskite structure in polycrystalline $Sr_{1-x}Ba_xMnO_3$ with ferroelectric properties that rival those of the prototypal FE $BaTiO_3$ system. Future work on this system could involve continuing the process of realizing compositions with higher Ba levels and varying the structure by doping the A-site with yet larger cations necessary to promote strains and to enhance the ferroelectric properties. Structural, magnetic and multiferroic effects achieved by substitutions at the B-site should also be explored, (AA')(BB')O_3, but in dilute amounts such that the superexchange interactions between magnetic ions in the neighboring BO_6 octahedra are not compromised. Our work revealed that the both

the structural and magnetic transition temperatures are very sensitive to the strain-induced tetragonal distortions.

REFERENCES

[1] R. J. D. Tilley, Perovskites: structure-property relationships (John Wiley Sons, 2016).

[2] T. Wolfram and S. Ellialtioglu, Electronic and optical properties of d-band perovskites (Cambridge University Press, 2006).

[3] H. Dekura, T. Tsuchiya, and J. Tsuchiya, Phys. Rev. Lett. 110, 025904 (2013).

[4] R. Van der Hilst, S. Widiyantoro, and E. Engdahl, Nature 386, 578 (1997).

[5] G. Popov, M. Greenblatt, and M. Croft, Physical Review B 67, 024406 (2003).

[6] P. V. Arribi, P. García-Fernández, J. Junquera, and V. Pardo, Physical Review B 94, 035124 (2016).

[7] J. Yu, A. Freeman, and J.-H. Xu, Phys. Rev. Lett. 58, 1035 (1987).

[8] U. Chon, H. M. Jang, M. Kim, and C. Chang, Phys. Rev. Lett. 89, 087601 (2002).

[9] R. Angel, J. Zhao, and N. Ross, Phys. Rev. Lett. 95, 025503 (2005).

[10] G. Samara, T. Sakudo, and K. Yoshimitsu, Phys. Rev. Lett. 35, 1767 (1975).

[11] I. A. Kornev, L. Bellaiche, P. Bouvier, P.-E. Janolin, B. Dkhil, and J. Kreisel, Phys. Rev. Lett. 95, 196804 (2005).

[12] I. C. Infante et al., Phys. Rev. Lett. 105, 057601 (2010).

[13] J. H. Lee and K. M. Rabe, Phys. Rev. Lett. 107, 067601 (2011).

[14] T. Tohei, A. Kuwabara, T. Yamamoto, F. Oba, and I. Tanaka, Phys. Rev. Lett. 94, 035502 (2005).

[15] G. Shirane, Rev. Mod. Phys. 46, 437 (1974).

[16] E. Pavarini and E. Koch, Phys. Rev. Lett. 104, 086402 (2010).

[17] A. Ishikawa, J. Nohara, and S. Sugai, Phys. Rev. Lett. 93, 136401 (2004).

[18] M. W. Lufaso and P. M. Woodward, Acta Crystallographica Section B: Structural Science 60, 10 (2004).

[19] A. Tagantsev et al., Nature communications 4, ncomms3229 (2013).

[20] N. A. Benedek and C. J. Fennie, Phys. Rev. Lett. 106, 107204 (2011).

[21] E. H. Mountstevens, S. A. Redfern, and J. P. Attfield, Physical Review B 71, 220102 (2005).

[22] L. Suescun, O. Chmaissem, J. Mais, B. Dabrowski, and J. D. Jorgensen, Journal of Solid State Chemistry 180, 1698 (2007).

[23] M. Borowski, Perovskites: structure, properties, and uses (Nova Science Publishers, 2010).

[24] R. D. t. Shannon, Acta Crystallographica Section A: Crystal Physics, Diffraction, Theoretical and General Crystallography 32, 751 (1976).

[25] S. Maekawa, T. Tohyama, S. E. Barnes, S. Ishihara, W. Koshibae, and G. Khaliullin, Physics of transition metal oxides (Springer Science Business Media, 2013), Vol. 144.

[26] J. S. Zhou and J. B. Goodenough, Phys. Rev. Lett. 94, 065501 (2005).

[27] M. Yashima and R. Ali, Solid State Ionics 180, 120 (2009).

[28] A. E. Smith, A. W. Sleight, and M. Subramanian, Mater. Res. Bull. 46, 1 (2011).

[29] J. Hemberger et al., Phys. Rev. Lett. 91, 066403 (2003).

[30] K. F. Garrity, Physical Review B 94, 045122 (2016).

[31] T. Wolfram, Phys. Rev. Lett. 29, 1383 (1972).

[32] W. A. Harrison, Electronic structure and the properties of solids: the physics of the chemical bond (Courier Corporation, 2012).

[33] S. Bhattacharjee, E. Bousquet, and P. Ghosez, Phys. Rev. Lett. 102, 117602 (2009).

[34] T. Okuda, K. Nakanishi, S. Miyasaka, and Y. Tokura, Physical Review B 63, 113104 (2001).

[35] S. L. Cooper, T. Egami, J. B. Goodenough, J. S. Zhou, and J. B. Goodenough, Localized to itinerant electronic transition in perovskite oxides (Springer, 2003), Vol. 98

[36] I. Inoue, O. Goto, H. Makino, N. Hussey, and M. Ishikawa, Physical Review B 58, 4372 (1998).

[37] A. Sundaresan, P. Paulose, R. Mallik, and E. Sampathkumaran, Physical Review B 57, 2690 (1998).

[38] S. Ohta, T. Nomura, H. Ohta, M. Hirano, H. Hosono, and K. Koumoto, Appl. Phys. Lett. 87, 092108 (2005).

[39] F. S. Galasso, Structure, properties and preparation of perovskite-type compounds: international series of monographs in solid state physics (Elsevier, 2013), Vol. 5

[40] J. F. Schooley, W. R. Hosler, E. Ambler, J. H. Becker, M. L. Cohen, and C. S. Koonce, Phys. Rev. Lett. 14, 305 (1965).

[41] J. G. Bednorz and K. A. Müller, Rev. Mod. Phys. 60, 585 (1988).

[42] B.-G. Kim, S. M. Cho, T.-Y. Kim, and H. M. Jang, Phys. Rev. Lett. 86, 3404 (2001).

[43] R. J. D. Tilley, Understanding solids: the science of materials (John Wiley Sons, 2004).

[44] J. Liu, C. Wang, W. Su, H. Wang, P. Zheng, J. Li, J. Zhang, and L. Mei, Appl. Phys. Lett. 95, 162110 (2009).

[45] C. Lin and A. A. Demkov, Phys. Rev. Lett. 111, 217601 (2013).

[46] S. Satpathy, Z. S. Popović, and F. R. Vukajlović, Phys. Rev. Lett. 76, 960 (1996).

[47] J. Neumeier and J. Cohn, Physical Review B 61, 14319 (2000).

[48] B. Dabrowski, S. Kolesnik, A. Baszczuk, O. Chmaissem, T. Maxwell, and J. Mais, Journal of Solid State Chemistry 178, 629 (2005).

[49] J. Inoue and S. Maekawa, Phys. Rev. Lett. 74, 3407 (1995).

[50] H. Kawano, R. Kajimoto, H. Yoshizawa, Y. Tomioka, H. Kuwahara, and Y. Tokura, Phys. Rev. Lett. 78, 4253 (1997).

[51] Y. Tomioka, A. Asamitsu, Y. Moritomo, H. Kuwahara, and Y. Tokura, Phys. Rev. Lett. 74, 5108 (1995).

[52] F. o. Gervais, J.-L. Servoin, A. Baratoff, J. G. Bednorz, and G. Binnig, Physical Review B 47, 8187 (1993).

[53] T. Kolodiazhnyi and S. Wimbush, Phys. Rev. Lett. 96, 246404 (2006).

[54] W. P. Mason and B. T. Matthias, Phys. Rev. 74, 1622 (1948).

[55] H. Y. Hwang, Y. Iwasa, M. Kawasaki, B. Keimer, N. Nagaosa, and Y. Tokura, Nature materials 11, 103 (2012).

[56] B. Fisher, J. Genossar, C. Kuper, L. Patlagan, G. Reisner, and A. Knizhnik, Physical Review B 47, 6054 (1993).

[57] P. A. Lee, N. Nagaosa, and X.-G. Wen, Rev. Mod. Phys. 78, 17 (2006).

[58] L. Sheng, D. Xing, D. Sheng, and C. Ting, Phys. Rev. Lett. 79, 1710 (1997).

[59] O. Prokhnenko, R. Feyerherm, E. Dudzik, S. Landsgesell, N. Aliouane, L. Chapon, and D. Argyriou, Phys. Rev. Lett. 98, 057206 (2007).

[60] H. Xiang, S.-H. Wei, M.-H. Whangbo, and J. L. Da Silva, Phys. Rev. Lett. 101, 037209 (2008).

[61] A. Malashevich and D. Vanderbilt, Phys. Rev. Lett. 101, 037210 (2008).

[62] J. Pérez, J. Garcia, J. Blasco, and J. Stankiewicz, Phys. Rev. Lett. 80, 2401 (1998).

[63] K. Miyano, T. Tanaka, Y. Tomioka, and Y. Tokura, Phys. Rev. Lett. 78, 4257 (1997).

[64] Y. Tokura, H. Kuwahara, Y. Moritomo, Y. Tomioka, and A. Asamitsu, Phys. Rev. Lett. 76, 3184 (1996).

[65] T. Ramakrishnan, H. Krishnamurthy, S. Hassan, and G. V. Pai, Phys. Rev. Lett. 92, 157203 (2004).

[66] S. A. Kimber, J. A. Rodgers, H. Wu, C. A. Murray, D. N. Argyriou, A. N. Fitch, D. I. Khomskii, and J. P. Attfield, Phys. Rev. Lett. 102, 046409 (2009).

[67] M. Imada, A. Fujimori, and Y. Tokura, Rev. Mod. Phys. 70, 1039 (1998).

[68] F. Evers and A. D. Mirlin, Rev. Mod. Phys. 80, 1355 (2008).

[69] A. Millis, P. Littlewood, and B. I. Shraiman, Phys. Rev. Lett. 74, 5144 (1995).

[70] Y. Tomioka, H. Kuwahara, A. Asamitsu, M. Kasai, and Y. Tokura, Appl. Phys. Lett. 70, 3609 (1997).

[71] Y. Long, L. Yang, Y. Lv, Q. Liu, C. Jin, J. Zhou, and J. B. Goodenough, Journal of Physics: Condensed Matter 23, 355601 (2011).

[72] Z. Fang, I. Solovyev, and K. Terakura, Phys. Rev. Lett. 84, 3169 (2000).

[73] J.-G. Cheng, J.-S. Zhou, and J. B. Goodenough, Proceedings of the National Academy of Sciences 110, 13312 (2013).

[74] X. Zhang and L.-D. Zhao, Journal of Materiomics 1, 92 (2015).

[75] N. S. Lewis and G. Crabtree, (US Department of Energy, Office of Basic Energy Science, 2005).

[76] H. J. Goldsmid, Introduction to thermoelectricity (Springer Science Business Media, 2009), Vol. 121

[77] T. J. Seebeck, Annalen der Physik 82, 133 (1826).

[78] K. Nielsen, Historical studies in the physical and biological sciences 21, 317 (1991).

[79] G. J. Snyder and E. S. Toberer, Nature materials 7, 105 (2008).

[80] C. C. Sorrell, J. Nowotny, and S. Sugihara, Materials for energy conversion devices (Elsevier, 2005).

[81] I. Terasaki, Y. Sasago, and K. Uchinokura, Physical Review B 56, 12685 (1997).

[82] V. Zlatic and A. Hewson, New Materials for Thermoelectric Applications: Theory and Experiment (Springer, 2013).

[83] L. E. Bell, Science 321, 1457 (2008).

[84] M. Vedernikov and E. Iordanishvili, in Thermoelectrics, 1998. Proceedings ICT 98. XVII International Conference on (IEEE, 1998), pp. 37.

[85] G. S. Nolas, J. Sharp, and J. Goldsmid, Thermoelectrics: basic principles and new materials developments (Springer Science Business Media, 2013), Vol. 45.

[86] T. M. Tritt and M. Subramanian, MRS bulletin 31, 188 (2006).

[87] G. A. Slack and D. Rowe, CRC, Boca Raton, FL 407 (1995).

[88] Y. Pei, X. Shi, A. LaLonde, H. Wang, L. Chen, and G. J. Snyder, Nature 473, 66 (2011).

[89] K. Kobayashi, S. Yamaguchi, M. Mukaida, and T. Tsunoda, Solid state ionics 144, 315 (2001).

[90] W. Koshibae, K. Tsutsui, and S. Maekawa, Physical Review B 62, 6869 (2000).

[91] P. M. Chaikin and G. Beni, Physical Review B 13, 647 (1976).

[92] L.-D. Zhao, S.-H. Lo, Y. Zhang, H. Sun, G. Tan, C. Uher, C. Wolverton, V. P. Dravid, and M. G. Kanatzidis, Nature 508, 373 (2014).

[93] S. I. Kim et al., Science 348, 109 (2015).

[94] C. Wood, Rep. Prog. Phys. 51, 459 (1988).

[95] C. Wood, Energy conversion and management 24, 317 (1984).

[96] A. R. West, Solid state chemistry and its applications (John Wiley Sons, 2014).

[97] H. Ohta, K. Sugiura, and K. Koumoto, lnorg. Chem. 47, 8429 (2008).

[98] S. R. S. Kumar, A. Z. Barasheed, and H. N. Alshareef, ACS applied materials interfaces 5, 7268 (2013).

[99] T. Caillat, M. Carle, P. Pierrat, H. Scherrer, and S. Scherrer, Journal of Physics and Chemistry of Solids 53, 1121 (1992).

[100] W. Kim, J. Zide, A. Gossard, D. Klenov, S. Stemmer, A. Shakouri, and A. Majumdar, Phys. Rev. Lett. 96, 045901 (2006).

[101] B. Poudel et al., Science 320, 634 (2008).

[102] W. Haken, Ann. Phys. (Leipzig) 832, 291 (1910).

[103] A. F. Ioffe, (1957).

[104] Y. Miyazaki, Solid State Ionics 172, 463 (2004).

[105] F. Zhang, N. I. U. Baocheng, K. Zhang, X. Zhang, L. U. Qingmei, and J. Zhang, Journal of Rare Earths 31, 885 (2013).

[106] R. Kabir, T. Zhang, D. Wang, R. Donelson, R. Tian, T. T. Tan, and S. Li, Journal of Materials Science 49, 7522 (2014).

[107] L. T. Hung, N. Van Nong, L. Han, D. Le Minh, K. A. Borup, B. B. Iversen, N. Pryds, and S. Linderoth, Journal of Materials Science 48, 2817 (2013).

[108] H. P. R. Frederikse, W. R. Thurber, and W. R. Hosler, Phys. Rev. 134, A442 (1964).

[109] H. Ohta et al., Nature materials 6, 129 (2007).

[110] M. A. Subramanian and M. H. Whangbo, Journal of Solid State Chemistry 96, 461 (1992).

[111] Y. Wang, K. H. Lee, H. Ohta, and K. Koumoto, J. Appl. Phys. 105, 103701 (2009).

[112] S. Hébert, D. Flahaut, C. Martin, S. Lemonnier, J. Noudem, C. Goupil, A. Maignan, and J. Hejtmanek, Progress in solid state chemistry 35, 457 (2007).

[113] A. Asamitsu, Y. Moritomo, and Y. Tokura, Physical Review B 53, R2952 (1996).

[114] H. Schmid, Ferroelectrics 162, 317 (1994).

[115] T. Kimura, T. Goto, H. Shintani, and K. Ishizaka, nature 426, 55 (2003).

[116] R. Ramesh and N. A. Spaldin, Nature materials 6, 21 (2007).

[117] J. Wang et al., Science 299, 1719 (2003).

[118] K. F. Wang, J. M. Liu, and Z. F. Ren, Adv. Phys. 58, 321 (2009).

[119] N. A. Spaldin and M. Fiebig, Science 309, 391 (2005).

[120] M. Mochizuki and Y. Watanabe, Appl. Phys. Lett. 107, 082409 (2015).

[121] G. Giovannetti and J. van den Brink, Phys. Rev. Lett. 100, 227603 (2008).

[122] A. Filippetti and N. A. Hill, Physical Review B 65, 195120 (2002).

[123] T. Kimura, S. Kawamoto, I. Yamada, M. Azuma, M. Takano, and Y. Tokura, Physical Review B 67, 180401 (2003).

[124] O. Chmaissem, B. Dabrowski, S. Kolesnik, J. Mais, D. E. Brown, R. Kruk, P. Prior, B. Pyles, and J. D. Jorgensen, Physical Review B 64, 134412 (2001).

[125] H. Sakai et al., Phys. Rev. Lett. 107, 137601 (2011).

[126] T. Kimura, G. Lawes, T. Goto, Y. Tokura, and A. Ramirez, Physical Review B 71, 224425 (2005).

[127] S. Dong, R. Yu, S. Yunoki, J. M. Liu, and E. Dagotto, Physical Review B 78, 155121 (2008).

[128] J. Van Den Brink and D. I. Khomskii, Journal of Physics: Condensed Matter 20, 434217 (2008).

[129] G. Giovannetti, S. Kumar, J. van den Brink, and S. Picozzi, Phys. Rev. Lett. 103, 037601 (2009).

[130] K. Gupta, P. Mahadevan, P. Mavropoulos, and M. Ležaić, Phys. Rev. Lett. 111, 077601 (2013).

[131] M. H. Qin, Y. M. Tao, M. Zeng, X. S. Gao, S. J. Wu, S. Dong, and J. M. Liu, Appl. Phys. Lett. 100, 052410 (2012).

[132] M. Mochizuki and N. Furukawa, Physical Review B 80, 134416 (2009).

[133] C. J. Fennie and K. M. Rabe, Physical Review B 72, 100103 (2005).

[134] R. E. Cohen, Nature 358, 136 (1992).

[135] S.-W. Cheong and M. Mostovoy, Nature materials 6, 13 (2007).

[136] H. Sim and B. G. Kim, Physical Review B 89, 201107 (2014).

[137] A. Filippetti, V. Fiorentini, F. Ricci, P. Delugas, and J. Íñiguez, Nature communications 7, 11211 (2016).

[138] D. Khomskii, Physics 2, 20 (2009).

[139] J. Zhang et al., Phys. Rev. Lett. 107, 147602 (2011).

[140] M. Mostovoy, Phys. Rev. Lett. 96, 067601 (2006).

[141] M. Mochizuki and N. Furukawa, Phys. Rev. Lett. 105, 187601 (2010).

[142] Y. Weng, L. Lin, E. Dagotto, and S. Dong, Phys. Rev. Lett. 117, 037601 (2016).

[143] H. Zhai, Y. Jiang, H. Li, P. Zhang, Y. He, D. Shi, X. Zhang, and J. Yang, Heliyon 3, e00313 (2017).

[144] K. J. Choi et al., Science 306, 1005 (2004).

[145] J. Haeni, P. Irvin, W. Chang, and R. Uecker, Nature 430, 758 (2004).

[146] T. Katsufuji, Y. Taguchi, and Y. Tokura, Physical Review B 56, 10145 (1997).

[147] H. Muta, K. Kurosaki, and S. Yamanaka, Journal of alloys and compounds 392, 306 (2005).

[148] S. Anwar and N. Lalla, Appl. Phys. Lett. 92, 212901 (2008).

[149] T. Negas and R. S. Roth, Journal of Solid State Chemistry 1, 409 (1970).

[150] A. Huq, J. P. Hodges, O. Gourdon, and L. Heroux, Z. Kristallogr. Proc 1, 127 (2011).

[151] B. H. Toby, J. Appl. Crystallogr. 34, 210 (2001).

[152] A. C. Larson and R. B. Von Dreele, Los Alamos National Laboratory, New Mexico, USA, 86 (2000).

[153] C. G. Shull, Rev. Mod. Phys. 67, 753 (1995).

[154] E. H. Kisi and C. J. Howard, Applications of neutron powder diffraction (Oxford University Press, 2012), Vol. 15.

[155] V. Sears, Thermal-neutron scattering lengths and cross sections for condensed-matter research (Chalk River Nuclear Laboratories Chalk River (Ontario), 1984).

[156] V. F. Sears, Neutron news 3, 26 (1992).

[157] D. Kan, R. Kanda, Y. Kanemitsu, Y. Shimakawa, M. Takano, T. Terashima, and A. Ishizumi, Appl. Phys. Lett. 88, 1916 (2006).

[158] J. H. Haeni et al., Nature 430, 758 (2004).

[159] J. G. Bednorz and K. A. Müller, Phys. Rev. Lett. 52, 2289 (1984).

[160] C. Eylem, H. L. Ju, B. W. Eichhorn, and R. L. Greene, Journal of Solid State Chemistry 114, 164 (1995).

[161] M. Itoh, R. Wang, Y. Inaguma, T. Yamaguchi, Y.-J. Shan, and T. Nakamura, Phys. Rev. Lett. 82, 3540 (1999).

[162] J. F. Schooley, W. R. Hosler, and M. L. Cohen, Phys. Rev. Lett. 12, 474 (1964).

[163] J. Schooley, W. Hosler, E. Ambler, J. Becker, M. L. Cohen, and C. Koonce, Phys. Rev. Lett. 14, 305 (1965).

[164] G. Binnig, A. Baratoff, H. Hoenig, and J. Bednorz, Phys. Rev. Lett. 45, 1352 (1980).

[165] C. J. Ball, B. D. Begg, D. J. Cookson, G. J. Thorogood, and E. R. Vance, Journal of Solid State Chemistry 139, 238 (1998).

[166] M. A. Carpenter, C. J. Howard, K. S. Knight, and Z. Zhang, Journal of Physics: Condensed Matter 18, 10725 (2006).

[167] S. Anwar and N. Lalla, Solid State Sciences 10, 307 (2008).

[168] S. Qin, A. I. Becerro, F. Seifert, J. Gottsmann, and J. Jiang, Journal of Materials Chemistry 10, 1609 (2000).

[169] R. Ranjan, D. Pandey, W. Schuddinck, O. Richard, P. De Meulenaere, J. Van Landuyt, and G. Van Tendeloo, Journal of Solid State Chemistry 162, 20 (2001).

[170] S. K. Mishra, R. Ranjan, D. Pandey, and B. J. Kennedy, J. Appl. Phys. 91, 4447 (2002).

[171] D. I. Woodward, P. L. Wise, W. E. Lee, and I. M. Reaney, Journal of Physics: Condensed Matter 18, 2401 (2006).

[172] C. J. Howard, R. L. Withers, K. S. Knight, and Z. Zhang, Journal of Physics: Condensed Matter 20, 135202 (2008).

[173] P. Ranson, R. Ouillon, J. P. Pinan-Lucarre, P. Pruzan, S. K. Mishra, R. Ranjan, and D. Pandey, Journal of Raman Spectroscopy 36, 898 (2005).

[174] R. Ranjan, P. Dhananjai, V. Siruguri, P. S. R. Krishna, and S. K. Paranjpe, Journal of Physics: Condensed Matter 11, 2233 (1999).

[175] B. J. Kennedy, C. J. Howard, and B. C. Chakoumakos, Journal of Physics: Condensed Matter 11, 1479 (1999).

[176] S. K. Mishra, R. Ranjan, D. Pandey, P. Ranson, R. Ouillon, J.-P. Pinan-Lucarre, and P. Pruzan, Journal of Physics: Condensed Matter 18, 1899 (2006).

[177] B. Dabrowski, O. Chmaissem, J. Mais, S. Kolesnik, J. D. Jorgensen, and S. Short, Journal of Solid State Chemistry 170, 154 (2003).

[178] O. Chmaissem, B. Dabrowski, S. Kolesnik, J. Mais, L. Suescun, and J. D. Jorgensen, Physical Review B 74, 144415 (2006).

[179] S. A. T. Redfern, Journal of Physics: Condensed Matter 8, 8267 (1996).

[180] T. Yamanaka, N. Hirai, and Y. Komatsu, American Mineralogist 87, 1183 (2002).

[181] C. J. Howard, R. L. Withers, Z. Zhang, K. Osaka, K. Kato, and M. Takata, Journal of Physics: Condensed Matter 17, 459 (2005).

[182] A. M. Glazer, Acta Crystallographica Section B: Structural Crystallography and Crystal Chemistry 28, 3384 (1972).

[183] A. M. Glazer, Acta Crystallographica Section A: Crystal Physics, Diffraction, Theoretical and General Crystallography 31, 756 (1975).

[184] J. Kapusta, P. Daniel, and A. Ratuszna, Physical Review B 59, 14235 (1999).

[185] E. Prince, A. J. C. Wilson, T. Hahn, and U. Shmueli, International tables for crystallography (International Union of Crystallography, 1999).

[186] R. Ubic, J. Am. Ceram. Soc. 90, 3326 (2007).

[187] Y. A. Abramov, V. G. Tsirelson, V. E. Zavodnik, S. A. Ivanov, and I. D. Brown, Acta Crystallographica Section B: Structural Science 51, 942 (1995).

[188] J. M. Kiat and T. Roisnel, Journal of Physics: Condensed Matter 8, 3471 (1996).

[189] Y. Kuroiwa, S. Aoyagi, A. Sawada, E. Nishibori, M. Takata, M. Sakata, H. Tanaka, and J. Harada, Journal of the Korean Physical Society 42, 1425 (2003).

[190] K. S. Knight, Journal of Alloys and Compounds 509, 6337 (2011).

[191] A. C. Komarek, H. Roth, M. Cwik, W. D. Stein, J. Baier, M. Kriener, F. Bourée, T. Lorenz, and M. Braden, Physical Review B 75, 224402 (2007).

[192] K. Müller, W. Berlinger, and F. Waldner, Phys. Rev. Lett. 21, 814 (1968).

[193] H. Thomas and K. Müller, Phys. Rev. Lett. 21, 1256 (1968).

[194] M. Cwik et al., Physical Review B 68, 060401 (2003).

[195] M. Eitel and J. E. Greedan, Journal of the Less Common Metals 116, 95 (1986).

[196] G. Shirane and Y. Yamada, Phys. Rev. 177, 858 (1969).

[197] R. Ranjan and D. Pandey, Journal of Physics: Condensed Matter 13, 4239 (2001).

[198] M. C. Steele and F. D. Rosi, J. Appl. Phys. 29, 1517 (1958).

[199] S. Q. Bai, X. Shi, and L. D. Chen, Appl. Phys. Lett. 96, 202102 (2010).

[200] G. S. Nolas, G. A. Slack, D. T. Morelli, T. M. Tritt, and A. C. Ehrlich, J. Appl. Phys. 79, 4002 (1996).

[201] D. T. Morelli and G. P. Meisner, J. Appl. Phys. 77, 3777 (1995).

[202] T. Takabatake, K. Suekuni, T. Nakayama, and E. Kaneshita, Rev. Mod. Phys. 86, 669 (2014).

[203] J. Liu, C. L. Wang, Y. Li, W. B. Su, Y. H. Zhu, J. C. Li, and L. M. Mei, J. Appl. Phys. 114, 223714 (2013).

[204] S. Moon, M. Hatano, M. Lee, and C. P. Grigoropoulos, International Journal of Heat and Mass Transfer 45, 2439 (2002).

[205] Y. Suemune, J. Phys. Soc. Jpn. 20, 174 (1965).

[206] J. Robertson, Journal of Vacuum Science Technology B 18, 1785 (2000).

[207] H.-S. Kim, Z. M. Gibbs, Y. Tang, H. Wang, and G. J. Snyder, APL materials 3, 041506 (2015).

[208] K. C. Lukas, W. Liu, G. Joshi, M. Zebarjadi, M. S. Dresselhaus, Z. Ren, G. Chen, and C. P. Opeil, Physical Review B 85, 205410 (2012).

[209] K. Takahata, Y. Iguchi, D. Tanaka, T. Itoh, and I. Terasaki, Physical Review B 61, 12551 (2000).

[210] J. Callaway, Phys. Rev. 113, 1046 (1959).

[211] J. Callaway and H. C. von Baeyer, Phys. Rev. 120, 1149 (1960).

[212] A. Eucken and G. Kuhn, Zeitschrift für Physikalische Chemie 134, 193 (1928).

[213] W. Kim, Journal of Materials Chemistry C 3, 10336 (2015).

[214] C. Glassbrenner and G. A. Slack, Phys. Rev. 134, A1058 (1964).

[215] S. R. Brown, S. M. Kauzlarich, F. Gascoin, and G. J. Snyder, Chemistry of materials 18, 1873 (2006).

[216] B. Paul and P. Banerji, J. Appl. Phys. 108, 064322 (2010).

[217] D. Spiteri, J. Anaya, and M. Kuball, J. Appl. Phys. 119, 085102 (2016).

[218] G. A. Slack, Phys. Rev. 126, 427 (1962).

[219] G. Burns, Solid State Commun. 35, 811 (1980).

[220] V. Kresin and S. Wolf, Rev. Mod. Phys. 81, 481 (2009).

[221] C. Kittel, Introduction to solid state (John Wiley Sons, 1966), Vol. 162.

[222] P. Klemens, Phys. Rev. 119, 507 (1960).

[223] J. Garg, N. Bonini, B. Kozinsky, and N. Marzari, Phys. Rev. Lett. 106, 045901 (2011).

[224] M. N. Luckyanova, D. Chen, W. Ma, H. L. Tuller, G. Chen, and B. Yildiz, Appl. Phys. Lett. 104, 061911 (2014).

[225] G. Meisner, D. Morelli, S. Hu, J. Yang, and C. Uher, Phys. Rev. Lett. 80, 3551 (1998).

[226] V. Ambegaokar, Phys. Rev. 114, 488 (1959).

[227] I. Wood, K. Knight, G. Price, and J. Stuart, J. Appl. Crystallogr. 35, 291 (2002).

[228] A. Ward and D. A. Broido, Physical Review B 81, 085205 (2010).

[229] N. Mott, J. Non·Cryst. Solids 1, 1 (1968).

[230] L. Zhang and Z.-J. Tang, Physical Review B 70, 174306 (2004).

[231] Y. Sun, X. Xu, and Y. Zhang, Journal of Physics: Condensed Matter 12, 10475 (2000).

[232] P. Sun, B. Wei, J. Zhang, J. M. Tomczak, A. Strydom, M. Søndergaard, B. B. Iversen, and F. Steglich, Nature communications 6 (2015).

[233] N. Mott and E. Davis, Electronic process in non-crystalline materials (Oxford University Press, 1971).

[234] S. Mollah, H. Huang, H. Yang, S. Pal, S. Taran, and B. Chaudhuri, Journal of magnetism and magnetic materials 284, 383 (2004).

[235] N. Mott, E. Davis, and R. Street, Philos. Mag. 32, 961 (1975).

[236] C. Lu, A. Quindeau, H. Deniz, D. Preziosi, D. Hesse, and M. Alexe, Appl. Phys. Lett. 105, 082407 (2014).

[237] N. F. Mott and W. Twose, in Sir Nevill Mott–65 Years In Physics (World Scientific, 1995), pp. 259.

[238] E. K. Weise and I. A. Lesk, The Journal of Chemical Physics 21, 801 (1953).

[239] J. S. Dyck, W. Chen, J. Yang, G. P. Meisner, and C. Uher, Physical Review B 65, 115204 (2002).

[240] T. Holstein, Annals of Physics 8, 343 (1959).

[241] X. Hao, Z. Wang, M. Schmid, U. Diebold, and C. Franchini, Physical Review B 91, 085204 (2015).

[242] A. Banerjee, S. Pal, and B. Chaudhuri, The Journal of Chemical Physics 115, 1550 (2001).

[243] A. Banerjee, S. Pal, E. Rozenberg, and B. Chaudhuri, Journal of Physics: Condensed Matter 13, 9489 (2001).

[244] J. Lago, P. Battle, M. Rosseinsky, A. Coldea, and J. Singleton, Journal of Physics: Condensed Matter 15, 6817 (2003).

[245] W. Wunderlich, H. Ohta, and K. Koumoto, Physica B: Condensed Matter 404, 2202 (2009).

[246] M. Yamamoto, H. Ohta, and K. Koumoto, Appl. Phys. Lett. 90, 072101 (2007).

[247] D. B. Marsh and P. E. Parris, Physical Review B 54, 7720 (1996).

[248] H. Goldsmid and J. Sharp, Journal of electronic materials 28, 869 (1999).

[249] K. Park, S. Nam, and C. Lim, Intermetallics 18, 1744 (2010).

[250] C. B. Vining, J. Appl. Phys. 69, 331 (1991).

[251] J. Ravichandran, W. Siemons, M. Scullin, S. Mukerjee, M. Huijben, J. Moore, A. Majumdar, and R. Ramesh, Physical Review B 83, 035101 (2011).

[252] M. Ahrens, R. Merkle, B. Rahmati, and J. Maier, Physica B: Condensed Matter 393, 239 (2007).

[253] M. B. Salamon and M. Jaime, Rev. Mod. Phys. 73, 583 (2001).

[254] J. H. Lee and K. M. Rabe, Phys. Rev. Lett. 104, 207204 (2010).

[255] J. M. Rondinelli, A. S. Eidelson, and N. A. Spaldin, Physical Review B 79, 205119 (2009).

[256] H. Chen and A. J. Millis, Physical Review B 94, 165106 (2016).

[257] V. Goian et al., Journal of Physics: Condensed Matter 28, 175901 (2016).

[258] V. Goian et al., Physical Review B 95, 075126 (2017).

[259] H. Sakai et al., Physical Review B 86, 104407 (2012).

[260] J. Goodenough, Rep. Prog. Phys. 67, 1915 (2004).

[261] R. D. Shannon, Acta crystallographica section A: crystal physics, diffraction, theoretical and general crystallography 32, 751 (1976).

[262] D. K. Pratt, J. W. Lynn, J. Mais, O. Chmaissem, D. E. Brown, S. Kolesnik, and B. Dabrowski, Physical Review B 90, 140401 (2014).

[263] B. Matthias and A. Von Hippel, Phys. Rev. 73, 1378 (1948).

[264] R. Buttner and E. Maslen, Acta Crystallographica Section B: Structural Science 48, 764 (1992).

[265] Y. Tokura and N. Nagaosa, Science 288, 462 (2000).

[266] W. Zhong, D. Vanderbilt, and K. Rabe, Phys. Rev. Lett. 73, 1861 (1994).

[267] R. Nourafkan, G. Kotliar, and A. M. S. Tremblay, Physical Review B 90, 220405 (2014).

[268] G. Giovannetti, S. Kumar, C. Ortix, M. Capone, and J. van den Brink, Phys. Rev. Lett. 109, 107601 (2012).

[269] B. Dabrowski, S. Kolesnik, O. Chmaissem, L. Suescun, and J. Mais, Acta Physica Polonica A 111, 15 (2007).

[270] M. Mouallem-Bahout, O. Peña, D. Gutierrez, P. Duran, and C. Moure, Solid State Commun. 122, 561 (2002).

[271] J.-S. Zhou and J. Goodenough, Physical Review B 77, 132104 (2008).

[272] L. M. Rodriguez-Martinez and J. P. Attfield, Physical Review B 54, R15622 (1996).

[273] O. Chmaissem, B. Dabrowski, S. Kolesnik, J. Mais, L. Suescun, and J. Jorgensen, Physical Review B 74, 144415 (2006).

[274] E. Langenberg, L. Maurel, N. Marcano, R. Guzmán, P. Štrichovanec, T. Prokscha, C. Magén, P. A. Algarabel, and J. A. Pardo, Advanced Materials Interfaces 4 (2017).

[275] A. Marthinsen, C. Faber, U. Aschauer, N. A. Spaldin, and S. M. Selbach, MRS Communications 6, 182 (2016).

[276] R. Søndenå, P. Ravindran, S. Stølen, T. Grande, and M. Hanfland, Physical Review B 74, 144102 (2006).

[277] T. Takeda and S. Ohara, J. Phys. Soc. Jpn. 37, 275 (1974).